2019

Catalytic Properties of Defect-Laden 2D Material from First-Principles

Tao Jiang
University of Central Florida

CATALYTIC PROPERTIES OF DEFECT-LADEN 2D MATERIAL FROM FIRST-PRINCIPLES

by

TAO JIANG
B.Sc. Northeastern University, China, 2013
M.Sc. University of Central Florida, USA, 2015

A dissertation submitted in partial fulfillment of the requirements
of the degree of Doctor of Philosophy
in the Department of Physics
in the College of Sciences
at the University of Central Florida
Orlando, Florida

Fall Term
2019
Major Professor: Talat Shahnaz Rahman

ABSTRACT

Two-dimensional (2D) materials offer excellent opportunities for application as catalysts for energy needs. Their catalytic activity depends on the nature of defects, their geometry and their electronic structure. It thus important that the characteristics of defect-laden 2D materials be understood at the microscopic level. My dissertation focuses on theoretical and computational studies of several novel nanoscale materials using state-of-the-art techniques based on density functional theory (DFT) with the objective of understanding the microscopic factors that control material functionality.

My work has helped establish defect-laden hexagonal boron nitride (*dh*-BN) as a promising metal-free catalyst for CO_2 hydrogenation. Firstly, I showed how small molecules (H_2, CO, CO_2) interacting with several kinds of defects in *dh*-BN (with nitrogen or boron vacancy, boron substituted for nitrogen, Stone-Wales defect). I analyzed binding energies and electronic structures of adsorption of molecules on *dh*-BN to predict their catalytic activities. Then by computational efforts on reaction pathways and activation energy barriers, I found that vacancies induced in *dh*-BN can effectively activate the CO_2 molecule for hydrogenation, where activation occurs through back-donation to the π^* orbitals of CO_2 from frontier orbitals (defect state) of the *h*-BN sheet localized near a nitrogen vacancy (V_N). Subsequent hydrogenation to formic acid (HCOOH) and methanol (CH_3OH), indicating *dh*-BN (V_N) an excellent metal-free catalyst for CO_2 reduction, which may serve as a solution for global energy and sustainability.

At the same time, I studied critical steps of the catalytic processes from carbon monoxide and methanol to higher alcohol on single-layer MoS_2 functionalized with small Au nanoparticle,

indicating C-C coupling feasible on MoS_2-Au_{13}, which led to production of acetaldehyde (CH_3CHO). Whereas a bilayer 31-atom cluster of gold on MoS_2 show excellent catalytic performance on CO hydrogenation to methanol through two effective pathways.

ACKNOWLEDGEMENTS

First, I would like to take this opportunity to express my sincere thanks to my advisor Pegasus Professor Talat S. Rahman for her patience, motivation and guidance. She is a great scholar with solid theoretical knowledge and wide scientific insights. Her great enthusiasm and rigorous attitude towards the research influence me a lot. I was lucky to be her student since I trained to be an independent researcher to have a full understanding of physics and abilities to expressing and explaining comprehensive and profound theoretical knowledge to others, which brings benefits for my further academic career. Her affirm and encourage help me to build confidence, which kept me in the correct track to finish my dissertation work. Moreover, she provide me chance to join a couple of projects to collaborate with many great scientists all over the world. Her leadership and professional promotes the group as well as interdisciplinary teamwork have achievements of high productivities and high qualities. Besides her academic guidance, she also guide me mentally and spiritually. She is very nice person with kindness, wise and optimistic attitude towards life. She helped every group member and the department a lot.

Then I want thank to Dr. Duy Le. I work with him on various catalysis projects. He is a professional scholar and a good mentor with responsibilities of day-to-day impact on me. He taught me a lot of knowledge on DFT as well as programming skills, making me always working in an efficient way. He is willing to take the initiative to new things and good at using new tools to explore the frontier of the research.

I would like to thank Dr.Volodymyr Turkowski. I work with him in TDDFT and DMFT. With his helpful scientific discussions, I gain a new understanding of research. His solid

knowledge on condensed matter physics impressed me a lot and made me realize the joy of doing research on physics, a way to better describe and understand the word from atomic scale.

I want to thank the former and current members of Dr. Rahman's research group: Naseem Ud Din, Dr. Takat B. Rawal, Dr. Zahra Hooshmand, Dr. Shree Ram Acharya, Rainier Berkley, Andre Childs, Dave Austin, Mahboob Ur Rehman, and Jia Shi for academic discussions and the friendly atmosphere in the office.

I would like to thank my dissertation committee member Professor Sergey Stolbov, who is also my course teacher, and his first-principles class let me enjoy learning knowledge in this fantastic area. Then, I want to thank Professor Laurene Tetard. As my committee member, she provided me with insightful comments and suggestion on my dissertation work. Moreover, her ideas in the research project inspired me a lot, helping me to explore new interdisciplinary. I want thank to Professor Richard G. Blair, my external committee member, also my main collaborative experimental scientist. Not only for his helpful discussions on our projects but also his comprehensive knowledge in chemistry offer me a lot of insightful ideas, which guide me make more progress on computational simulation.

I also would like to thank my girlfriend Jiaojiao Zhao for her support and company. These three years spent with her in Orlando was full of happiness and wonderful moments. She made me be a better person with more responsibilities. Her encouragement always helps me overcome difficulties in academia and in life.

I would like to express all my deepest gratitude to my parents: Hongwei Jiang and Chunmei Wu for their unconditional support uninterrupted encourage. My parents raised me up

and educated me well. I had a dream to be a scientist since I was a child. They did their best to provide me with a good environment. Their kindness and courage made me become a positive and optimistic person. I am honored to be their son and happy to be their pride. My parents are truly my spiritual support. There are no words to convey how important they are and how much I love them. I could not have completed my study without their support.

Moreover, I want to thank to my grandparents: Guochen Jiang and Suqin Liu, who raised me and witness my growing up. Their kindness, diligent, and optimistic attitude influence me a lot. I communicate with them every weekend and their voice full of concern and encouragement let me feel not far from home even though I am in USA. In addition, I want to thank all my family members and my relatives in China. Their concerns and supports encouraged me along my journey to get the Ph.D. degree.

Finally, I would like to thank those who have helped me achieve the significant milestone. The journey to the Ph.D. degree is going to the end and a new journey to become an outstanding scientist is just beginning.

TABLE OF CONTENTS

LIST OF FIGURES

LIST OF TABLES

CHAPTER 1: INTRODUCTION

The discovery of graphene [1-3] contributed to the exponentially growing of research on two-dimensional (2D) materials in the past decade. Graphene further motivated the investigation of next several 2D materials, such as hexagonal boron nitride (*h*-BN), molybdenum disulfide (MoS_2), and other members of 2D material family [4]. Applications of 2D material is wide [5], such as energy storage and conversion [6-8], electronics [9, 10], optoelectronics [11-13], and catalysis [14-16].

2D materials catalyst design and discovery for energy needs is in high demand since their unique geometric and electronic structures make them excellent catalysts for various catalytic processes [17]. As a wide band gap [18, 19] material, single layer *h*-BN is inert with high chemical stability [20]. Creating defects is one effective way to make *h*-BN become a chemically active catalyst by introducing defect states nearby the fermi level to offer the dangling bonds, for example, defect laden boron nitride (*dh*-BN) is catalytically active for hydrogenation under reductive conditions [14]. Another 2D material discussed in the dissertation is MoS_2, one of transition metal dichalcogenides (TMDs) family, also including WS_2, TiS_2, TaS_2, etc. The single-layer MoS_2 displays a direct band gap [21] and its basal plane is also chemically inert, but can be catalytically activated by functionalizing with defects such as creation of S vacancies which may align in a row in MoS_2 [22]. Another catalyst application is to let MoS_2 serve as a platform for stabilizing nanoscale metal particles, such as a 13 atom-gold cluster on MoS_2 [23], in which MoS_2 is a single layer with S vacancy. Because of new physics and chemistry properties

discovered in 2D material-based catalyst, fundamental studies in these topics have become hot research fields, whose rich achievements brings a lot of industrial applications.

Synthesis of value-added production such as methanol from syngas has been of great interest owing to the limited petroleum resources and environmental concerns. Rational designing of cheap and efficient catalyst material for such synthesis is in great demand because of diminishing supply of the current state-of-the-art catalysts. Defect-laden boron nitride is to be consider as a metal-free catalyst, which could meet these requests for replacing traditional catalysts. At the same time, 2D material supported metal nanoparticle attract attention since its unique catalytic properties compare with those of metal oxide platforms. In this dissertation, I explore pathways and mechanisms on both defect-laden boron nitride and MoS_2 functionalized with small Au nanoparticle, which could guide experimental work on CO_2 hydrogenation, and higher alcohol synthesis, respectively.

Modern heterogeneous catalysis research is capable of interdisciplinary subjects including physics, chemistry, engineering, and industrial technology with the process including modeling, prediction, synthesis, characterization and evaluation. With growth of computing power and improvement of algorithm, fundamental theoretical simulation has the power to play increasingly important role to led experiential discovery. In my dissertation, in order to investigate the properties of functional nanomaterials, I have utilized the most commonly used first-principles tool, density functional theory (DFT) [24], to carry out results on the geometry, energetics, electronic structure, activation barriers, and reaction pathways. DFT implemented in *ab-initio* calculation packages such as Quantum Espresso [25] and VASP [26], can serve to validate the conclusions that are drawn from analysis of experimentally measured data, and to

predict new ones for future experimental detection. The DFT-based calculation of the properties of a wide range of material systems leads to the establishment of a close coupling between theory and experiment.

The ultimate goal of the projects undertaken in this dissertation is to design 2D materials-based catalyst for energy needs such for catalytic conversion of syngas into alcohol. The organization of the rest of the dissertation is follows:

Chapter 2 introduces a set of theoretical methods employed in the present work to manifest certain qualities characteristic of electronic properties of involved defect-laden 2D materials (such as *dh*-BN) and nanoparticles on 2D materials (such as Au nanoparticles on MoS_2). Based on density functional theory, the chapter discusses the methods for optimized structure, calculation of adsorption energy, and activation energy barriers that determine the reaction pathways.

Chapter 3 describes an *ab initio* study of the geometry, electronic structure, and the propensity for adsorption of small molecules on a set of defects on *dh*-BN such as, nitrogen vacancy (V_N), boron vacancy (V_B), Stone Wales (SW) defect, and boron substitution for nitrogen (B_N), using density functional theory with the inclusion of van der Waals interactions. The four kinds of defects studied are plotted in Figure 1.1. Our results point out that the defect-laden boron nitride with nitrogen vacancy has the potential to be a catalyst for CO_2 hydrogenation.

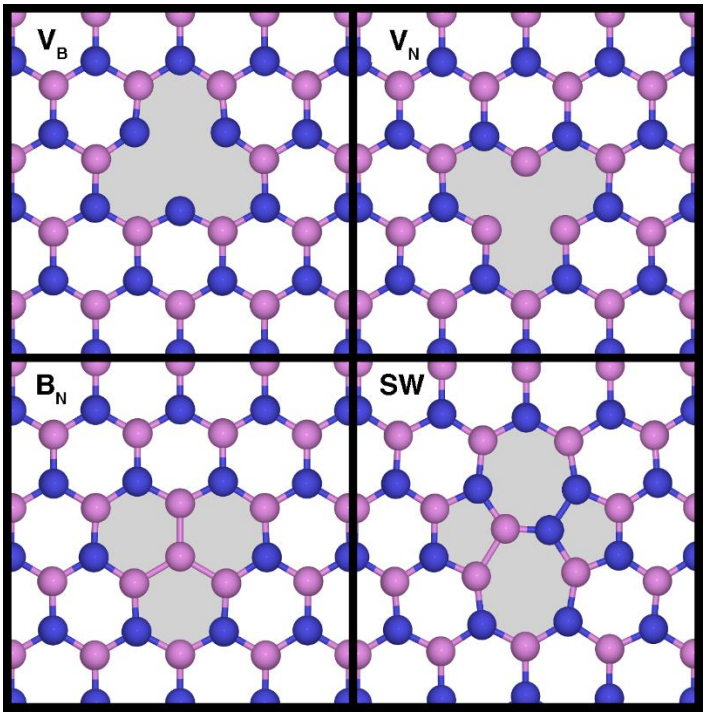

Figure 1.1 Four defect structures in *h*-BN studied. These are (from top left to bottom right): a nitrogen vacancy (V_B), a boron vacancy (V_N), boron substitution for nitrogen (B_N), and 90° rotation of a BN bond, aka Stone-Wales defect, (SW). Blue and pink spheres represent nitrogen and boron respectively. The light-gray backgrounds indicate the defected areas.

Chapter 4 reports a computational finding of the reduction of carbon dioxide to value-added molecules (methanol and formic acid) over defect-laden hexagonal boron nitride (*dh*-BN). By density functional theory (DFT), we find back-donation to the π^* orbitals of CO_2 from frontier orbitals (defect state) of the *h*-BN sheet localized near a nitrogen vacancy (V_N) can effectively activate the CO_2 molecule for hydrogenation. Based calculations of reaction pathways and activation energy barriers, we that *dh*-BN (V_N) is an excellent metal-free catalyst for CO_2 hydrogenated to formic acid (HCOOH) and methanol (CH_3OH). Figure 1.2 shows a schematic of pathways from CO_2 hydrogenation to formic acid and methanol on *dh*-BN (V_N).

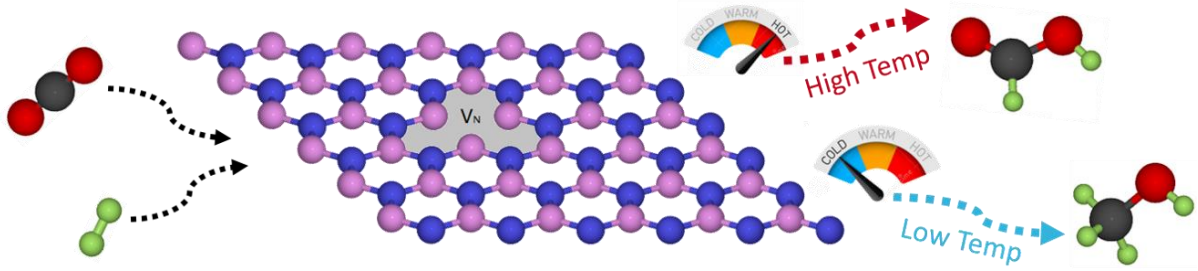

Figure 1.2 Schematic representation of *dh*-BN (V_N) catalyst for CO_2 hydrogenation to formic acid and methanol.

Chapter 5 deals with the formation of higher alcohols from syngas on 13-atom gold nanoparticle on a single-layer MoS_2 with an S vacancy. We apply density functional theory to study necessary steps for its realization, such as efficient C-C coupling from carbon monoxide and methanol. Figure 1.3 shows that CH_3* and H* which dissociative from methanol could react with CO to form acetyl (CH_3CO) and hydrogenation of acetyl to form acetaldehyde (CH_3CHO).

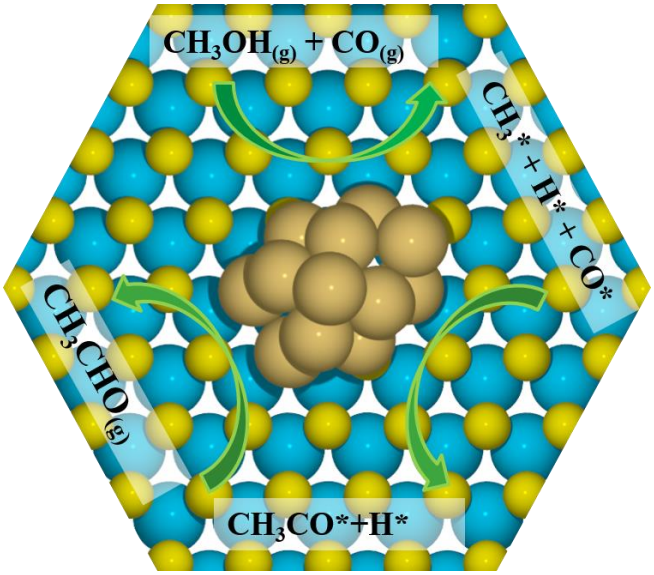

Figure 1.3 Schematic representation of important reaction steps in higher alcohol synthesis on Au_{13}-MoS_2 catalyst.

Chapter 6 explains the mechanism of hydrogenation of CO on bilayer 31-atom Au cluster supported on single-layer MoS_2 (Au_{31}/MoS_2) by employing dispersion-corrected density functional theory. We used Bader charge analysis for estimating charge transfer, indicating top layer of Au_{31} suit for molecules adsorption. Not like CO strong affinity for binding [23], H_2 could only physical adsorption on Au_{31}/MoS_2 but a lower dissociation barrier than that on Au_{13}/MoS_2 [27]. We find that Au_{31}/MoS_2 offers excellent activity toward methanol synthesis, via two competitive reaction pathways: CHO* → CH_2O* → CH_3O* → CH_3OH* and CHO* → CHOH* → CH_2OH* → CH_3OH*. Figure 1.4 shows a schematic of CO hydrogenation on the bilayer 31-atom Au cluster supported on single-layer MoS_2.

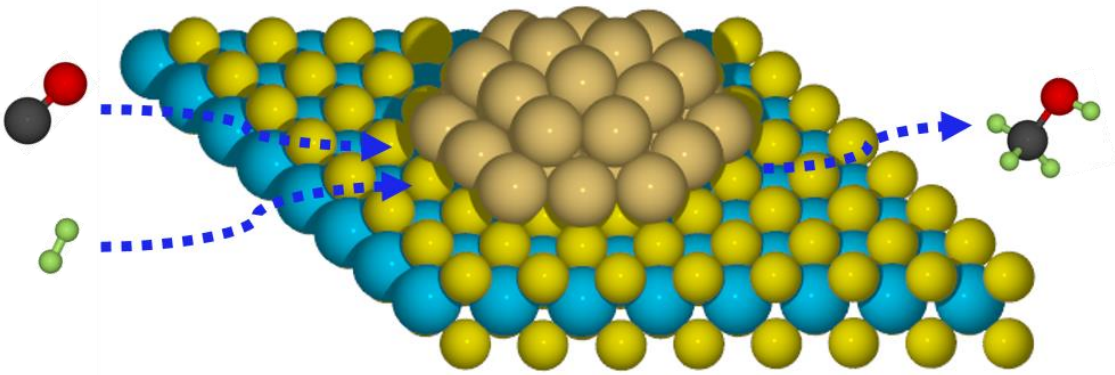

Figure 1.4 Schematic representation of CO hydrogenation on the bilayer 31-atom Au cluster supported on single-layer MoS_2.

The conclusions derived from the work presented in this thesis are presented in Chapter 7.

CHAPTER 2: THEORETICAL METHODS

2.1 Density Functional Theory

Density Functional Theory signifies an important milestone for approaching describing the condensed matter system, which use electron density as a basic variable instead of full wave function of many-electron system.

Since the birth of density functional theory (DFT) in 1965 [24], it has been the dominant method for the quantum mechanical simulation of periodic systems. Walter Kohn was awarded The Nobel Prize in Chemistry in 1998 for his contribution to build Density Functional Theory, which a computationally simpler method that makes it possible to study very large molecules.

With people's efforts [28], strategies base on DFT for describing quantum mechanical properties of material are evolving more and more accurately, making it the most useful technique we use to study materials starting from atomic scales.

In this section, I introduce the basic concepts underlying density functional theory and part of history of accuracy increasing via a vast array of approximations, which led to its widespread application.

2.1.1 Schrödinger Equation of Condensed Matter System

Thanks to Quantum Mechanics, people have founded a logically tight and fully self-consistent theoretical manner to describe a system with has N nuclei and n electrons via Schrödinger's equation.

We consider stationary states of matter-time-independent electronic states; we call it Stationary Schrödinger's equation:

$$\hat{H}\Psi = E\Psi \qquad (2.1)$$

If one applies Equation 2.1 to the system of N nuclei and n electrons, the Schrödinger's equation, which contain all the information about this system, can be written as:

$$\hat{H}\Psi(\boldsymbol{r_1}, \boldsymbol{r_2}, \dots, \boldsymbol{r_n}; \boldsymbol{R_1}, \boldsymbol{R_2}, \dots, \boldsymbol{R_N}) = E\Psi(\boldsymbol{r_1}, \boldsymbol{r_2}, \dots, \boldsymbol{r_n}; \boldsymbol{R_1}, \boldsymbol{R_2}, \dots, \boldsymbol{R_N}) \quad (2.2)$$

Whether $\boldsymbol{r_n}$ or $\boldsymbol{R_n}$, is a function of 3 spatial coordinates, there will be totally $3n + 3N$ variables to describe the whole system.

For this condensed matter system, the General Hamiltonian is:

$$\hat{H} = \hat{T}_e + \hat{T}_N + \hat{V}_{e-e} + \hat{V}_{N-N} + \hat{V}_{e-N} \qquad (2.3)$$

Where $\hat{T}_e$ presents kinetic energy of n electrons:

$$\hat{T}_e = -\frac{1}{2}\sum_{i=1}^{n} \nabla_i^2 \qquad (2.4)$$

Where $\hat{T}_N$ presents the kinetic energy of N nuclei:

$$\hat{T}_N = -\frac{1}{2}\sum_{p=1}^{N} \frac{1}{M_p} \nabla_p^2 \qquad (2.5)$$

Where $\hat{V}_{e-e}$ is a potential energy, describing electron-electron interactions:

$$\hat{V}_{e-e} = \sum_{i}^{n} \sum_{j>i}^{n} \frac{1}{|\boldsymbol{r_i} - \boldsymbol{r_j}|} \qquad (2.6)$$

Where $\hat{V}_{N-N}$ presents electrostatic nucleus-nucleus repulsion:

$$\hat{V}_{N-N} = \sum_{p}^{N} \sum_{q>p}^{N} \frac{1}{|\boldsymbol{R_p} - \boldsymbol{R_q}|} \qquad (2.7)$$

Where $\hat{V}_{e-N}$ presents electrostatic electron-nucleus repulsion:

$$\hat{V}_{e-e} = -\sum_{i=1}^{n}\sum_{p=1}^{N}\frac{Z_p}{r_{ip}} \qquad (2.8)$$

Since the above General Hamiltonian is complex, it is extremely challenging to obtain the full wave function of a system. It is thus necessary to apply approximations to General Hamiltonian in several ways, for example, neglecting the kinetic energy of the nuclei (second term of Equation 2.3) and the electrostatic nucleus-nucleus repulsion (the fourth term of Equation 2.3), since electrons move much faster than nuclei. This idea was an approximation introduced by Born and Oppenheimer in 1927 [29] and continues to this day.

2.1.2 Thomas-Fermi Model

The idea of DFT is mainly to describe the properties of systems using density functional rather than wave function. In 1927, Thomas and Fermi [30, 31] proposed an approach which has become known as the model of Thomas-Fermi, which described complex systems using electron density rather than the actual orbital wave function.

Imagine that the space was divided into many small boxes with the same side length of l, where every box obeys principles of the free electrons model. In a three-dimensional infinite potential, the particle in a box model (the infinite square well) describes a particle free to move in a small space surrounded by impenetrable barriers as:

$$\varepsilon(n_x, n_y, n_z) = \frac{(2\pi)^2}{8l^2}\left({n_x}^2 + {n_y}^2 + {n_z}^2\right) = \frac{(2\pi)^2 k^2}{8l^2} \qquad (2.9)$$

Every (n_x, n_y, n_z) represents a quantum state. Setting the center of a sphere at the origin of n_x, n_y, n_z coordinates, chose k as the radius, where k obeys

$$k^2 = {n_x}^2 + {n_y}^2 + {n_z}^2 \qquad (2.10)$$

Points (quantum states) at the sphere surface with the same radius=k, has the same energy. We can get the number of quantum states whose energy is smaller than ε is locate in 1/8 sphere, where

$$n_y, n_y, n_y > 0 \qquad (2.11)$$

$$n_y, n_y, n_y = 1,2,\cdots,\infty \qquad (2.12)$$

So the number of quantum states in 1/8 sphere is

$$\Phi(\varepsilon) = \frac{1}{8}\left(\frac{4}{3}\pi k^3\right) = \frac{1}{8}\left(\frac{4}{3}\pi\left(\frac{2\sqrt{2}l\varepsilon^{\frac{1}{2}}}{2\pi}\right)^3\right) = \frac{\pi}{6}\left(\frac{8l^2\varepsilon}{4\pi^2}\right)^{3/2} \qquad (2.13)$$

Number of states whose energy is between ε and $\varepsilon + \Delta\varepsilon$ is

$$\begin{aligned}&\Phi(\varepsilon + \Delta\varepsilon) - \Phi(\varepsilon)\\ &= \mathrm{A}(\varepsilon + \Delta\varepsilon)^{3/2} - \mathrm{A}(\varepsilon)^{3/2}\\ &= \frac{3}{2}A\varepsilon^{1/2}\Delta\varepsilon + O[(\Delta\varepsilon)^2]\end{aligned} \qquad (2.14)$$

In approach, we assume that $\mathrm{g}(\varepsilon)$ is density of states at ε,

$$\begin{aligned}\mathrm{g}(\varepsilon)\Delta\varepsilon &= \Phi(\varepsilon + \Delta\varepsilon) - \Phi(\varepsilon)\\ &\approx \frac{\pi}{4}\left(\frac{8l^2\varepsilon}{4\pi^2}\right)^{3/2}\varepsilon^{1/2}\Delta\varepsilon\end{aligned} \qquad (2.15)$$

For those small boxes equal to or smaller than ε_F, each state has two electrons, so the total number of electrons is

$$\Delta N = 2\int_0^{\varepsilon_F}\mathrm{g}(\varepsilon)d\varepsilon = \frac{8\pi}{3}\left(\frac{2}{4\pi^2}\right)^{3/2} l^3{\varepsilon_F}^{3/2} \qquad (2.16)$$

$$\Delta E = 2\int_0^{\varepsilon_F}\varepsilon\mathrm{g}(\varepsilon)d\varepsilon = \frac{8\pi}{5}\left(\frac{2}{4\pi^2}\right)^{3/2} l^3{\varepsilon_F}^{5/2} \qquad (2.17)$$

So that we can get:

$$\Delta E = \frac{3}{5}\Delta N \varepsilon_F = \frac{3}{5}\Delta N \left(\Delta N / \left(\frac{8\pi}{3}\left(\frac{2}{4\pi^2}\right)^{3/2} l^3\right)\right)^{2/3}$$

$$= \frac{3}{5}\left(\frac{4\pi^2}{2}\right)\left(\frac{3}{8\pi}\right)^{2/3} \Delta N^{5/3} l^{-2}$$

$$= \frac{3}{5}\left(\frac{4\pi^2}{2}\right)\left(\frac{3}{8\pi}\right)^{2/3} l^3 \left(\frac{\Delta N}{l^3}\right)^{5/3} \quad (2.18)$$

Since that $\rho = \frac{\Delta N}{\Delta V} = \left(\frac{8\pi}{3}\left(\frac{2}{4\pi^2}\right)^{3/2} l^3 {\varepsilon_F}^{3/2}\right)/(l^3)$, one can get

$$\Delta E = = C_F \rho^{5/3} \Delta V \quad (2.19)$$

Integral it over all space, and we get

$$T_{TF} = \int \Delta E = C_F \int \rho^{5/3}(\boldsymbol{r}) d\boldsymbol{r} \quad (2.20)$$

We can find energy is a functional of $\rho(\boldsymbol{r})$, which is the historical first effort to build Density Functional Theory. We can find the way to get energy that is not related to wave function. We apply this process to systems of atoms to get the Thomas-Fermi Energy Functional

$$E_{TF}[\rho] = T + U_{eN} + U_{ee}$$

$$= C_F \int \rho^{5/3}(\boldsymbol{r}) d\boldsymbol{r} + \int \rho(\boldsymbol{r}) v_{ext}(\boldsymbol{r}) d\boldsymbol{r} + \frac{1}{2}\int \frac{\rho(\boldsymbol{r_1})\rho(\boldsymbol{r_2})}{\mathbf{r_{12}}} d\boldsymbol{r_1} d\boldsymbol{r_2} \quad (2.21)$$

where $v_{ext}(\boldsymbol{r}) = -\frac{Ze^2}{\boldsymbol{r}}$, representing the attractive Coulomb's potential between electrons and nuclei. Here $\rho(\boldsymbol{r})$ has the form

$$\int \rho(\boldsymbol{r}) d\boldsymbol{r} = N \quad (2.22)$$

When we apply Lagrange multiplier (μ), we obtain:

$$\delta\{E_{TF}[\rho] - \mu_{TF}(\int \rho(\boldsymbol{r}) d\boldsymbol{r} - \boldsymbol{N})\} = 0 \quad (2.23)$$

We apply Equation 2.21 into Equation 2.23 to gain:

$$\frac{5}{3} C_F \rho^{2/3}(\boldsymbol{r}) + v_{ext}(\boldsymbol{r}) + \int \frac{\rho(\boldsymbol{r})}{|\boldsymbol{r} - \boldsymbol{r'}|} d\boldsymbol{r} - \mu_{TF} = 0 \quad (2.24)$$

The Thomas-Fermi approximate functional (Equation 2.24) shows the relation between density functional and the external potential, where μ_{TF} can be defined as chemical potential. Together with Equation 2.22, we can get the solutions of $\rho(\boldsymbol{r})$ first and then get $E_{TF}[\rho]$. Here, we can find that Thomas-Fermi Model can calculate energy from electron density functional. However, this model was built on the assumption of homogeneous electron gas, which neglected the exchange energy between electrons. Therefore, a more accurate model to describe electrons in the external potential is in high demand.

2.1.3 The First Hohenberg-Kohn Theorem

The first Hohenberg-Kohn theorem was presented by P. Hohenberg and W. Kohn in 1964 [32]: When the external potential $V(\boldsymbol{r})$ is determined, there is a unique corresponding electron density $\rho(\boldsymbol{r})$.

Proof by contradiction: Consider a system of N electrons, there is the quantity $V(\boldsymbol{r_i})$ representing the interaction between the i^{th} electron and the external potential. The quantity $\sum_i^N V(\boldsymbol{r_i})$ will be the total potential energy describing the interaction between the system of N electrons and the external potential.

Now we assumed that there are two different external potentials: $V_1(\boldsymbol{r})$ and $V_2(\boldsymbol{r})$, where $V_1(\boldsymbol{r}) - V_2(\boldsymbol{r}) \neq constant$, which can determine the same electron density. For these two different external potentials, there will be two different Hamiltonians:

$$\hat{H}_1 = \hat{T} + \sum_i^N V_1(\boldsymbol{r_i}) + \sum_{i=1}^N \sum_{i<j}^N \frac{1}{\boldsymbol{r_{ij}}} \qquad (2.25)$$

As well as we have

$$\hat{H}_2 = \hat{T} + \sum_i^N V_2(\boldsymbol{r_i}) + \sum_{i=1}^N \sum_{i<j}^N \frac{1}{\boldsymbol{r_{ij}}} \quad (2.26)$$

Corresponding with each Hamiltonian, there is a non-degenerate ground state wave function Ψ_1 and Ψ_2. From Ψ_1 and Ψ_2, we can get two electron density $\rho_1(\boldsymbol{r})$ and $\rho_2(\boldsymbol{r})$. According to the variational principle, we obtain

$$\begin{aligned} E_1 &= \langle \Psi_1 | \hat{H}_1 | \Psi_1 \rangle < \langle \Psi_2 | \hat{H}_1 | \Psi_2 \rangle \\ &= \langle \Psi_2 | \hat{H}_2 | \Psi_2 \rangle + \langle \Psi_2 | \hat{H}_1 - \hat{H}_2 | \Psi_2 \rangle \\ &= E_2 + \int \rho_2(\boldsymbol{r})[V_1(\boldsymbol{r}) - V_2(\boldsymbol{r})]d\boldsymbol{r} \end{aligned} \quad (2.27)$$

$$\begin{aligned} E_2 &= \langle \Psi_2 | \hat{H}_2 | \Psi_2 \rangle < \langle \Psi_1 | \hat{H}_2 | \Psi_1 \rangle \\ &= \langle \Psi_1 | \hat{H}_1 | \Psi_1 \rangle + \langle \Psi_1 | \hat{H}_2 - \hat{H}_1 | \Psi_1 \rangle \\ &= E_1 - \int \rho_1(\boldsymbol{r})[V_1(\boldsymbol{r}) - V_2(\boldsymbol{r})]d\boldsymbol{r} \end{aligned} \quad (2.28)$$

If $\rho_1(\boldsymbol{r})$=$\rho_2(\boldsymbol{r})$, we add Equation 2.27 and Equation 2.28, and then we can get

$$E_1 + E_2 < E_2 + E_1 \quad (2.29)$$

This is a contradiction, which means that the initial assumption $\rho_1(\boldsymbol{r}) \neq \rho_2(\boldsymbol{r})$ is not correct. So far, we proof that it is a one-to-one correspondence relationship between the external potential $V(\boldsymbol{r})$ and the electron density $\rho(\boldsymbol{r})$.

2.1.4 The Second Hohenberg-Kohn theorem

The Second Hohenberg-Kohn theorem: For a system of N electrons with a ground state energy E_0, for any functional $\rho'(\boldsymbol{r})$, which obeys $\rho'(\boldsymbol{r}) \geq 0$ and $\int \rho'(\boldsymbol{r})d\boldsymbol{r} = N$, one can get $E[\rho'(\boldsymbol{r})] \geq E_0$. In other words, this theorem says the ground state density has the lowest energy.

Proof: From the first Hohenberg-Kohn theorem, $\rho'(\boldsymbol{r})$ could make sure an unique corresponding $V'(\boldsymbol{r})$, so that we have relevant $\hat{H}_1$ and, Ψ' , we assum Ψ' is variational function, we have

$$\langle \Psi' | \hat{H} | \Psi' \rangle = \hat{T}[\rho'(\boldsymbol{r})] + E_{ee}[\rho'(\boldsymbol{r})] + \int \rho'(\boldsymbol{r}) V'(\boldsymbol{r}) d\boldsymbol{r} = E[\rho'(\boldsymbol{r})] \quad (2.30)$$

For ground state, its wave functions write as Ψ:

$$\langle \Psi' | \hat{H} | \Psi' \rangle \geq \langle \Psi | \hat{H} | \Psi \rangle = E_0 \quad (2.31)$$

So that we have:

$$E[\rho'(\boldsymbol{r})] \geq E_0 \quad (2.32)$$

Equation 2.32 indicates that ground state density has the lowest energy.

2.1.5 Kohn-Sham Formalism

With the success of the two Hohenberg-Kohn theorems, it allows us to write the total energy of the ground state of a system of N interacting electrons in an external field:

$$E[\rho] = T[\rho] + V[\rho] + E_{ee}[\rho] \quad (2.33)$$

Assume there is another corresponding system of non-interacting electrons, and is an orthogonal normalization function group of $\{\phi_i, i = 1, \dots, N\}$, which obeys

$$\rho(\boldsymbol{r}) = \sum_{i=1}^{N} |\phi_i(\boldsymbol{r})|^2 \quad (2.34)$$

Here $\rho(\boldsymbol{r})$ is the electron density functional of the realistic system. Whereas, the kinetic energy of the system of non-interacting electrons is:

$$T_{KS}[\rho] = \sum_{i=1}^{N} \left\langle \phi_i \middle| -\frac{1}{2}\nabla^2 \middle| \phi_i \right\rangle = -\frac{1}{2}\sum_{i=1}^{N} \langle \phi_i | \nabla^2 | \phi_i \rangle \qquad (2.35)$$

For Equation 2.33, it is easy that $V[\rho]$ can be calculated by $V[\rho] = \int \rho(\boldsymbol{r}) V_{ext}(\boldsymbol{r}) d\boldsymbol{r}$, but the remain terms $T[\rho]$ and $E_{ee}[\rho]$ still need to be figured out.

Here we define a new functional $E_{XC}[\rho]$ as:

$$E_{XC}[\rho] = T[\rho] - T_{KS}[\rho] + V_{ee}[\rho] - J[\rho] \qquad (2.36)$$

The functional $E_{XC}[\rho]$ is called as exchange-correlation energy, which can be separated into two terms: the first term is that $T[\rho]$ subtracting $T_{KS}[\rho]$; The second term is that $V_{ee}[\rho]$ subtracting $J[\rho]$, where $J[\rho]$ is classical Coulomb interaction:

$$J[\rho] = \frac{1}{2}\int \frac{\rho(\boldsymbol{r_1})\rho(\boldsymbol{r_2})}{\boldsymbol{r_{12}}}\, d\boldsymbol{r_1} d\boldsymbol{r_1} \qquad (2.37)$$

Now the total energy of a system of N interacting electrons in an external field (Equation 2.33) can be rewritten as:

$$E[\rho] = T_{KS}[\rho] + J[\rho] + \int V(\boldsymbol{r})\, \rho(\boldsymbol{r}) dr + E_{XC}[\rho] \qquad (2.38)$$

Here, the main idea is to minimize the influence of $E_{XC}[\rho]$ in the Equation 2.38. The strategy is that if $\{\phi_i, i = 1, \dots, N\}$ is chosen good enough, one can make $T_{KS}[\rho] + J[\rho]$ be the main body, and $E_{XC}[\rho]$ will be a small functional. By this unique method approximation, we will have small error in total energy equation because of a small functional $E_{XC}[\rho]$.

For $\{\phi_i, i = 1, \dots, N\}$, there is:

$$E[\rho] = \sum_{i=1}^{n} \int \phi_i^*(\boldsymbol{r}) \left[-\frac{1}{2}\nabla^2\right] \phi_i(\boldsymbol{r}) d\boldsymbol{r} + \frac{1}{2}\int \frac{\rho(\boldsymbol{r_1})\rho(\boldsymbol{r_2})}{\boldsymbol{r_{12}}}\, d\boldsymbol{r_1} d\boldsymbol{r_1} + \int V(\boldsymbol{r})\, \rho(\boldsymbol{r}) d\boldsymbol{r} + E_{XC}[\rho] \quad (2.39)$$

In the condition that $\langle \phi_i | \phi_j \rangle = \delta_{ij}, i, j = 1 \ldots, N$, and $\varepsilon_{ij} = \varepsilon_i \delta_{ij}$, one calculates its extreme value with the variational principle:

$$\delta\left\{E[\rho] - \sum_{i=1}^{N}\sum_{j=1}^{N} \varepsilon_{ij} \int \phi_i^*(\boldsymbol{r})\, \phi_i(\boldsymbol{r}) d\boldsymbol{r}\right\} = 0 \quad (2.40)$$

So, we get Kohn-Sham Equation [24]:

$$\widehat{H}_{KS}\phi_i \equiv \left[-\frac{1}{2}\nabla^2 + V_{eff}(\boldsymbol{r})\right]\phi_i(\boldsymbol{r}) = \varepsilon_i \phi_i(\boldsymbol{r}) \quad (2.41)$$

Where $V_{eff}(\boldsymbol{r})$ is Kohn-Sham effective potential:

$$V_{eff}(\boldsymbol{r}) = V(\boldsymbol{r}) + V_H(\boldsymbol{r}) + V_{XC}(\boldsymbol{r}) \quad (2.42)$$

We call $V_{XC}(\boldsymbol{r})$ as exchange-correlation potential:

$$V_{XC}(\boldsymbol{r}) = \frac{\delta E_{XC}[\rho]}{\delta \rho(\boldsymbol{r})} \quad (2.43)$$

And the classical electrostatic potential is also called as Hartree potential:

$$V_H(\boldsymbol{r}) = \frac{\delta J[\rho]}{\delta \rho(\boldsymbol{r})} = \int \frac{\rho(\boldsymbol{r\prime})}{|\boldsymbol{r} - \boldsymbol{r}'|} d\boldsymbol{r}' \quad (2.44)$$

The term $V_{XC}(\boldsymbol{r})$, which is called the exchange-correlation potential, is determined from $E_{XC}[\rho]$. By calculating the solutions to Kohn-Sham equation (Equation 2.41), we can get $\{\phi_i\}$, which can lead us to get the ground state electron density $\rho(\boldsymbol{r})$ and energy $E[\rho]$.

Here, the wave functions ϕ_i and the eigenvalues ϵ_i are called as Kohn-Sham orbitals and Kohn-Sham eigenvalues, respectively, which are solutions of Kohn-Sham equations. Keep in mind that these orbitals and eigenvalues are not of real electrons, they belong to Kohn-Sham quasi-particles.

Figure 2.1 shows the flow chart of for solving Kohn-Sham equations in a self-consistent loop:

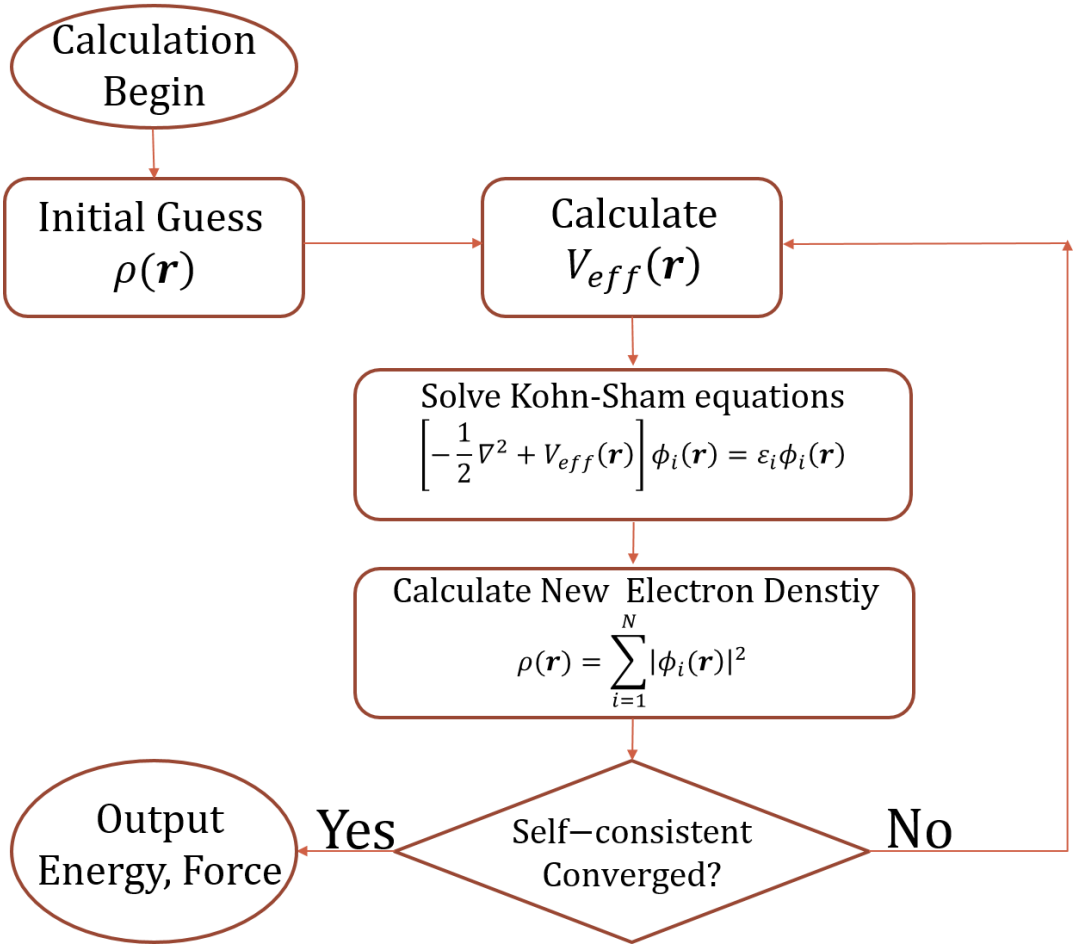

Figure 2.1 A flow chart representation of self-consistent ground state DFT calculations.

Step 1: Make an initial guess for the electron density $\rho(\boldsymbol{r})$.

Step 2: Calculate the Kohn-Sham effective potential, which contains external potential $V(\boldsymbol{r})$, Hartree potential $V_{ext}(\boldsymbol{r})$, and exchange-correlation potential $V_{XC}(\boldsymbol{r})$.

Step 3: Solve the Kohn-Sham equations (Equation 2.41) to obtain Kohn-Sham wave functions $\phi_i(\boldsymbol{r})$, which is one to one correspond to the electron density $\rho(\boldsymbol{r})$. Note that this step is the most time-consuming step.

Step 4: Calculate a new electron density using Equation 2.34

Step 5: If the electron density is self-consistent, the calculation is done, gaining output such as energy or force. Otherwise, go back to Step 2 to a new loop until converged.

2.2 The Exchange-Correlation Functional

In KS-DFT calculation, the most difficulty is to calculate exchange-correlation functional $E_{XC}[\rho]$, which is the only unknown functional in Kohn-Sham Formalism.

However, to solve KS equation with an exact exchange-correlation functional is too expensive to achieve, which calls for appropriate and effective approximations of the exchange-correlation functional. There are many approximation methods, for example, the local density approximation and the generalized-gradient approximation, which are widely used. For the details of these two methods, I provide as following.

2.2.1 The Local Density Approximation

To apply Kohn-Sham method to realistic calculation, the relation between $E_{XC}[\rho]$ and $V_{XC}[\rho]$ is necessary. In principle, if one knows the exact exchange-correlation functional, it is possible to solve KS equation, although generally it is a complex problem. However, for homogeneous electron gas, the relation between $E_{XC}[\rho]$ and $V_{XC}[\rho]$ can be determined correctly. This leads to the approximation known as the local density approximation (LDA), which

assumes that the exchange-correlation energy experienced by each electron at point $\boldsymbol{r}$ is the same as that of a homogeneous electron gas with the same electron density. Using this approximation, the exchange energy and potential are calculated exactly as:

$$E_{XC}^{LDA}[\rho] = \int \rho(\boldsymbol{r})\varepsilon_{XC}[\rho(\boldsymbol{r})]d\boldsymbol{r} \quad (2.45)$$

$$E_{XC}^{LDA}[\rho] = E_X[\rho] + E_C[\rho] \quad (2.46)$$

$$\varepsilon_{XC}[\rho(\boldsymbol{r})] = \varepsilon_X[\rho(\boldsymbol{r})] + \varepsilon_C[\rho(\boldsymbol{r})] \quad (2.47)$$

Where, $E_X[n]$ is the exchange energy; $E_C[\rho]$ is the correction energy; $\varepsilon_X[\rho(\boldsymbol{r})]$ is the exchange energy per electron; $\varepsilon_C[\rho(\boldsymbol{r})]$ is the correction energy per electron.

For homogeneous electron gas, background charge is uniform and hence external potential is constant:

$$E_X[\rho] = \int \rho(\boldsymbol{r})\varepsilon_X d\boldsymbol{r} \quad (2.48)$$

The expression of exchange part is given by Dirac et al [33, 34]:

$$\varepsilon_X = -\frac{3}{4}\left(\frac{3}{\pi}\right)^{\frac{1}{3}}\rho^{\frac{1}{3}}(\boldsymbol{r}) = -\frac{0.4582}{r_s} \quad (2.49)$$

Where, r_s is the effective radius of the sphere with density $n(r)$ and is defined as:

$$\frac{4}{3}\pi {r_s}^3 = \frac{1}{n} \quad (2.50)$$

The quantities E_X and ε_X are easily calculated via LDA, but the correlation energy E_C and potential ε_C are still difficult to solved. However, there are various approximations such as Vosko-Wilk-Nusiar (VWN) [35], Perdew-Zunger (PZ81) [36], Cole-Perdew (CP) [37], Perdew-Wang (PW92) [38] which address the calculation of the correlation energy.

2.2.2 The Generalized-Gradient Approximation

LDA method is suit for a homogeneous gas, but cannot handle systems with inhomogeneity of electrons density. To describe the inhomogeneity of electrons density, one method is to use the first or higher order of derivatives of electron density with respect to the spatial coordinates. This approach was first proposed by Hohenberg and Kohn [32], known as gradient-expansion approximation (GEA), but turned out to give suboptimal results which were worse than LDA.

A better approximation is that the exchange-correlation functional is gradient expansion for E_{XC}: considering ε_{XC} as a function of density and the gradient of the density, which is known generalized-gradient approximation (GGA). Typically, exchange-correlation energy is expressed as following:

$$E_{XC} = \int \rho(\boldsymbol{r})\varepsilon_{XC}[\rho(\boldsymbol{r})]d\boldsymbol{r}$$

$$= \int \rho(\boldsymbol{r})\varepsilon_X^{hom}F_{XC}\,[\rho(\boldsymbol{r}), \nabla\rho(\boldsymbol{r}), \nabla^2\rho(\boldsymbol{r}), \nabla^3\rho(\boldsymbol{r}), \dots]d\boldsymbol{r} \qquad (2.51)$$

The functional F_{XC}, is dimensionless, a correction parameter applying to ε_X^{hom}. Numerous versions of GGA have been subsequently proposed, for example, the famous GGA method known as Perdew-Burke-Ernzerhoff (PBE) [39]:

$$E_{XC}^{PBE}[\rho] = E_X^{PBE}[\rho] + E_C^{PBE}[\rho] \qquad (2.52)$$

$$E_X^{PBE}[\rho, \eta] = E_X^{PBE}[\rho] - C_\eta \int a\left(1 - \frac{1}{1+b\eta^2}\right)\rho^{4/3}(r)d\boldsymbol{r} \qquad (2.53)$$

Where $C_\eta = \frac{3}{4}\left(\frac{3}{\pi}\right)^{1/3}$, $a = 0.804$ and $b = 0.273$, is

$$E_C^{PBE}[\rho, \xi] = E_C^{LDA}[\rho, \xi] + \int G[t(\boldsymbol{r})]\rho(\boldsymbol{r})d\boldsymbol{r} \qquad (2.54)$$

$$G[t(r)] = cf^3(\xi)\ln B = g\left[exp\left(\frac{1+Bt^2}{1+Bt^2+B^2t^2}\right) - 1\right]^{-1} \qquad (2.55)$$

where c=0.031091, g=2.146119.

LDA works well for some properties, such as the lattice constant, whereas PBE works well for dissociation energy, adsorption energy, bond lengths, and bond angles. And there are many other GGA methods such as LYP [40] and PW91 [41] which I do not discuss here.

2.3 van der Waals interactions in DFT

The van der Waals interaction is relatively weak, widespread in nature, play an important role in many chemical systems, describing interactions between atoms and molecules. For example, van der Waals interaction is the source of stability for physisorption of molecules on surfaces.

DFT with LDA and GGA functionals has been extremely successful in predicting structural, elastic, vibrational properties of materials bound by metallic, ionic, covalent bonds, but neither LDA or GGA describe vdW interaction. There are two ways: The first way is to add an empirical damped dispersion correction, which has been presented in well-known methods, such as, DFT-D [42] DFT-D2 [43], and DFT-D3 [44]. The second way is to develop a truly non-local exchange-correlation functional as in the well-known vdw-DF [45] and vdw-DF2 [46] methods. Some details of these methods are provided below.

2.3.1 DFT-D

A simple and crude approximation is the pair interaction between two ions, which was proposed by Grimme in 2006 [42], known as DFT-D. In this approximation, the total energy of

the system consists of two different parts: (1) the total energy from DFT calculation (2) and an empirical damped dispersion correction:

$$E_{tot}^{DFT-D} = E_{tot}^{DFT} + E_{tot}^{disp} \quad (2.56)$$

$$E_{tot}^{disp} = -s_6 \sum_{i=1}^{N_{at}-1} \sum_{j=i+1}^{N_{at}} \frac{C_6^{ij}}{R_{ij}^6} f_{dmp}(R_{ij}) \quad (2.57)$$

Here, N_{at} is the number atoms in the system, C_6^{ij} denotes the dispersion coefficient for atmo pair ij, s_6 is a global scaling factor that only depends on the DF used, $R_{ij}^6$is an ineratoimic distance.

$$f_{dmp}(R) = \frac{1}{1+e^{-\alpha(R/R_0-1)}} \quad (2.58)$$

2.3.2 DFT-D2

Part of the problems of the original DFT-D approach, especially with heavier elements, can be traced back to the combination rule employed for the composed C_6^{ij} coefficients that gives too much weight to the smaller coefficient (lighter atom). Careful testing of systems including elements up to xenon and large hydrocarbons with many hydrogen atoms showed that a geometric mean of the coefficient would lead to a better approximation. This is the second version of Grimme's dispersion correction method [43], labeled as DFT-D2:

$$E_{tot}^{disp} = -s_6 \sum_{i=1}^{N_{at}-1} \sum_{j=i+1}^{N_{at}} \frac{C_6^{ij}}{R_{ij}^6} f_{dmp}(R_{ij}) \quad (2.59)$$

Where s_6 is a scaling factor; $f_{dmp}(r_{ij})$ is damping function to avoid the divergence at short distance and is given by

$$f_{dmp}(R_{ij}) = \frac{1}{1+e^{-d(R_{ij}/R_r-1)}} \quad (2.60)$$

Where d=20; R_{ij} is the sum of atomic vdW radii of atom i and j.

The coefficient C_6^{ij} is calculated as the follow:

$$C_6^{ij} = \sqrt{C_6^i C_6^j} \quad (2.61)$$

Atomic C_6 coefficients that is derived from the London formula for dispersion.

$$C_6^a = 0.05 N I_p^a \alpha^a \quad (2.62)$$

Where I_p^a is atomic ionization potentials and α^a represent static dipole polarizabilities.

2.3.3 DFT-D3

DFT-D3 is the third version of DFT-D, which was proposed by Grimme et al. in 2010 [44]. The dispersion coefficients are calculated from first principles based pre-calculated C_6 coefficients, which is from a large database of dispersion coefficients calculated accurately for any pair of atoms:

$$E_{tot}^{disp} = E_{n=6}^{disp} + E_{n=8}^{disp} \quad (2.63)$$

Where $E_{n=6}^{disp}$ and $E_{n=8}^{disp}$ are

$$E_{n=6}^{disp} = s_6 f_6(r_{ij}) \frac{C_6^{ij}}{r_{ij}^6} \quad (2.64)$$

$$E_{n=8}^{disp} = s_8 f_8(r_{ij}) \frac{C_8^{ij}}{r_{ij}^8} \quad (2.65)$$

In the formalism $f_n(r_{ij})$ is chosen as:

$$f_n(r_{ij}) = \frac{1}{1+6\left[\frac{r_{ij}}{s_n R_{ij}}\right]^{-\alpha}} \quad (2.66)$$

2.3.4 vdW-DF Functional

The methods vdW-DF and vdDW-DF2 [45, 46] are vdW exchange-correlation functionals to take into account the vdW interaction into DFT calculations. In contrast to empirical damped dispersion corrections based on external parameters like the DFT-D family, the vdW-DF functional directly calculate the dispersion interaction from electron density.

The vdW-DF method uses an exchange-correlation functional, which combines of all the correlations for all ranges:

$$E_{XC} = E_X^{GGA}[\rho(r)] + E_C^{LDA}[\rho(r)] + E_c^{non-local}[\rho(r)] \qquad (2.67)$$

The last term which is fully non-local correlation energy is given by:

$$E_c^{non-local} = \frac{1}{2}\int d^3r d^3r' \rho(r) K(r,r') \rho(r') \qquad (2.68)$$

$$K(r,r') = K(\rho(r), \rho(r'), |\nabla\rho(r)|, |\nabla\rho(r')||r - r'|) \qquad (2.69)$$

$K(r,r')$ is a universal kernel and its definition for different classes of vdW-DF methods can be found in the literature. The first and second terms in Equation 2.67 are the exchange energy evaluated using GGA functional and the local correlation energy obtained using LDA, respectively.

Although this method is computationally more expensive than DFT-D methods, it improves the values of lattice parameter and binding energies as a result of more accurate approach for considering the non-local interactions.

2.4 Practical DFT Methods for Periodic Structures

Even after we have in hand the approaches to calculate the exchange-correlation functional and van der Waals interactions, it is still a problem to apply DFT to a realistic system because it contains infinite number of electrons and nuclei. By the help of Bloch's theorem [47], one can apply DFT methods to a periodic system.

2.4.1 Bloch's Theorem

Schrödinger's equation of an independent electron can write as

$$\left[-\frac{\hbar}{2m}\nabla^2 + V(\boldsymbol{r})\right]\psi(\boldsymbol{r}) = E\psi(\boldsymbol{r}) \qquad (2.70)$$

If the electron is in a periodic potential

$$V(\boldsymbol{r}+\boldsymbol{l}) = V(\boldsymbol{r}) \qquad (2.71)$$

The solutions (using k to present) should be

$$\psi_k(\boldsymbol{r}) = u_{\boldsymbol{k}}(\boldsymbol{r})e^{i\boldsymbol{k}\cdot\boldsymbol{r}} \qquad (2.72)$$

Where $u_k(\boldsymbol{r})$ have the same periodic symmetry as the lattice

$$u_k(\boldsymbol{r}+\boldsymbol{l}) = u_k(\boldsymbol{r}) \qquad (2.73)$$

For the wave function at $\boldsymbol{r}+\boldsymbol{l}$, it should be

$$\psi_k(\boldsymbol{r}+\boldsymbol{l}) = u_k(\boldsymbol{r}+\boldsymbol{l})e^{ik\cdot(\boldsymbol{r}+\boldsymbol{l})} = u_k(\boldsymbol{r})e^{ik\cdot\boldsymbol{l}}e^{ik\cdot\boldsymbol{r}} = e^{ik\cdot\boldsymbol{l}}\psi_k(\boldsymbol{r}) \qquad (2.74)$$

Which is known as Bloch's theorem.

The physical meaning is that the wave function at $\boldsymbol{r}+\boldsymbol{l}$ and $\boldsymbol{r}$ is with same probability density $|\psi(\boldsymbol{r})|^2$, whereas different phase factor $\exp(i\boldsymbol{k}\cdot\boldsymbol{l})$

With aid of Bloch's theorem, we can calculate the system in a unit cell (periodic models for these systems, called supercell [48]) instead of one of infinite size.

2.4.2 k-point Sampling

For counting of electrons in bands, total energies and other physical and chemical quantities, which was labeled as Q, we need to sum its density $q(\boldsymbol{k})$ over $\boldsymbol{k}$ in Brillouin zone:

$$Q = \frac{\Omega}{(2\pi)^3} \int q(\boldsymbol{k}) d\boldsymbol{k} \qquad (2.75)$$

Numerically, we only take care about some average the quantity at various k-points in the space, and we sum them like this:

$$Q = \frac{1}{N_k} \sum_{\boldsymbol{k}} q(\boldsymbol{k}) \qquad (2.76)$$

Because of the fact that electronic wave functions at $\boldsymbol{k}$ points that are in a small region will be similar [48], choosing suitable $\boldsymbol{k}$ points needs strategy, such as k-point Sampling. There are some simple methods, one is sampling at one point (also called Baldereschi point or Gamma point) [49], another is sampling at some special point [50]. And a method of sampling at regular meshes was developed by Monkhorst and Pack [19]. This method is to sample the Brillouin zone by an equally spaced mesh, whose accuracy was controlled by the density of mesh points.

2.4.3 Plane-wave Basis Sets

It is easy to show that the wave-vectors can be defined in terms of the following reciprocal lattice vectors. Assuming that a unit cell is defined with three vectors $\boldsymbol{a_1}$, $\boldsymbol{a_2}$, and $\boldsymbol{a_3}$, the volume of the unit cell is

$$\Omega = \boldsymbol{a_1} \cdot (\boldsymbol{a_2} \times \boldsymbol{a_3}) \qquad (2.77)$$

We consider a periodic case in which $\boldsymbol{r}$ and $\boldsymbol{r}+\boldsymbol{R}$ has same properties. For direct lattice vectors $\boldsymbol{R}$, one can write it as

$$\boldsymbol{R} = n_1\boldsymbol{a_1} + n_2\boldsymbol{a_2} + n_3\boldsymbol{a_3} \quad (2.78)$$

where $\boldsymbol{a_1}$, $\boldsymbol{a_2}$, and $\boldsymbol{a_3}$ are all integers.

And there are three vectors $\boldsymbol{b_1}$, $\boldsymbol{b_2}$, and $\boldsymbol{b_3}$, in reciprocal lattice and there is a relationship between $\boldsymbol{a_i}$ and $\boldsymbol{b_i}$:

$$\boldsymbol{b_i} \cdot \boldsymbol{a_i} = 2\pi\delta_{ij} \quad (2.79)$$

For every reciprocal lattice vector $\boldsymbol{b_i}$, we have

$$\boldsymbol{b_1} = 2\pi\frac{\boldsymbol{a_2}\times\boldsymbol{a_3}}{\Omega} \quad (2.80)$$

$$\boldsymbol{b_2} = 2\pi\frac{\boldsymbol{a_3}\times\boldsymbol{a_1}}{\Omega} \quad (2.81)$$

$$\boldsymbol{b_3} = 2\pi\frac{\boldsymbol{a_1}\times\boldsymbol{a_2}}{\Omega} \quad (2.82)$$

And we have reciprocal lattice vectors $\boldsymbol{G}$:

$$\boldsymbol{G} = n_1\boldsymbol{b_1} + n_2\boldsymbol{b_2} + n_3\boldsymbol{b_3} \quad (2.83)$$

Bloch's function can be described in reciprocal lattice vectors:

$$\psi_{\boldsymbol{k}}(\boldsymbol{r}) = \sum_{\boldsymbol{G}} C_{\boldsymbol{k}+\boldsymbol{G}}\, e^{i(\boldsymbol{k}+\boldsymbol{G})\cdot\boldsymbol{r}} \quad (2.84)$$

Where $u_{\boldsymbol{k}}(\boldsymbol{r})$ also being periodic in the reciprocal space

$$u_{\boldsymbol{k}}(\boldsymbol{r}) = \sum_{\boldsymbol{G}} C_{\boldsymbol{k}+\boldsymbol{G}}\, e^{i\boldsymbol{G}\cdot\boldsymbol{r}} \quad (2.85)$$

Kinetic energy operator is diagonal in the plane wave basis

$$-\frac{1}{2}\nabla^2\psi_{\boldsymbol{k}}(\boldsymbol{r}) = -\frac{1}{2}\big(i(\boldsymbol{k}+\boldsymbol{G})\big)^2 \sum_{\boldsymbol{G}} C_{\boldsymbol{k}+\boldsymbol{G}}\, e^{i(\boldsymbol{k}+\boldsymbol{G})\cdot\boldsymbol{r}} = \frac{1}{2}(\boldsymbol{k}+\boldsymbol{G})^2\psi_{\boldsymbol{k}}(\boldsymbol{r}) \quad (2.86)$$

So kinetic energy cutoff is defined as:

$$E_{cut} = \frac{1}{2}|\boldsymbol{k} + \boldsymbol{G}|^2 \qquad (2.87)$$

However, the coefficients, $\boldsymbol{k} + \boldsymbol{G}$, for the plane waves with small kinetic energies are more important than those with large kinetic energies. Thus, the plane wave basis set can be truncated to include only plane waves that have kinetic energies that are smaller than some particular cutoff energy as illustrated

Kohn-Sham equation can be rewritten with Plane-wave Basis Sets as:

$$E_{cut} = \sum_{\boldsymbol{G}'} \left[\frac{1}{2}|\boldsymbol{k} + \boldsymbol{G}|^2 \delta_{\boldsymbol{G},\boldsymbol{G}'} + V^{eff}_{\boldsymbol{G},\boldsymbol{G}'}\right] C_{i,\boldsymbol{k}+\boldsymbol{G}} = \varepsilon_i C_{\boldsymbol{k}+\boldsymbol{G}'} \qquad (2.88)$$

Where:

$$V^{eff}_{\boldsymbol{G},\boldsymbol{G}'} = \int V^{eff}_{\boldsymbol{G},\boldsymbol{G}'} e^{i(\boldsymbol{G}-\boldsymbol{G}')} d\boldsymbol{r} \qquad (2.89)$$

Here E_{cut} is the plane wave cutoff energy. It is the highest kinetic energy of all basis functions and determines the number of basis functions. The basis set convergence can be systematically controlled by increasing the plane wave cutoff energy. To reduce errors, we can increase the cutoff energy,

The strength of plane-wave basis sets is its implementation ease, controllable accuracy (by varying the number of plane-wave basis set), and its appropriateness for periodic systems.

2.4.4 Pseudopotential Approximation

For the core electrons that form the inner-shells and are strongly bound to nuclei, there are sharp features and nodes in their wave function $\psi(\boldsymbol{r})$, which require representation by a large number of plane waves and drain of computational resource. As we know, core electrons do not participate in bonding, whereas valence electrons that fill the highest energy level bind weakly to

the nuclei in the outer-shell play most important role in in chemical interactions. To avoid huge calculation on core electrons, the pseudopotential approximation was developed by Phillips and Kleinman [51], which behave as a smooth plane wave at the core replacing those of the core electrons.

Real wave function of the valence electrons $\psi_v(\boldsymbol{r},\boldsymbol{k})$ is supposed to combine linearly with a smooth valence function $\lambda_v(\boldsymbol{r},\boldsymbol{k})$ and expand the remaining portion in terms of core states $\phi_c(\boldsymbol{r},\boldsymbol{k})$, which can be described as:

$$\psi_v(\boldsymbol{r},\boldsymbol{k}) = \lambda_v(\boldsymbol{r},\boldsymbol{k}) - \sum_c \sigma_{cv}(\boldsymbol{k})\phi_c(\boldsymbol{r},\boldsymbol{k}) \quad (2.90)$$

Because the smooth valence function $\lambda_v(\boldsymbol{r},\boldsymbol{k})$ is orthogonal to core states $\phi_c(\boldsymbol{r},\boldsymbol{k})$, we can get the portion parameter $\sigma_{cv}(\boldsymbol{k})$:

$$\sigma_{cv}(\boldsymbol{k}) = \int d\boldsymbol{r}'\, \phi_c^*(\boldsymbol{r},\boldsymbol{k})\lambda_v(\boldsymbol{r},\boldsymbol{k}) \quad (2.91)$$

Schrödinger's equation of valence electrons is

$$\hat{H}\psi_v(\boldsymbol{r},\boldsymbol{k}) = E_v(\boldsymbol{k})\psi_v(\boldsymbol{r},\boldsymbol{k}) \quad (2.92)$$

Schrödinger's equation of core electrons is

$$\hat{H}\phi_c(\boldsymbol{r},\boldsymbol{k}) = E_c(\boldsymbol{k})\phi_c(\boldsymbol{r},\boldsymbol{k}) \quad (2.93)$$

And substituting 2.90 in 2.92 we find

$$\hat{H}[\lambda_v(\boldsymbol{r},\boldsymbol{k}) - \sum_c \int d\boldsymbol{r}'\, \phi_c^*(\boldsymbol{r},\boldsymbol{k})\lambda_v(\boldsymbol{r},\boldsymbol{k})\phi_c(\boldsymbol{r},\boldsymbol{k})] = E_v(\boldsymbol{k})\psi_v(\boldsymbol{r},\boldsymbol{k}) \quad (2.94)$$

We firstly look at the left term we can get:

$$Left = \hat{H}\lambda_v(\boldsymbol{r},\boldsymbol{k}) - E_c(\boldsymbol{k})\phi_c(\boldsymbol{r},\boldsymbol{k}) \sum_c \int d\boldsymbol{r}'\, \phi_c^*(\boldsymbol{r},\boldsymbol{k})\lambda_v(\boldsymbol{r},\boldsymbol{k}) \quad (2.95)$$

And right term is

$$Right = E_v(\boldsymbol{k})\lambda_v(\boldsymbol{r},\boldsymbol{k}) - E_v(\boldsymbol{k}) \sum_c \int d\boldsymbol{r}'\, \phi_c^*(\boldsymbol{r},\boldsymbol{k})\lambda_v(\boldsymbol{r},\boldsymbol{k})\phi_c(\boldsymbol{r},\boldsymbol{k}) \quad (2.96)$$

From Left= Right we can get

$$\left[\widehat{H} + (E_v(\boldsymbol{k}) - E_c(\boldsymbol{k})) \int d\boldsymbol{r}'\, \phi_c^*(\boldsymbol{r},\boldsymbol{k})\phi_c(\boldsymbol{r},\boldsymbol{k})\right]\lambda_v(\boldsymbol{r},\boldsymbol{k}) = E_v(\boldsymbol{k})\lambda_v(\boldsymbol{r},\boldsymbol{k}) \quad (2.97)$$

We construct

$$\widehat{H}_{pseudo} = \widehat{H} + (E_v(\boldsymbol{k}) - E_c(\boldsymbol{k})) \int d\boldsymbol{r}'\, \phi_c^*(\boldsymbol{r},\boldsymbol{k})\phi_c(\boldsymbol{r},\boldsymbol{k}) \quad (2.98)$$

With the same eigenvalues as the original Hamiltonian the associated potential is

$$V_{pseudo} = V + (E_v(\boldsymbol{k}) - E_c(\boldsymbol{k})) \int d\boldsymbol{r}'\, \phi_c^*(\boldsymbol{r},\boldsymbol{k})\phi_c(\boldsymbol{r},\boldsymbol{k}) \quad (2.99)$$

Here V_{pseudo} is called the pseudopotential.

In the first-principle calculation, norm-conserving pseudopotential method is one of common methods, which was proposed by Hamann, Schlüter and Chiang in 1979 [52], which satisfied the condition: inside the core region ($r < r_c$). The total charge generated by pseudo wavefunctions must be identical with that generated from true wave-functions, and pseudo wavefunctions is in the same shape and norm with true wave-functions in the region out of r_c, which is norm-conserving.

However, for elements belonging to Period 1 element and transition element, norm-conserving pseudopotential required large values of E_{CUT}. In 1990, Vanderbilt proposed a new and radical method for generating pseudopotentials by relaxing the norm-conservation constraint to obtain smoother pseudo wave functions [53]. Pseudopotentials generated in this way (due to their softness) require a much smaller planewave cutoff and thus a much smaller number of planewaves. For this reason, they are usually called as ultrasoft pseudopotentials (USPP). This can be done by splitting the pseudo wave functions into two parts: Ultrasoft valence wave function that do not fulfill the norm conservation criteria

In 1994, Blöchl introduced the projector-augmented wave method (PAW) [54]: an all-electron equivalent method – that can be used for high accuracy first principles simulations. In (1999), Kresse and Joubert [55] made reformulation of the method to calculate electron density and illustrated the internal relations between USPP and PAW, so that PAW method became widely used. The main idea of the method is to use a transformation operator that can map the true wave functions onto pseudo wave functions. Since pseudo wave functions are computationally favorite, they are used in the Kohn-Sham equation. Once pseudo wave functions are obtained, the transformation operator constructs real wave functions that are used for evaluating observables. By people's efforts, the pseudo potential makes the calculations more efficient.

2.5 Method for Finding Transition States

Transition state theory (TST) was found Eyring, Evans, and Polanyi in 1935 [56, 57], to state that the process from the reactant to the production would have immediate transition state which has higher energy. The lower energy of the process which from reactant to the product through transition state, the easier reaction can happen, which we called it minimum energy path (MEP). Finding MEP is a key component of most computational chemistry to study the reactivity from reactant to product. Usually the energy difference between transition state and reactant is consider as the barrier, which is very important measurement to determine the level of reaction rate.

In a complex surface reaction, from reactant to product, it may take many MEPs. If we can converge all partial geometries' MEPs into a same MEP, we can say we find a MEP between the reactant and product we desired.

2.5.1 Nudged-Elastic Band Method

The Nudged-Elastic band (NEB) method was developed by Henkelman et al. in 2000 [58], which become a popular method to determine minimum-energy paths (MEPs) and the transition states (TS) in the past decades.

First, we define the geometries along the expected minimum-energy path as a set of $N+1$ images: $\{R_0, R_1, R_2, \dots R_i \dots R_N\}$. Instead of using the simplest normalized way $\hat{\boldsymbol{\tau}}_{\boldsymbol{i}} = \frac{R_{i+1}-R_{i-1}}{|R_{i+1}-R_{i-1}|}$, a way bisecting the two unit vectors is adopted as:

$$\hat{\boldsymbol{\tau}}_{\boldsymbol{i}} = \frac{R_{i+1}-R_{i-1}}{|R_{i+1}-R_{i-1}|} \qquad (2.100)$$

This vector is the tangent vector at image i and is calculated by bisecting the two unit vectors from image $i \to i+1$ and $i-1 \to i$:

$$\boldsymbol{\tau}_i = \frac{R_i-R_{i-1}}{|R_i-R_{i-1}|} + \frac{R_{i+1}-R_i}{|R_{i+1}-R_i|} \qquad (2.101)$$

Then normalize it and we have

$$\hat{\boldsymbol{\tau}}_{\boldsymbol{i}} = \boldsymbol{\tau}_i/|\boldsymbol{\tau}_i| \qquad (2.102)$$

The total force acting on the image R_i is the sum of the spring force along the tangent and the true force of the image R_i:

$$F_i^{Total} = -\nabla V_i + F_i^{Spring} \qquad (2.103)$$

In order to converge to the MEP, the true force perpendicular to the tangent of the image R_i can be removed. For the elastic band force F_i^{EB} on the image R_i, we defined it as the sum of the spring forces along the tangent and the true force perpendicular to the tangent of the image R_i .

$$F_i^{EB} = -\nabla V_i|_\perp + F_i^{Spring} = [-\nabla V_i - (-\nabla V_i \cdot \hat{\boldsymbol{\tau}}_{\boldsymbol{i}})] + F_i^{Spring} \quad (2.104)$$

Remove perpendicular component of spring force as Nudged Elastic Band Method, parallel component of the spring force is known as 'nudging'.

$$F_i^{NEB} = -\nabla V_i|_\perp + F_i^{Spring}|_\parallel = [-\nabla V_i - (-\nabla V_i \cdot \hat{\boldsymbol{\tau}}_{\boldsymbol{i}})] + F_i^{Spring}|_{||} \quad (2.105)$$

Where the parallel component of the spring force is

$$F_i^{Spring}|_{||} = k[(R_{i+1} - R_i) - (R_i - R_{i-1})] \cdot \hat{\boldsymbol{\tau}}_{\boldsymbol{i}}\hat{\boldsymbol{\tau}}_{\boldsymbol{i}} \quad (2.106)$$

So that we can get force of Nudged Elastic Band as:

$$F_i^{NEB} = -\nabla V_i|_\perp + F_i^{Spring}|_\parallel \hat{\boldsymbol{\tau}}_{\boldsymbol{i}}\hat{\boldsymbol{\tau}}_{\boldsymbol{i}} + f(\phi_i)(F_i^{Spring}|_\parallel - F_i^{Spring}|_\parallel \hat{\boldsymbol{\tau}}_{\boldsymbol{i}}\hat{\boldsymbol{\tau}}_{\boldsymbol{i}}) \quad (2.107)$$

Here we use $f(\phi_i) = \frac{1}{2}(1 + \cos(\pi cos\phi_i))$, where $cos\phi_i = \frac{(\vec{x}_{i+1} - \vec{x}_i)(\vec{x}_i - \vec{x}_{i-1})}{|\vec{x}_{i+1} - \vec{x}_i||\vec{x}_i - \vec{x}_{i-1}|}$

If φ = 90°, the full perpendicular component of spring force is kept, but when φ = 0°, none of the perpendicular spring force is kept.

2.5.2 Climbing Image Nudged Elastic Band Method

Climbing-Image (CI) NEB [59] is a modified version of the regular NEB method[58], which the image with the highest energy always at the saddle point with no spring forces along the band. The full force of this image is inverted along the elastic band:

$$F_i^{climb} = -\nabla E\left(R_{i_{max}}\right) + 2\nabla E\left(R_{i_{max}}\right)|_{\parallel}$$

$$= -\nabla E\left(R_{i_{max}}\right) + 2\nabla E\left(R_{i_{max}}\right) \cdot \hat{\boldsymbol{\tau}}_{\boldsymbol{i}_{max}} \hat{\boldsymbol{\tau}}_{\boldsymbol{i}_{max}} \qquad (2.108)$$

This climbing image will be in the saddle point after the CI-NEB method converges. One need to notice that CI-NEB needs to start after some regular NEB calculations, which NEB will estimate potential with the component along the elastic band. If initially the calculations start with CI-NEB, the convergence process takes much longer especially if the maximum energy image is far from the saddle point.

CHAPTER 3: ADSORPTION OF SYNGAS MOLECULES ON DEFECT-LADEN SINGLE-LAYER HEXAGONAL BORON NITRIDE

Defect-Laden hexagonal BN (*dh*-BN) single layer is attracting a lot of attention for application on catalyst for energy needs. We present results of spin polarized density functional theory (DFT), with vdW-DF2 functional to account for the nonlocal van der Waals interaction, to perform the adsorption of syngas (H_2, CO, CO_2) on *dh*-BN with various defects, namely, Nitrogen vacancy (V_N), Born vacancy (V_B), Stone–Wales (SW), Nitrogen substituted by Boron (B_N). By measuring binding energy, charge transfer and electronic structures, we obtain a deep understanding about interaction between molecules and these *dh*-BN substrates, what role of defect states play in the adsorption. We find that CO and CO_2 molecules chemisorb on these *dh*-BN substrates, whereas H_2 could only physisorb. V_N and V_B showed strong affinity for CO and CO_2 since the defect states are close to the fermi level. SW is not favorable for adsorption of these small molecules, since the adsorption of two hydrogen, CO and CO_2 are all endothermic processes. B_N can make CO bind strongly but show a week interaction with CO_2. After systematically investigating the adsorption of small molecules on these defects, we predict that *dh*-BN (V_N) is a good candidate catalyst for CO and CO_2 hydrogenation.

3.1 Introduction

The adsorption of H_2, CO, and CO_2 (syngas) on solid catalyst materials are the fundamental processes during catalytic conversion of them into useful chemical products (simple to higher alcohols, formaldehyde, formic acid, and higher hydrocarbons) [60-62]. The hydrogenation of CO or CO_2 offer various reaction pathways for production of fuels and other

useful chemical commodities. The thermodynamic favorability and kinetic stability of the adsorption of syngas molecules on the catalyst surface are critical for efficiently and selectively promoting the hydrogenation reaction [63]. In fact, it requires an excellent catalyst material which being thermally stable, active and selective for the desired reaction. Historically, metal-based catalysts have been widely investigated and been utilized for hydrogenation reaction. They typically demonstrate good catalytic activity and selectivity for the reaction [60-62], however, they are expensive and often deactivated by oxidation. Copper-based catalysts [62] have poor thermal stability, thus, are not suitable for high-temperature reactions without a thermal stabilizer. Cerium-based catalysts [64] have also shown good activity and selectivity for CO_2 hydrogenation process, but are easily deactivated by a small coverage of deposited carbon. Therefore, there is a need to develop a catalyst material, which has superior properties for syngas conversion than Cu-based/Ce-based materials.

Two-dimensional (2D) hexagonal boron nitride (*h*-BN) has received considerable interests in research owing to its novel properties for various applications [65]. Structurally analogous to graphene, single-layer *h*-BN has B and N atoms, which arranged in a hexagonal lattice and bound together by strong covalent bonds. Single-layer *h*-BN is a wide bandgap material with the high chemical stability [20]. The unique physical and chemical properties of the single-layer *h*-BN have made possible for its potential usage in a wide variety of applications such as electronics [66], optoelectronics [12], photo-catalysis [67], and catalysis [14, 65]. The *h*-BN system is metal-free and thermally stable material, and therefore can serve as a metal free catalyst for hydrogenation of CO/CO_2 even at high-temperature. To probe the catalytic properties

of *h*-BN toward such hydrogenation, it is therefore very important to gain fundamental insights into interaction between *h*-BN and syngas.

Pristine *h*-BN is a chemically inert material owing to the lack of dangling bonds [68]. It therefore calls for systematic investigation to find prudent ways to activate the basal plane of *h*-BN. In terms of the chemical inertness of the basal plane, *h*-BN and MoS_2 including other 2D materials (graphene [69], $MoSe_2$ [70], WS_2 [71] etc.) are chemical inert materials. As similar to the case of MoS_2 [16, 23, 27, 72-74], it is known from the prior studies that the basal plane can be activated by the creation of defects [75, 76], or the deposition of metal atoms or molecules [77-80], or the creation of grain-boundaries [81], or the application of strain to the defective surface [82]. Specifically, alike to the case of single-layer defect-laden MoS_2 (with sulfur vacancies), which catalyze the hydrogenation of syngas to alcohol [16], the basal plane of the single-layer *h*-BN can be chemically activated for hydrogenation reaction when there are point or line defects on the surface. Indeed, a combined experimental and theoretical study [14] has shown that the defect-laden *h*-BN efficiently catalyzes the propane hydrogenation, thus suggesting its possible catalytic applications in a wide variety of industrially important hydrogenation reactions. However, the in-depth understanding of the competitive catalytic sites as well as the electronic properties modified by syngas is in question.

We perform DFT-based first-principles calculations of the adsorption of syngas on the *dh*-BN substrate with nitrogen vacancy (V_N), boron vacancy (V_B), stone-wales (SW), and nitrogen substituted by boron (B_N). To probe the reactivity of the *h*-BN substrates with these defects, we compare the adsorption characteristics of syngas molecules. We examine the favorable sites and orientation of these molecules on those *dh*-BN substrates. We analyze the

unique local geometry and electronic structure of *dh*-BN that modified by adsorbed molecules (H_2, CO and CO_2). Based on the DFT-calculated energetics for syngas-adsorption, we show that the *h*-BN with nitrogen vacancy may serve as a potential metal-free catalyst material for hydrogenation of CO/CO_2.

3.2 Calculation Methods

All calculations are performed by using spin-polarized density functional theory (DFT) method, implemented in Quantum Espresso Code [25]. We use the vdW-DF2 functional [46] for exchange-correlation of electrons. For each atom in our considered systems herein, generated according to the theoretical framework of PAW method [54, 55] for interaction between electrons and nuclei. We use the plane wave basis set with kinetic energy cutoff of 45 Ry. We construct a (6x6) supercell of single layer hexagonal boron nitride (*h*-BN) with periodic boundary conditions and a vacuum of 20 Å to avoid the spurious electrostatic interaction between periodical images. To model a defect-laden *h*-BN system (so-called *dh*-BN), we remove either a boron/nitrogen atom or substitute a nitrogen atom by a boron atom or rotate a B-N bond by 90 degree. The relaxed structures of our model systems of *h*-BN with various defects, namely, nitrogen vacancy (V_N), boron vacancy (V_B), Stone Wales (SW) and nitrogen substituted by boron (B_N) are shown in Figure 3.1. To investigate the adsorption characteristics of H_2, CO and CO_2 we place single molecule at the defect site and at the neighboring atoms near defect sites (We present only the lowest-energy adsorption structures). All atoms of *dh*-BN systems with and without molecules and of the isolated molecules, under our investigation, are relaxed until the energy converges to 10^{-6} eV, the residual force on each atom reaches below 0.005 eV/Å. For

calculations of geometry relaxation and of electronic density of states, we use one k-point and 12×12×1 k-point mesh to sample the Brillouin zone, respectively. The adsorption energy is defined as $E_{ads} = E_{Molecule/dh-BN} - \{E_{Molecule} + E_{dh-BN}\}$, where,$E_{Molecule/dh-BN}$, $E_{Molecule}$, E_{dh-BN} are the total energy of the molecule on *dh*-BN, isolated molecule, and *dh*-BN system, respectively. We calculate charge density difference upon adsorption of molecules on *dh*-BN using: $\Delta\rho = \rho_{Molcule/dh-BN} - (\rho_{Molcule} + \rho_{dh-BN})$, where $\rho_{molcule/dh-BN}$, ρ_{dh-BN}, and $\rho_{Molcule}$ are charge density of the molecule on *dh*-BN, *dh*-BN system, and isolated molecule, respectively. We calculate charge on each atom using Löwdin's approach [83] and thus estimate charge transfer between molecules and *dh*-BN systems.

3.3 Results and Discussions

3.3.1 Geometrical and Electronic Structure of *dh*-BN

We present geometry of considerable four kinds of *dh*-BN: V_N, V_B, SW, and B_N in Figure 3.1. To explore their electronic structures, we show the density of states of each defects in Figure 3.2.

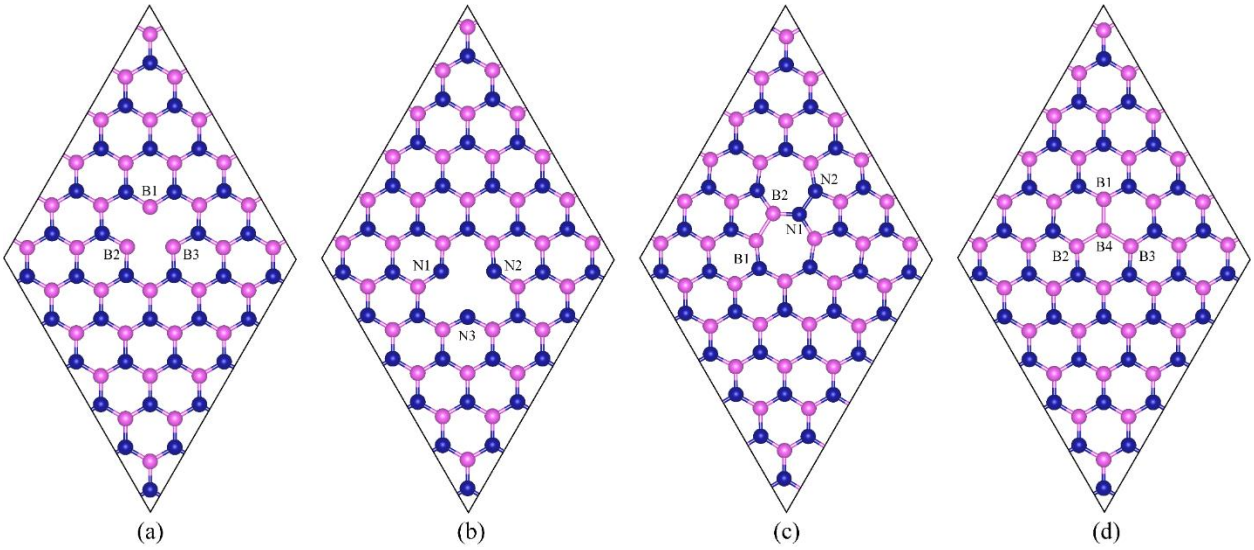

Figure 3.1 Schematic representation of *h*-BN model systems with defects: (a) V_N, (b) V_B, (c) SW, and (d) B_N.

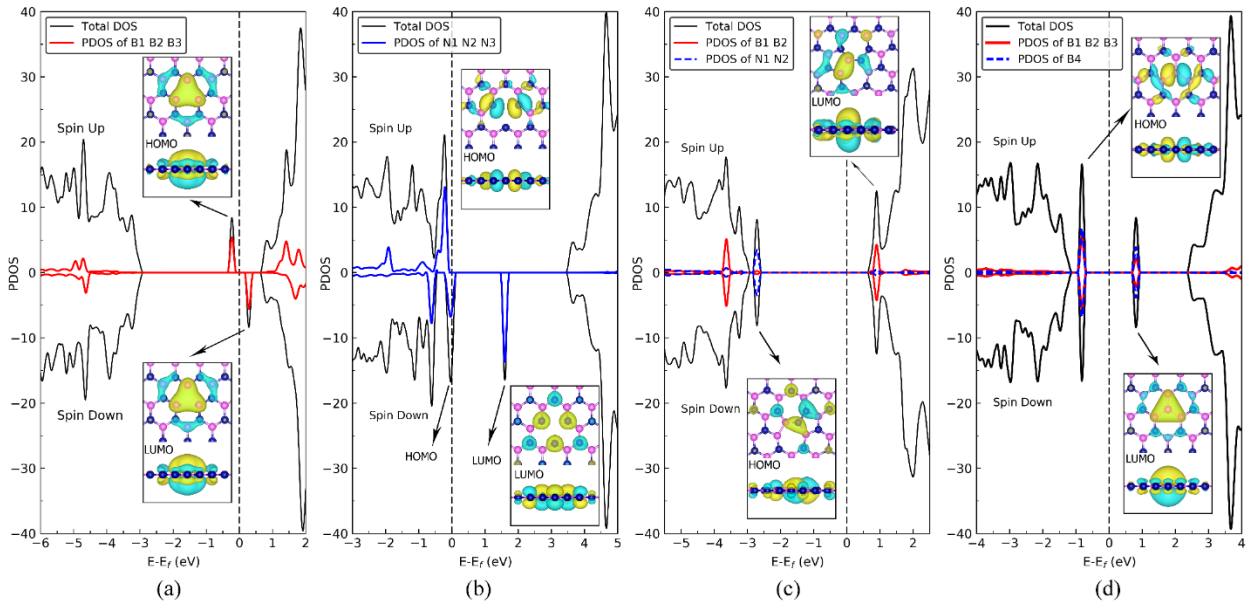

Figure 3.2 The Spin-polarized projected density of states (PDOS) of the respective *dh*-BN systems with defects: (a) V_N, (b) V_B, (c) SW, and (d) B_N. Within the PDOS, there are wave function of the defect states with isosurface value of 0.001 e/Å.

3.3.1.1 Nitrogen vacancy (V_N)

The presence of a nitrogen vacancy on the *h*-BN surface leads to the local geometrical change (Figure 3.1 (a)). The distance between B and N atoms ($d_{(B1/B2/B3-N)}$) is 1.455 Å, which is almost same to 1.454 Å of the pristine *h*-BN whereas the angle between N, B and N atoms ($\theta_{(N-B1/B2/B3-N)}$) is changed from 120° to 116.4° (3% change). Also, the $d_{(N-N)}$ is changed from 2.520 to 2.471 Å (1.9 % change). Since B1/B2/B2 lose a neighboring N atom, these atoms have dangling bonds and laterally displaced forwards the N atoms by 0.002 Å.

From spin-polarized calculations of electronic density of states in Figure 3.2 (a), we find that *dh*-BN (V_N) is the spin-polarized system and that such spin-polarization effect arises from the unpaired electrons owing to the N vacancy. There are two mid-gap states, one is spin-up and the other one is spin-down. The spin-up mid-gap states preformed as the highest occupied molecular orbital (HOMO), and the spin-down mid-gap states preforming as the lowest unoccupied molecular orbital (LUMO). Looking at the wave function of HOMO and LUMO, we can clear find they have the same geometry and preformed π-type orbital, which is hybridized from the B1/B2/B3 atoms and surrounding N atoms and B atoms. Via PDOS of B1/B2/B3 atoms in red curve, we find they make the most contribution to the mid-gap states, indicating B1/B2/B3 are main active sites. So with help of PDOS and wave function in Figure 3.2 (a), we find mid-gap defect states, both spin-up (HOMO) and spin-down (LUMO), near E_F associate with dangling bonds, which can facilitate the adsorption of molecules.

3.3.1.2 Boron vacancy (V_B)

The existence of a boron vacancy on single-layer *h*-BN leads to geometrical change locally (Figure 3.1 (b)): the distance between N and B atoms ($d_{(B-N1/N2/N3)}$) is changed from 1.455

Å to 1.411Å (3.0% change) and the angle between B, N and B atoms ($\theta_{(B\text{-}N1/N2/N3\text{-}B)}$) is changed from 120° to 126.8° (5.7% change). While the distance between N atoms, i.e. $d_{(N\text{-}N)}$, is changed from 2.520 Å to 2.672 Å (6% change). The *dh*-BN (V_B) system possesses the spin-polarized behavior, as indicated by the calculated spin-up and -down density of states in Figure 3.2 (b). The presence of B vacancy leads to the unsaturation of bonds for the nearest-neighboring N (N1, N2, and N3) atoms, and these atoms' electrons become unpaired. To electronically stabilize the *dh*-BN (V_B) by itself, these electrons become aligned in different states with both spin-up and spin-down, corresponding to different energies (Figure 3.2 (b)). The HOMO orbital in the spin-down channel showed as an σ-type orbital, locating at near the valence band edge of the *h*-BN system. The LUMO preforming a π-type orbital in spin-down character above E_F. Via PDOS of N1/N2/N3 atoms in blue curve Figure 3.2 (b), we find states of N1/N2/N3 atoms mainly made up HOMO and LUMO atoms mostly, which shows N1/N2/N3 atoms are main active sites for molecule adsorption.

3.3.1.3 Stone–Wales (SW)

The defect Stone-Wales (SW) can be created by rotation of a B–N bond by 90° around its midpoint, shown in Figure 3.1 (c). The bond length of B1-B2, B2-N1, N1-N2 are 1.671 Å, 1.358 Å and 1.466 Å, respectively. The electronic structure of *dh*-BN (SW) presented via PDOS in Figure 3.2 (c). It is clearly showed that there are two occupied (one is spin up and the other one is spin down) and two unoccupied defect states (one is spin up and the other one is spin down). The unoccupied defect states below the fermi level is partly contributed by the B1 and B2 atoms, the reset are contributed from the atoms surround B1 and B2 atoms (PDOS of LUMO orbitals). In addition, the occupied defect states above the fermi level are coming from N1 and N2 atoms

(PDOS of HOMO orbitals). Defect states which above the fermi level are σ-type mainly contributed by p_x and p_y orbitals from the B–B bond [84].

3.3.1.4 B substitution for N (B_N)

A boron atom can substitute for a nitrogen atom to form B substitution for N as B_N. For *dh*-BN (B_N) in Figure 3.1 (d), the bond lengths of B-B and N-B are 1.588 Å, 1.439 Å. The PDOS plot obtained for *dh*-BN (B_N) clearly showed its large-gap semiconductor properties with defect-related gap states, shown in Figure 3.2 (d). Boron has two fewer valence electrons than nitrogen which providing the dangling bonds. In the defect levels below and above the fermi level, B4 make bigger contribution than sum of the B1, B2, and B3 atoms. H. Choi et al [85] has ready analyzed electronic properties of boron nitride nanotube with B_N. In our case, B4 atoms and its surrounding boron atoms of the single layer *dh*-BN (B_N) has closer geometry to boron nitride nanotube with B_N, indicating the similar electronic properties of B_N.

Using partial charge density analyses, we can find the B_N defect introduces the unoccupied in the middle of the energy gap (LUMO orbital in Figure 3.2 (d)), and occupied defect states near the valence band edge. The HOMO is σ-type and the LUMO, similar structure in comparison with the structure of orbitals of the nanotube with B_N [85].

3.3.2 Hydrogen molecule on *dh*-BN

After discussing the geometries and electronic proprieties of *dh*-BN systems, we focus on the adsorption behaviors of H_2 molecule on *dh*-BN systems since syngas H_2 is a key molecule in CO and CO_2 hydrogenation reaction. Figure 3.3 shows the corresponding geometries of H_2 on *dh*-BN with V_N, V_B, SW and B_N.

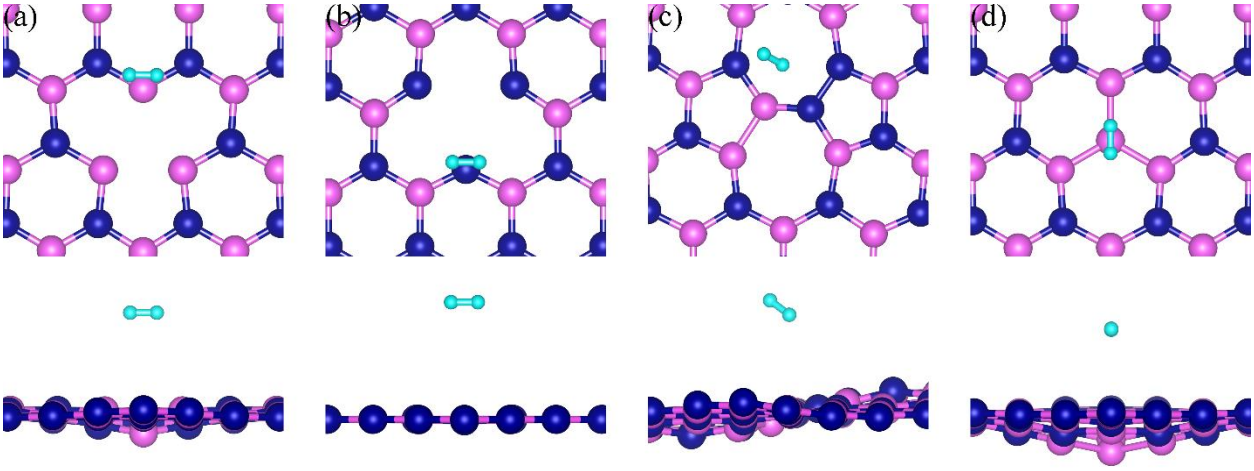

Figure 3.3 Optimized structures of H_2 adsorbed at the favorable sites of *h*-BN with a) V_N, b) V_B, c) SW, and d) B_N. The magenta, blue, white balls represent the B, N and H atoms, respectively. The top and bottom panel shows the top and side views, respectively.

The bond length of H-H of H_2 on all four kinds of *dh*-BN is 0.737 Å, which is almost same to H-H of 0.735 Å of gas phase H_2. The distance $d_{(H-B)}$ for the case of H_2 on *dh*-BN(V_N), *dh*-BN(SW) and *dh*-BN(B_N) are 3.359 Å, 3.267 Å, and 3.357 Å, respectively. The distance $d_{(H-N)}$ for the case of H_2 on *dh*-BN (V_B) is 3.285 Å. We find that H_2 molecule only physical adsorption on single layer *dh*-BN (V_N, V_B, SW and B_N respectively) with the adsorption energy of -0.25 eV, -0.04 eV, -0.20 eV and -0.25 eV. From the Löwdin charge analysis [83], the electron transfer from the defected surfaces to H_2 gas molecules are very small (0.014, 0.011, 0.015, and 0.010 e, on V_N, V_B, SW and B_N, respectively), also confirming the physisorption type result in the negligible electron transfer.

3.3.3 Two Atomic Hydrogens on *dh*-BN

Since H_2 cannot adsorption in molecular type on *dh*-BN with V_N, V_B, SW and B_N, we turn to look at the adsorption of two atomic hydrogens on *dh*-BN systems. Binding behavior of two adsorbed atomic hydrogens (2H) on these four types of *dh*-BN substrates are performed with

the corresponding geometries are shown in Figure 3.4. The geometries of most stable adsorption sites are similar to that in previous work by Nash. et al.'s [14]. What is different here is that we put spin-polarized correction in our calculation since V_N and V_B are spin-polarized systems. The calculated parameters are summarized in Table 3.1, including the adsorption energy, H-H distance, and the distance of formed B(N)-H bond.

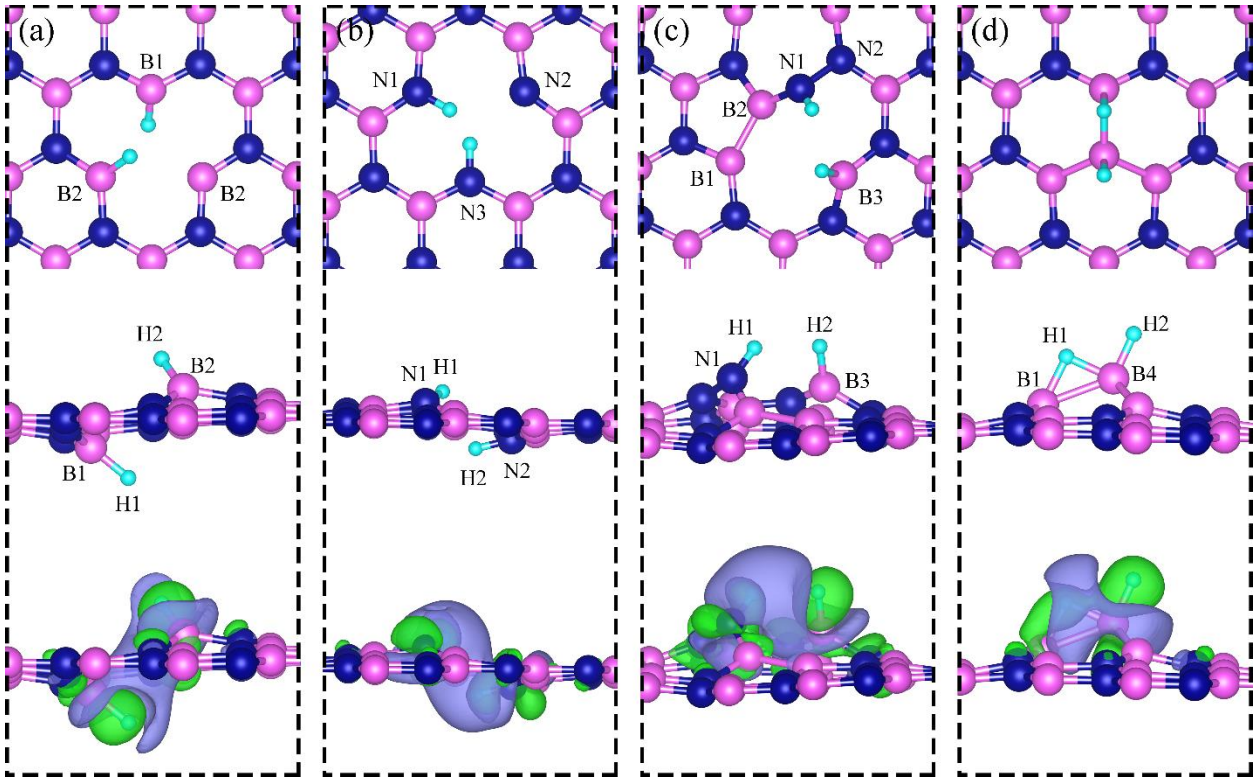

Figure 3.4 DFT-Optimized structures of two hydrogen atoms adsorbed at energetically favorable sites on single layer *dh*-BN with a) V_N, b) V_B, c) SW, and d) B_N. The magenta, blue, cyan balls represent the B, N and H atoms, respectively. The top and middle panel shows the top and side views, respectively. Bottom panel: the corresponding side views of the geometric structures with the charge density difference. The green and violet isosurfaces with isovalue of = ±0.003 e/Å^3, represent the accumulation and depletion of charge, respectively.

On *dh*-BN (V_N), two hydrogen atoms prefer to bound to B atoms near N vacancy in a way that the difference in their z coordinates is 2.934 Å (Figure 3.4 (a)). The most stable

adsorbed two hydrogen atoms (2H) on V_N has the asymmetric geometry with the adsorption energy of -1.79 eV, where one hydrogen stays up to the surface and the other one stays at down to the surface. For 2H-*dh*-BN (V_B) in Figure 3.4 (b), 2H prefer to attach to N atoms near B vacancy with the difference in their z-position of 1.490 Å. The adsorption energy of 2H on *dh*-BN (V_B) is -4.73 eV, an extremely exothermic process. For two hydrogens adsorption on *dh*-BN (SW), 2H prefer to stay at the same side of SW shown in Figure 3.4 (c), where one hydrogen attaches to B3 while the other attaches to N1. We find that the adsorption of 2H on SW break the bond of B3-N1, which $d_{(B3\text{-}N1)}$ = 2.632 Å largely increased from the 1.487 Å of the *dh*-BN(SW). This adsorption is an endothermic process of +1.04 eV. This may because that the mid-gap states (defect states) are too closer to conduction band or valence band of *dh*-BN (SW). For two H atoms on *dh*-BN (B_N), one hydrogen prefers to adsorb on the center boron atom (B4) whereas the other hydrogen prefers to stay at the bridge between B1 and B4, shown in Figure 3.4 (d). The adsorption energy of this configuration is -1.68 eV.

Table 3.1 The adsorption energy and geometrical parameters for adsorption of 2H on *dh*-BN.

	Defects	Sites	E_{ads} (eV)	Distance between atoms (Å)
2H	V_N	B1, B2	-1.79	$d_{(H-H)}$=3.086, $d_{(H1-B1)}$ =1.189, $d_{(H2-B2)}$=1.190
	V_B	N1, N2	-4.73	$d_{(H-H)}$=1.869, $d_{(H1-N1)}$=1.012, $d_{(H2-N2)}$ =1.009
	SW	B3, N1	+1.04	$d_{(H-H)}$=1.687, $d_{(H1-N1)}$ =1.004, $d_{(H2-B3)}$=1.190, $d_{(B3-N1)}$ = 2.632
	B_N	B1, B4	-1.68	$d_{(H-H)}$=1.757, $d_{(H1-B4)}$ =1.207, $d_{(H2-B4)}$= 1.274, $d_{(H2-B2)}$=1.315, $d_{(B1-B4)}$ =1.858

We next examine the charge density difference (CDD) (shown in Figure 3.4 Bottom panel) and PDOS (shown in Figure 3.5) to have a clear look at the interaction between 2H and *dh*-BN systems. We find the hydrogen adsorbed on boron atom or nitrogen atom of *dh*-BN via the H-B or H-N forming. From PDOS in Figure 3.5, we find that adsorption of 2H has small effect on changing the electronic properties of *dh*-BN. Adsorption energy of two hydrogens on *dh*-BN with V_N, V_B, SW and B_N are -1.79 eV, -4.73 eV, 1.04 eV and -1.68 eV, which are different from that reported by Nash et.al [14] of -1.43 eV, -4.95 eV, 0.62 eV and -1.77 eV. Overall, our calculations indicate that atomic hydrogen atoms most strongly adsorb on the *dh*-BN (V_B) system (E_{ads}=-4.73 eV) and that 2H are not favorable to adsorb on the *dh*-BN (SW) system (E_{ads}=+1.04 eV).

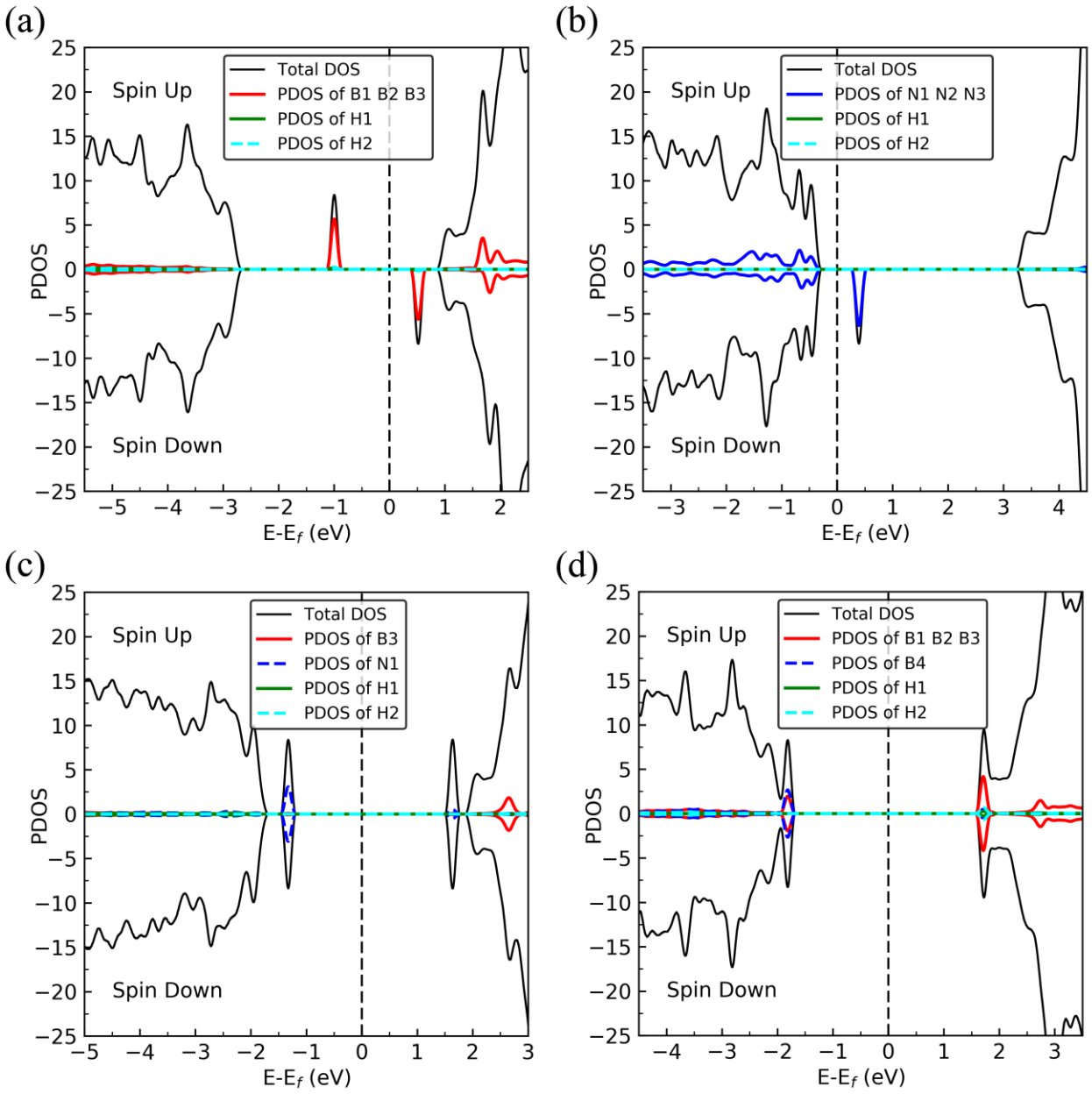

Figure 3.5 Spin-polarized total density of states (TDOS) (black line), spin-polarized PDOS of defect area in (red line or blue line) and spin-polarized PDOS adsorbed two hydrogens (green line and cyan line) of 2H-*dh*-BN with (a) V_N, (b) V_B, (c) SW, and (d) B_N, respectively. The position of the Fermi level (E_F) is indicated by dashed line.

3.3.4 CO on *dh*-BN

Carbon monoxide (CO) is one of the major common toxic gases in the atmosphere, and syngas CO is a very import reactant in reactions of methanol and ethanol synthesis. Here, we present the geometry structure of CO adsorption on the V_N, V_B, SW, and B_N in Figure 3.6 and we use PDOS, charge density difference and Löwdin charge transfer analyze to study their electronic structures, which can help us has a deep understanding of CO adsorption on *dh*-BN.

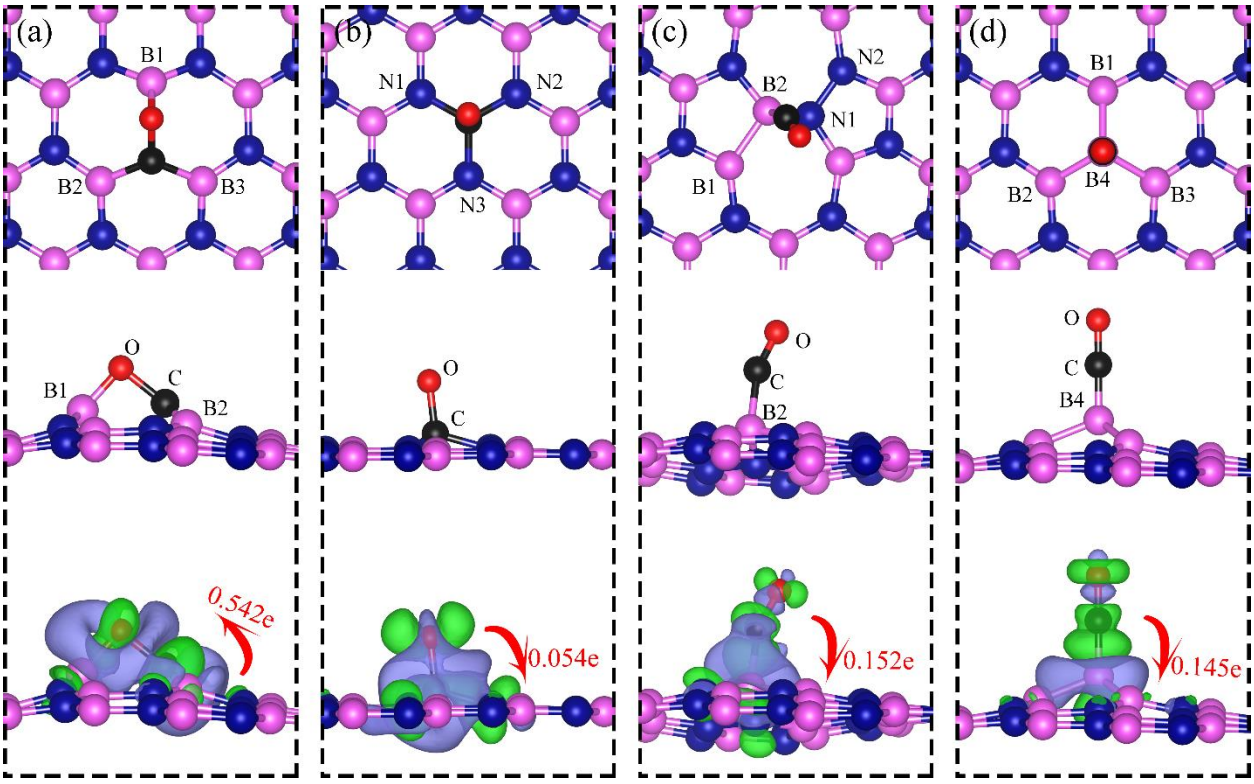

Figure 3.6 Top and side views of the most energetically favorable configurations of adsorbed CO on the *dh*-BN with a) V_N, b) V_B, c) SW, and d) B_N. The magenta, blue, black and red balls represent the B, N, C, and O atoms, respectively. The top and middle panel shows the top and side views, respectively. Bottom: the corresponding side views of the geometric structures with the charge density difference. The green and violet isosurfaces with isovalue of = ±0.003 e/Å^3, represent the accumulation and depletion of charge, respectively. The red arrow shows the electron transfer in direction and value.

3.3.4.1 CO adsorption on dh-BN (V_N).

On *dh*-BN (V_N), CO binds at the defect sites with O atom binding with B1 atom and C binding with two B2 and B3 in Figure 3.6 (a), whose geometry is similar with previous reports [86, 87]. Due to this adsorption, the B1 atom was drawn out about 1Å of the surface by O atom. The bond length of C–O increases from 1.143 Å (gas phase) to 1.403 Å (adsorbed), while $d_{(C-B2)}$ ($d_{(C-B3)}$) being measured to be 1.529 Å and $d_{(O-B)}$ being 1.417 Å. The adsorption energy of CO on *dh*-BN (V_N) is -3.64 eV. The Löwdin charge analysis shows that 0.542 e transferred from the surface to the CO molecule. To locate the area where electron transfer occurs, we perform charge density difference (CDD) analyses on the adsorption of CO on *dh*-BN (V_N). As shown in the bottom panel of Figure 3.6 (a), a sizable electron density accumulation (green region) appeared between the B atom and C atom, and between the B atom and O atom, which verifies the bonding formation of the B-C bond and B-O bond. A loss of electron density (violet region) is shown around the C-O bond, indicating that adsorption weakens the C-O bond, which can be also be verified by the enlargement of the C-O bond from the gas phase. In Figure 3.7 (a), which contains PDOS of CO adsorption on *dh*-BN (V_N), the orbital mixing between the occupied states of CO molecules (in red line) and the states of B atoms (around the vacancy in blue line). This obvious overlap of states of CO and V_N indicates the strong chemisorption of the CO molecule caused by dangling bonds of the B atoms around the vacancy site. In addition, the density of states peaks shift toward the higher energy since the charge transfer takes place from the *dh*-BN (V_N) surface to the CO molecule by 0.542 e. Therefore, CO is favorable on *dh*-BN (V_N) by chemical adsorption.

3.3.4.2 CO adsorption on dh-BN (V_B)

For CO adsorption on *dh*-BN (V_B) in Figure 3.6 (b), the most stable adsorption configuration is that when CO binds to N1, N2 and N3 atoms in vertical orientation via C-N bond forming shown, which is similar to that previously reported [86, 87]. The adsorption energy is -4.66 eV, which indicates a very strong binding. In this configuration, C–O bond length increases from 1.143 to 1.386 Å, while $d_{(C-N)}$ measured to be 1.501 Å. The Lödwin charge analysis shows that about 0.054 e transferred from the CO molecule to the surface. In bottom panel of Figure 3.6 (b), a sizable electron density accumulation (green region) appeared between the Carbon and N atoms, which verifies the strong interaction between the CO molecule and N atoms around the vacancy. A loss of electron density (violet region) is surround between C atom and O atom, which shows the weakened C-O bond (also can be verified by enlarge of length of C-O bond). In Figure 3.7 (b), PDOS of CO adsorption on *dh*-BN (V_B) shows the orbital mixing between the occupied states of CO molecules and orbitals of B atoms observed at around the Fermi level, indicating the chemisorption of CO on the *dh*-BN (V_B). We can see the unoccupied states shifts toward the lower energy where very close to the Fermi level after CO adsorption, verified by Lödwin charge analysis, which it shows 0.054e transferred from the surface to the CO molecule.

3.3.4.3 CO adsorption on dh-BN (SW)

For CO adsorption on *dh*-BN (SW) shown in Figure 3.6 (c), CO adsorbs at the B site pulling the B atom out from the surface a lot. In this geometry, the bond length of C-O is 1.150 Å and the bond length of C-B is 1.636 Å. Similar configuration has been obtained in previous study [88], leading to a significant change in local geometry with the adsorption energy of -0.58

eV, which is different from our calculated E_{ads}=0.25 eV indicating an endothermic process. Thus our van der Waals implemented (via vdW-DF2) computational results show that defect states of *dh*-BN (SW) are far from each other and one is very close to CBM and the other is very close to VBM, shown in Figure 3.2 (c), which is the reason that *dh*-BN (SW) is not favorable for adsorption of the molecules. Lödwin charge analysis shows 0.152 e transferred from CO molecule to the surface. As CDD of CO on *dh*-BN (SW) shown in the bottom panel of Figure 3.6 (c), a sizable electron density accumulation (green region) appeared between the B atom and C atom, which indicates the formation of B-C bond. However B-C bond length is 1.636, longer than the cases of CO on V_N and V_B defects, so indicates CO on *dh*-BN (SW) shows relatively weaker interaction (weaker interaction can also be verified from the its adsorption energy). In PDOS in Figure 3.7 (c), the conduction band moves toward the lower energy and that the valence band shifts toward the higher energy, thus molecule (CO)-surface interaction leads to shirking of the energy gap of the *dh*-BN. Still, the energy gap is large, thus lacking the electronic states closer to the Fermi level. Therefore, although the *dh*-BN with SW defect is not favorable for CO adsorption, the interaction of CO with the *dh*-BN(SW) surface made the unoccupied defect level move from VBM to the fermi level inside the gap, and may activate some intermediate reactions involving CO.

3.3.4.4 CO adsorption on dh-BN (B_N)

For the case of CO on *dh*-BN (B_N) in Figure 3.6 (d), CO perpendicularly binds at the top of the central B atom (labeled as B4) of the surface with an adsorption energy of -2.70 eV. The calculated $d_{(C–B)}$ and $d_{(C-O)}$ are is 1.444 Å and 1.163 Å (elongated by 0.02 Å from that in gas-phase), respectively. From the CDD of CO on *dh*-BN (B_N) in the bottom panel of Figure 3.6 (d),

a sizable electron density accumulation (green region) between the B and C atoms, which verifies the strong interaction between the CO molecule and its neighboring B atoms around the defect area. A small loss of electron density (violet region) is over the C-O bond, indicating the weakened C-O bond, also verified by elongation of C-O bond changed from 1.143 Å to 1.163 Å. A large loss of electron density (violet region) is over the B4-B1, B4-B2 and B4-B3 bonds. In all, we can see electron transfer from C-O and B-B leads to the formation of the new C-B bond (net 0.145 e transferred from CO to surface via Lödwin charge analysis). After CO adsorption on *dh*-BN with B_N, the density of states peaks shifts toward the lower energy shown in Figure 3.7 (d), and the defect states disappear within the energy gap. This provides insights to us that B_N defect is not suitable for reactions if there is CO involving as intermediate species. The adsorption of CO accompany the disappearance of mid- gap states, since there are no dangling bonds for more molecules to adsorb, thus passivating the catalytic activity of *dh*-BN (B_N).

Table 3.2 The adsorption energy and geometrical parameters for adsorption of CO on *dh*-BN.

Molecules	Defects	E_{ads} (eV)	Bond length (Å) and Bond angle (°)
CO	V_N	-3.54	$d_{(C-O)}$ =1.403, $d_{(C-B1)}$ =1.529, $d_{(O-B1)}$ =1.417, $\theta_{(C-O-B1)}$=93.6°
	V_B	-4.89	$d_{(C-O)}$=1.386, $d_{(C-N1)}$=1.493, $\theta_{(O-C-N1)}$=103.9°
	SW	0.25	$d_{(C-O)}$=1.150, $d_{(C-B2)}$ =1.636, $\theta_{(O-C-B2)}$=159.0°
	B_N	-2.56	$d_{(C-O)}$=1.163, $d_{(C-B4)}$ =1.444, $\theta_{(B4-C-O)}$=179.9°

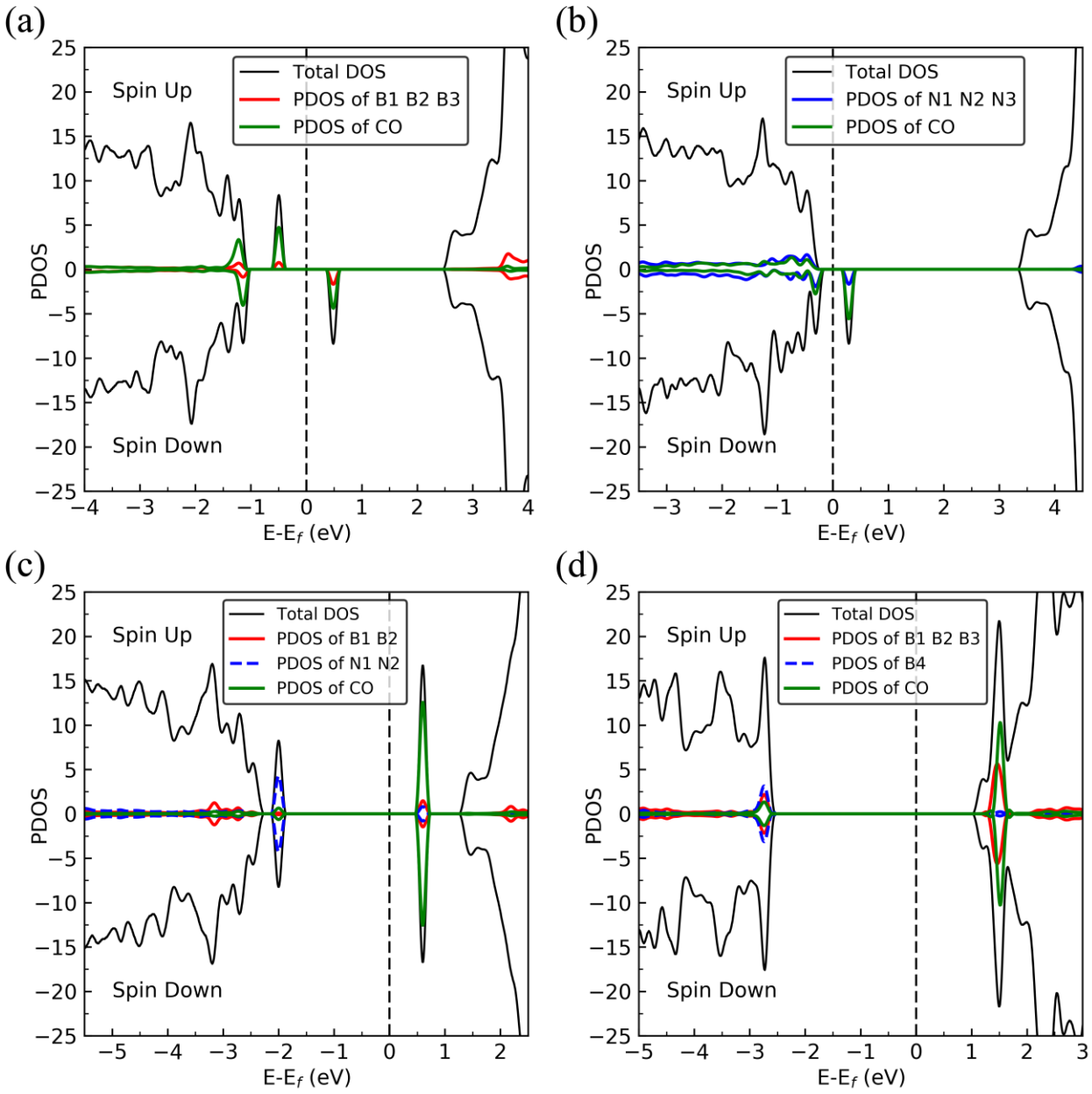

Figure 3.7 Spin-polarized total density of states (TDOS) (black line), spin-polarized PDOS of defect area in (red line or blue line) and spin-polarized PDOS adsorbed CO (green line) of CO-*dh*-BN with (a) V_N, (b) V_B, (c) SW, and (d) B_N, respectively. The position of the Fermi level (E_F) is indicated by dashed line.

3.3.5 CO_2 on *dh*-BN

Carbon dioxide (CO_2) is one of greenhouse gas, which brings concerns on climate changing. The reduction of CO_2 is an important topic in today's science. Here, we present the geometry structure of CO adsorption on the V_N, V_B, SW, and B_N in Figure 3.8 and summarized adsorption energy and parameters in Table 3.3. With PDOS, charge density difference and Löwdin charge transfer analysis, we can have a better understand between CO_2 and *dh*-BN.

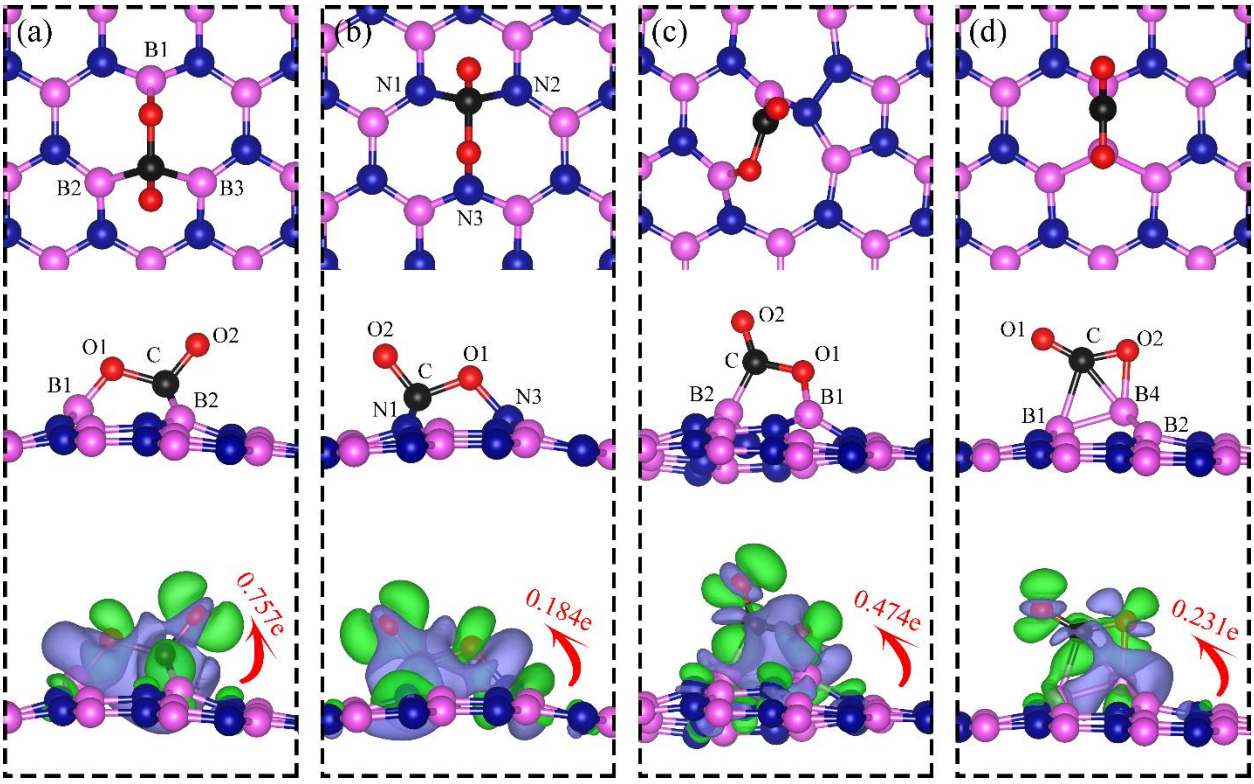

Figure 3.8 Top and side views of the most energetically favorable configurations of adsorbed CO_2 on the *dh*-BN with a) V_N, b) V_B, c) SW, and d) B_N. The magenta, blue, black and red balls represent the B, N, C, and O atoms, respectively. The top and middle panel shows the top and side views, respectively. Bottom: the corresponding side views of the geometric structures with the charge density difference. The green and violet isosurfaces with isovalue of = ±0.003 e/Å^3, represent the accumulation and depletion of charge, respectively. The red arrow shows the electron transfer in direction and value.

Table 3.3 The adsorption energy and geometrical parameters for adsorption of CO_2 on *dh*-BN.

Molecules	Defects	E_{ads} (eV)	Bond length (Å) and Bond angle (°)
CO_2	V_N	-1.97	$d_{(C-O1)}$=1.438, $d_{(C-O2)}$=1.311, $d_{(C-B2)}$ =1.672, $d_{(O1-B1)}$ =1.382, $\theta_{(O1-C-O2)}$=113.7°
	V_B	-0.69	$d_{(C-O1)}$=1.409, $d_{(C-O2)}$=1.353, $d_{(C-N1)}$ =1.496, $d_{(O1-N3)}$=1.446, $\theta_{(O1-C-O2)}$=107.1°
	SW	0.43	$d_{(C-O1)}$=1.407, $d_{(C-O2)}$=1.209, $d_{(C-B2)}$ =1.581, $d_{(O1-B1)}$=1.413, $\theta_{(O1-C-O2)}$=121.9°
	B_N	-0.21	$d_{(C-O1)}$=1.206, $d_{(C-O2)}$=1.273, $d_{(C-B1)}$ =1.989, $d_{(C-B4)}$ =1.807, $d_{(O2-B4)}$=1.661, $\theta_{(O1-C-O2)}$=139.6°

3.3.5.1 CO_2 adsorption on dh-BN (V_N)

On *dh*-BN (V_N), CO_2 binds at the defect sites, with the adsorption energy of -1.96 eV, a strong chemisorption of the CO_2 molecule caused by dangling bonds of the B atoms around the vacancy site. In this Figure 3.8 (a), the B1, B2 and B3 atom protrudes a little out of the surface, and CO_2 lies in three boron sites near the vacancy with $d_{(O1-B1)}$, and $d_{(C-B2)}$ ($d_{(C-B3)}$) of 1.382Å and 1.672Å, whereas the O1-C-O2 angle is 107.1º. The $d_{(C-O1)}$ and $d_{(C-O2)}$ are 1.438 Å and 1.311 Å (both longer than that 1.172Å of gas phase CO_2), indicating that the original C-O bond is stretched upon interaction between CO_2 and *dh*-BN (V_N). The Lödwin charge analysis shows

that about 0.757 e transferred from the surface to the molecule. By CDD of CO_2 on *dh*-BN (V_N) in the bottom panel of Figure 3.8 (a), a sizable electron density accumulation (green region) appeared between the B2 (B3) atom and C atom, same for between the B1 atom and the O atom, which verified new bonds B2(B3)-C and B1-C forming. A loss of electron density (violet region) is also evident over the C-O bond, which weakens the C-O bond, also verified by enlarged length of the C-O bond. PDOS of CO adsorption on *dh*-BN (V_N) in Figure 3.9 (a), shows overlap of states mixing between states of CO molecules and the states of B atoms, indicating the chemisorption of CO on the *dh*-BN (V_N) as well as the strong interaction between the molecule and the surface. We also find that the density of states peaks splinted and the group of spin up and down defect levels (almost shown blue) shift toward the lower energy where closer to VBM. This phenomenon indicates B atoms (B1, B2, and B3) near the vacancy becomes less active for molecules adsorption, which can also varied by the charge lost. But we can find the states nearby the CBM is most contributed by states of CO_2 , which showing C atom and O atoms become new active sites favorable for molecule adsorption.

3.3.5.2 CO_2 adsorption on dh-BN (V_B)

On *dh*-BN (V_B), CO_2 binds at the N sites with the adsorption energy of -0.69 eV shown in Figure 3.8 (b), which has similar configuration to previous report [89]. In this configuration, CO_2 lies in between the three N sites with the $d_{(C-N1)}$ and $d_{(O-N)}$ distance of 1.496 Å and 1.446 Å. The $d_{(C-O1)}$ and $d_{(C-O2)}$ are 1.409 Å and 1.353 Å (longer than that 1.172Å of an isolated molecule), indicating that weaken the original C-O bond. The Lödwin charge analysis shows 0.184 e transferred from the surface to the molecule. From CDD of CO_2 on *dh*-BN (V_B) in Figure 3.8 (b), a sizable electron density accumulation (green region) appeared between the N and C atoms

which verifies new N-C bond forming, but loss of electron density (violet region) between the B and O atoms which means very weak B-O bond, also showed in latter electronic structure study. In PDOS in Figure 3.9 (b), we can see the density of states peaks shifts toward the lower energy and the states are very close to the Fermi level after CO_2 adsorption. Since of number of defects decrease from 3 to 1 currently, and the only one defect level is mostly contributed by CO_2. Therefore, the adsorption of CO_2 let N atoms around the vacancy passivated for molecule adsorption, whereas only at C atoms and O atoms still active for molecules adsorption.

3.3.5.3 CO_2 adsorption on dh-BN (SW)

On *dh*-BN (SW), CO_2 binds at two B sites with adsorption energy of +0.36 eV indicating the adsorption is endothermic. In Figure 3.8 (c), we can find that CO_2 pulls the B atom out from the surface with C-O1 being 1.407 Å and C-O2 being 1.209 Å. The $d_{(C-B2)}$ and $d_{(O1-B1)}$ are 1.581Å and 1.413Å. The Lödwin charge analysis shows 0.474 e transferred from the surface to the molecule. From CDD of CO_2 on *dh*-BN (SW) in Figure 3.8 (c), a sizable electron density accumulation (green region) appeared between the B and C atoms and between the B and O atoms and. A large Loss of electron density (violet region) appears between the B1 atom and B2 atom which indicating weakening of B-B bond of the defect strongly. In PDOS of Figure 3.9 (c), the conduction band moves toward the lower energy and the valence band shifts toward the higher energy similar to the condition of CO on *dh*-BN (SW) which we had discussed. The states of B1, B2, N1, and N2 atoms is still most of the defect levels, whereas states of CO_2 is still very small, indicating the weak interaction between the CO_2 and *dh*-BN (SW) comparing with the situation of other kinds of defects, which also explain why the adsorption of CO_2 on *dh*-BN (SW) is endothermic.

3.3.5.4 CO_2 adsorption on dh-BN (B_N)

On *dh*-BN with B_N in Figure 3.8 (d), the CO_2 molecule undergoes structural distortion to a bent geometry and double-bond breaking of one C=O bond the similar way as CO_2 chemical adsorption on B-rich BNNTs [85]. The O1-C-O2 bond angle is 139.6º, and the broken C-O2 bond is significantly elongated to 1.273 Å on top of the B_N. The position of the defect site B4 is considerably pulled out by 1.083 Å. The CO_2 adsorbs at the B sites with the adsorption energy of -0.21 eV. The length of $d_{(C-O1)}$ is significantly enlarged to 1.206 Å on top of the B_N defect, accompanying with the double-bond breaking. The Lödwin charge analysis shows 0.231 e is transferred from the surface to the molecule. From CDD of CO_2 on *dh*-BN (B_N) in Figure 3.8 (d), a sizable electron density accumulation (green region) appeared between the B and C atoms and between the B and O atoms and. A large loss of electron density (violet region) appears between the B1 atom and B2 atom which indicating weakening of B-B bond strongly. After CO_2 adsorption on *dh*-BN with B_N, the density of states peaks shifts toward the higher energy since the charge transfer takes place from the *dh*-BN (B_N) surface to the CO_2 molecule in Figure 3.9 (d). From the PDOS, we can saw not only the defect levels of B atoms (B1, B2, B3 and B3) in blue but also new defect levels contributed by CO_2 in red. Both of these defect levels provide active sites for molecules or atoms adsorption.

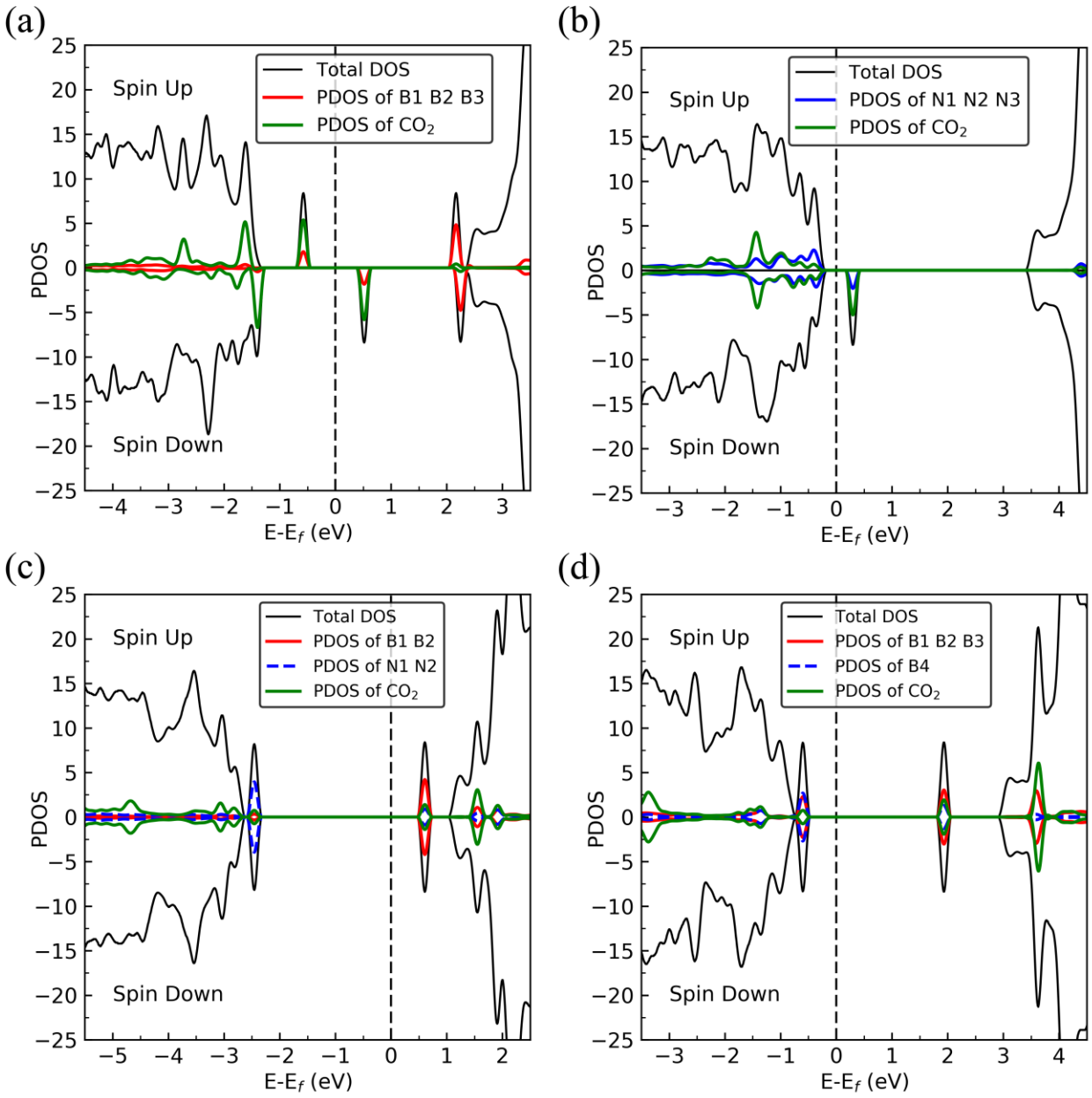

Figure 3.9 Spin-polarized total density of states (TDOS) (black line), spin-polarized PDOS of defect area in (red line or blue line) and spin-polarized PDOS adsorbed CO_2 (green line) of CO_2-*dh*-BN with (a) V_N, (b) V_B, (c) SW, and (d) B_N, respectively. The position of the Fermi level (EF) is indicated by dashed line.

3.3.6 Catalytic Properties of *dh*-BN

Our results suggest that if we use *dh*-BN as catalysts, the H_2 molecule could only dissociative adsorb. We compare 2H, CO, and CO_2 adsorption energy together in Figure 3.10. According to the black line in Figure 3.10, we find adsorption energy of 2H, CO and CO_2 on *dh*-BN(V_N) is at the similar energy level, V_N binding molecules not too strong to block active sites or not too weak to binding in reaction pathway. This shows that *dh*-BN (V_N) can be a potential catalyst for CO_2 and CO hydrogenation. For V_B, adsorption energy showing the red line in Figure 3.10, the 2H adsorption is too strong but for CO_2 adsorption is too weak, indicating *dh*-BN (V_B) may not a good catalyst for CO_2 hydrogenation. For SW in green line in Figure 3.10, 2H, CO and CO_2 on SW are all endothermic processes which showing SW are not energetic favorable for molecules adsorption much less the following reactions steps happening. For B_N, a blue line in Figure 3.10, binding CO_2 is too weak which means B_N could not performing a stable CO_2 adsorption rather than go to next reactions. Also from the PDOS of adsorption of 2H on B_N in Figure 3.5, and the PDOS of CO on B_N in Figure 3.7, we can see numbers mid-gap states peaks decreased to zero, indicating there is no dangling bonds in the band gap for more molecules adsorption. Because these two factors, *dh*-BN (V_N) is not a good catalyst for CO hydrogenation. Our work for catalytic prosperity discussion not need calculating energy barrier just study the electric properties and relations between these adsorption will give a good insight of the potential catalytic of the studied system.

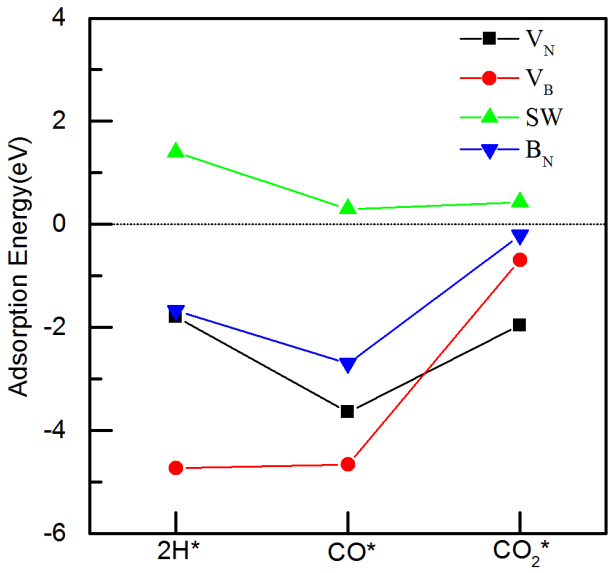

Figure 3.10 Adsorption energy of 2H, CO, and CO_2 on the *dh*-BN with (a) V_N, (b) V_B, (c) SW, and (d) B_N, shows in black, red, green, blue lines, respectively

3.4 Conclusions

Performing density functional theory based calculations, we have examined the propensity of *dh*-BN (with V_N, V_B, SW, and B_N) systems for binding of syngas molecules (H_2, CO, CO_2) and the electronic structures of those systems. We find that, except for H_2, only CO and CO_2 molecules chemisorb on all *dh*-BN substrates. H_2 molecular adsorption on these defects are all physical adsorption, For two hydrogen adsorption on the defect, the most stable adsorption of 2H is on V_B. Both the adsorption energy and PDOS analysis show the CO molecule chemically bonded to V_N, V_B, SW, and B_N, where the covalent interaction between molecules and defect sites formed, which same for CO_2. Adsorption of 2H, CO and CO_2 on SW are all endothermic processes. CO can chemically bonded to B_N with a large adsorption energy whereas CO_2 chemically-adsorption on B_N is very weak.

Our results provide fundamental insights into the interaction of syngas molecules and *dh*-BN, and help prescreen the suitable type of defects to make the basal plane of the *dh*-BN catalytically active for CO and CO_2 hydrogenation reactions. Our calculation results elucidate the detailed mechanism of H_2, CO, CO_2 molecular binding on the *dh*-BN system, which may be of importance not only for fundamental understanding of molecular interaction on *dh*-BN but also for possible applications of *dh*-BN, such as in catalysis. By comparing the adsorption energy of molecules on different *dh*-BN accompany with the analysis on the electronic structures, we predict that *dh*-BN (V_N) is a good candidate catalyst for CO and CO_2 hydrogenation.

CHAPTER 4: SELECTABLE CATALYTIC REDUCTION OF CARBON DIOXIDE TO FORMIC ACID OR METHANOL OVER DEFECT HEXAGONAL BORON NITRIDE: A FIRST-PRINCIPLE STUDY

The hydrogenation of waste gas carbon dioxide into value added molecules could reduce greenhouse gas emission and our dependence on nonrenewable energy sources. By our density functional theory (DFT) based calculations, we have found that nitrogen vacancy (V_N) induced in defect-laden hexagonal boron nitride (*dh*-BN) can effectively activate the CO_2 molecule for hydrogenation. Activation occurs through back-donation to the π^* orbitals of CO_2 from frontier orbitals (defect state) of the *h*-BN sheet localized near a nitrogen vacancy (V_N). Subsequent hydrogenation to formic acid (HCOOH) and methanol (CH_3OH) occur through vacancy facilitated co-adsorption of hydrogen and CO_2. The catalyst prepared from *dh*-BN (V_N) would allow catalytic recovery of value-added molecules.

4.1 Introduction

Carbon dioxide (CO_2) is the main component of all combustion products produced in power generation and transportation. As consumer demands increase the production of CO_2 will also increase. Global carbon dioxide emissions have been increasing. Each year sets a record high. In 2018, CO_2 emissions again hit a record high at 37.1 gig tons [90]. The reduction of emission of this greenhouse gas is of critical importance to the world climate. Popular approaches involve sequestration [91], electrochemical reduction [92], homogeneous [93], and heterogeneous reduction [94, 95]. Each of these approaches has disadvantages. Sequestration is limited to available space, electrochemical reduction is energy intensive, homogeneous reduction

utilizes catalysts that can be difficult to recover, and heterogeneous catalysts are typically transition metal based. The most popular transition metals (save iron) utilized are not abundant. Here we present computational results of reaction pathways and activation energy barriers on a metal-free single layer defect-laden boron nitride with nitrogen vacancy (*dh*-BN (V_N)). Reduction of carbon dioxide to useful molecules presents a solution by providing economic incentive for capturing and utilizing CO_2 instead of disincentives for CO_2 release. A combination of both encourages CO_2 to be viewed as a raw material not as a waste gas.

4.2 Computational Details

DFT calculations were carried out using the Quantum ESSPRESO package [25] employing the projector-augmented wave (PAW) [54, 55] and plane wave basis set methods. We utilized the vdW-DF2 functional [46] for describing electron exchange-correlation interaction. We set cut-off energy for plane-wave expansion at 45 Ry. We construct our simulation supercell with a 6×6 *h*-BN sheet with one N vacancy at the middle and a vacuum of 20 Å to decouple periodical image along the normal direction of the sheet. Considering the large size of supercell, we sampled the Brillouin Zone at the zone center. Structural relaxation is performed for all configurations until the forces acting on each ion are smaller than 0.0002 Ry/Bohr. To calculate reaction energy barriers, we use the Nudged-Climbing image method [59]. As V_N is identified as active site, calculations for reaction energies and barriers are carried out only for V_N defect *h*-BN.

4.3 Results and Discussion

Hexagonal boron nitride has the potential to catalyze multiple reactions, as multiple defect types are possible (Figure 1.1). These defects can produce quite different chemical environments from the Lewis acidity of a nitrogen vacancy (V_N) to the Lewis basicity of a boron vacancy (V_B) defects in the lattice. In fact, boron nitride has been shown to be catalytically active for hydrogenation under reductive conditions [14] and dehydrogenation under oxidative conditions [15]. Although oxidative dehydrogenation may be due to B-O species formed in situ [96], both hydrogenation and dehydrogenation take place on defect sites. In fact the presence of oxygen on defect sites inhibits hydrogenation [97].

4.3.1 Identification of Active Sites for CO_2 Reduction

Defects have been shown to be important in catalytically active solids [98-102]. Some defects in *h*-BN display favorable absorption energies for CO_2 (Table 4.1). Our density functional theory (DFT) based calculations show that CO_2 and H_2 binds to nitrogen vacancy with similar binding energies and that the strength of bindings are not too strongly to prevent CO_2 and H_2 co-adsorption nor too weak to make their adsorption unstable, suggesting nitrogen vacancy is the candidate for as the active site for CO_2 activation. As a result, we investigate only the nitrogen vacancy in this work. The complete reaction pathway and list of all reaction considered in this work are in Figure 4.9 and Table 4.2-4.10, respectively.

Table 4.1 Calculated binding Energy for ethane [103], propene [14] , hydrogen and CO_2 on defects in *h*-BN. Binding to nitrogen vacancies (V_N) is on par with olefin binding energies. The V_N site has been identified as the most likely catalytic site for olefin hydrogenation.

	Binding Energy (eV)			
Defect	Ethene	Propene	Hydrogen	CO_2
V_B	-3.71	-3.69	-4.82	-0.94
V_N	-1.90	-1.76	-1.51	-1.86
B_N	-1.95	-2.05	-1.68	-0.27
SW	-0.23	-0.35	1.02	0.36

4.3.2 CO_2 adsorption and activation

Starting with a physisorbed state (at 3.297 Å above the *h*-BN, with binding energy of -31.20 kJ/mol (-0.32 eV)), the adsorption of CO_2 on a V_N in *dh*-BN proceeds first with the C and one O, each binding to a B atom near the vacancy producing CO_2*(I) shown in Figure 4.1 (* denotes adsorbed species). The process has a low barrier of 14.12 kJ/mol (0.15 eV). After

overcoming a similarly small barrier of 15.27 kJ/mol (0.16 eV), the CO_2* reconfigures such that it binds to all three B atoms in its vicinity (CO_2*(II) in Figure 4.1).

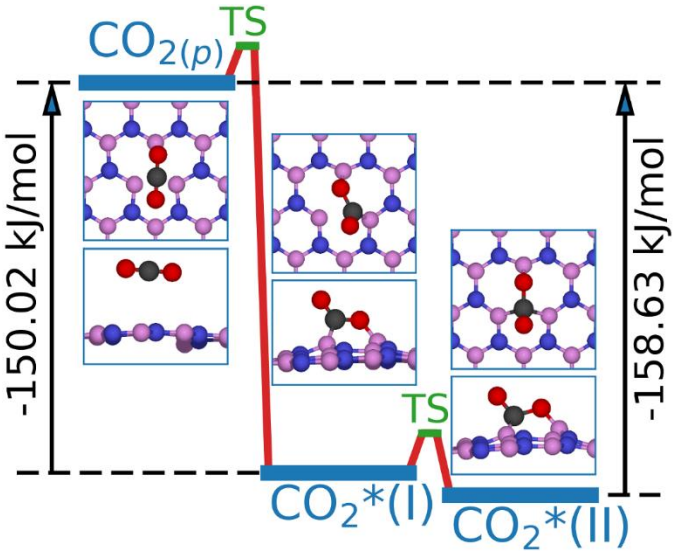

Figure 4.1 Energetic pathway for the adsorption of CO_2 on *dh*-BN with N vacancy. Blue horizontal bars represent states of the gas phase physisorbed $CO_{2(p)}$ (3.29 Å from on *h*-BN), or adsorbed CO_2, CO_2*(I) and CO_2*(II). Small green horizontal bars represent transition states (TS). The inserted cartoons show the top and side views of CO_2 in the three configurations. Blue, pink, black, and red balls represent N, B, C, and O atoms, respectively.

The CO_2 adsorption energy of -186.13 and -194.74 kJ/mol (-1.93 and -2.02 eV) in configurations I and II, respectively, is larger than that typically found on materials used for capturing CO_2: a feature we ascribe to the strong interaction of the frontier orbitals of N defect states (Figure 4.2 (a) and (b)) with the anti-bonding π* molecular orbital of CO_2. In both chemisorbed configurations, the CO_2 molecule is bent (with O-C-O angles of 119.4° and 113.7°, respectively), suggesting a reduction in the C=O bond order and an increase in carbon sp^3 character. Furthermore, there is a reactive, unsaturated O atom with a large negative charge (-0.386 e) in both configurations. In fact, small donation of electron density (0.036 e) from the defect state to the π* molecular orbital of CO_2, as seen in Figure 4.2 (c), occurs during

physisorption, resulting in a reduction of bond order evident by a bending of the O-C-O angle from 180° to 177.6°. From Löwdin [83] analysis, this charge donation increases in the chemisorbed configurations (Figure 4.2 (d) and (e)) to 0.523 e and 0.757 e, respectively. It is also worth noting that while electron density from the defect state is donated to CO_2 that is bound to two B atoms, a portion is also shared among the remaining B atoms (Figure 4.2 (d)). This is important for the adsorption and dissociation of H_2.

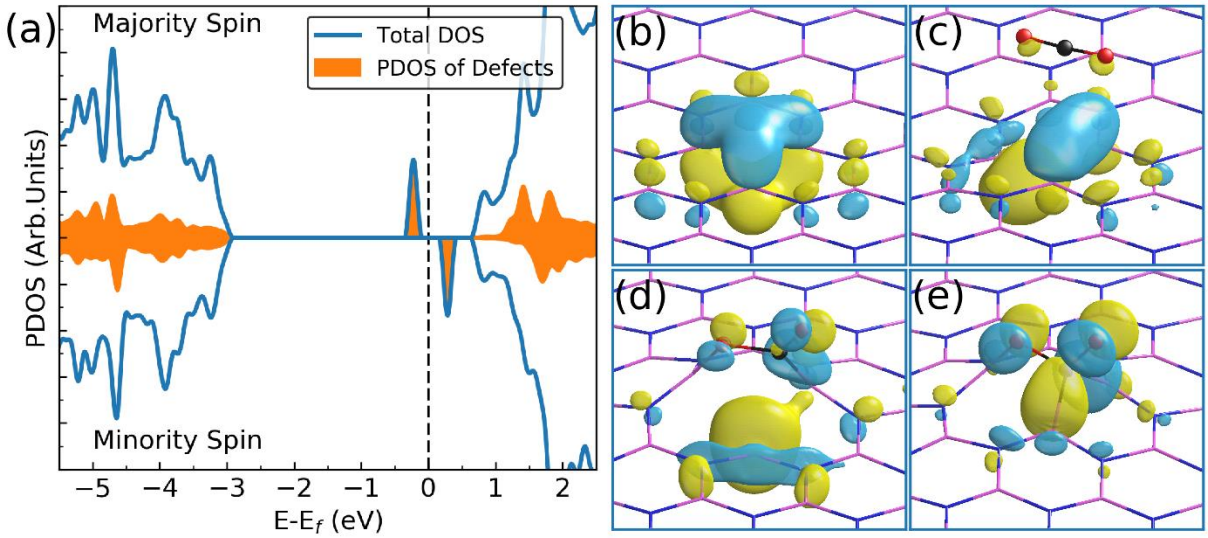

Figure 4.2 (a) Density of states (DOS) of *h*-BN with N vacancy and its projection onto atoms near the defect; (b) wave function of the occupied defect state, below the Fermi level E_f, and its evolution upon adsorption of CO_2: (c) at physisorbed state $CO_{2(p)}$, and chemisorbed state (d) CO_2*(I) and (e) CO_2*(II). Isosurface value is 0.015 e/Å. For visualization of the orbitals, sizes of the atoms are reduced.

4.3.3 CO_2 and H_2 co-adsorption

We find that H_2 adsorbs dissociatively on a nitrogen vacancy in *dh*-BN with a barrier of 61.94 kJ/mol (0.64 eV), and an adsorption energy of -172.66 kJ/mol (-1.79 eV), in agreement with values reported in Ref. [14]. More importantly, we find that to facilitate hydrogenation of

CO_2, co-adsorption must occur. In the configuration referred as CoAds(I) in Figure 4.3, two atomic H sit on a single boron atom and CO_2* takes the CO2*(I) configuration at the vacancy site with a co-adsorption energy of -190.59 kJ/mol(-1.98 eV). To form the co-adsorption configuration CoAds(I), H_2 must overcome a barrier of 39.67 kJ/mol (0.41 eV). It is important to note that this barrier is significantly lower than that of 61.94 kJ/mol (0.64 eV) for dissociative adsorption of H_2 on an unoccupied defect site. The excess electron density contributed by the frontier orbital on the B site (Figure 4.2 (d)) facilitates this process. Should H_2 come first, the barrier for CO_2 adsorption is found to be 78.32 kJ/mol(0.81 eV) (See Figure 4.4 for details of the pathway of this co-adsorption). We also found that the CoAds(II) is not energetically and kinetically favorable as compared to CoAds(I).

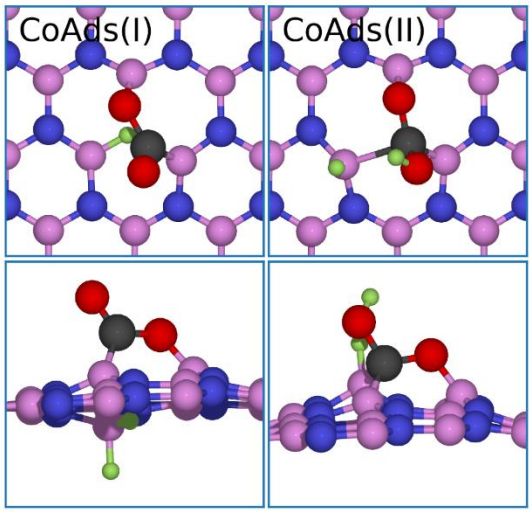

Figure 4.3 Top (upper panel) and side (lower panel) view of the co-adsorption configuration CoAds(I) (left) and CoAds(II) (right) of CO_2 and dissociated H_2. Blue, pink, black, red, and green balls represent N, B, C, O, and H atoms, respectively.

Figure 4.4 shows the reaction pathway for forming CoAds(I) configuration (Figure 4.3) and atomistic models of each intermediate states involved in reaction pathways. Should H_2

comes to the defect first, the highest barrier it has to come is 61.94 kJ/mol (0.64 eV) (to form H1 state, reaction 010 in Table 4.3). It then performs structural arrangement with minimal activation barrier (H1→H2, reaction 011 in Table 4.4) to form the lowest energy configuration (H2). The next step is the adsorption of CO_2 with a barrier of 78.32 kJ/mol (0.81 eV), reaction 012 in Table 4.4, to form H3 configuration. The adsorbed CO_2* will then rearrange itself to go through H4, H5, H6, and H7 configurations via the low barrier reactions 013, 014, 015, and 016, respectively, as shown in Table 4.4 and Table 4.5. Should the CO_2 adsorb first, the reaction pathway is much simpler, involving two reactions 001 and 003 (Table 4.2) with barriers of 14.12 and 40.82 kJ/mol, respectively, to form C1 and C2 (H7) configurations, respectively. The first reaction is the adsorption of CO_2, and the second one is the adsorption of H_2.

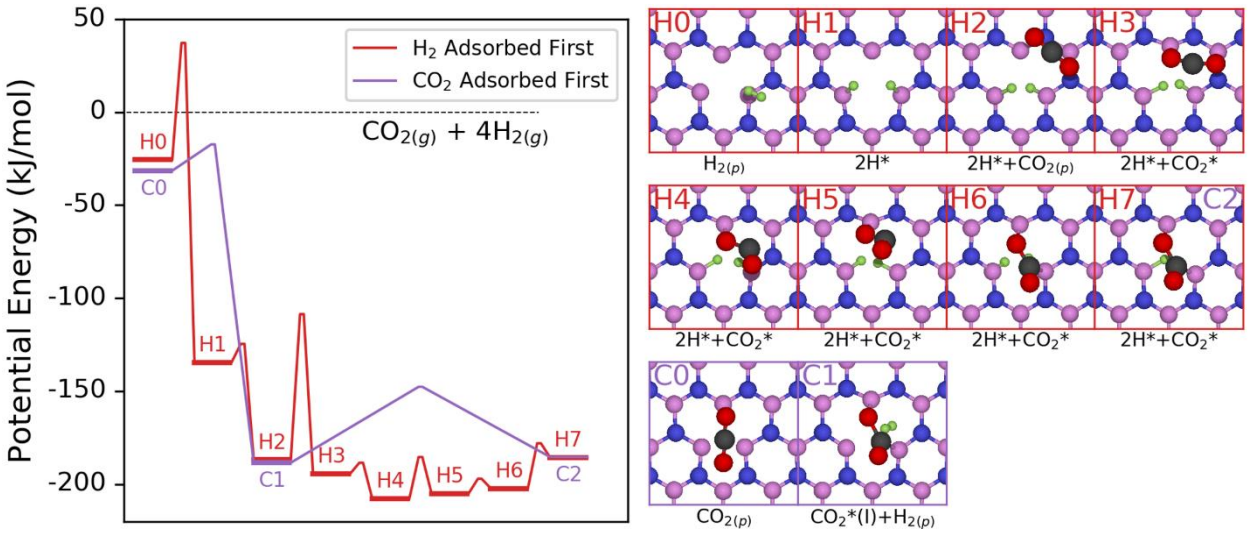

Figure 4.4 (Left) Reaction pathways of the formation of co-adsorption configuration CoAds(I). Horizontal bars represent intermediate states of the two pathways. Potential energy of each state is calculated with respect to one CO_2 and 4 H_2 molecules in gas phase. (Right) Atomistic configurations of the states noted in the left panel. Blue, pink, black, red, and green balls represent N, B, C, O, and H atoms, respectively.

The competitiveness of the binding strength of CO_2 and dissociative H_2 molecules makes co-adsorption of the two species preferable than the adsorption of one species until saturation. For instant, binding energy of the first dissociative H_2 adsorption at the vacancy is found to be -172.66 kJ/mol (-1.79 eV) but becomes 64.18 kJ/mol (0.67 eV) for the binding of the second molecule, an endothermic adsorption. Similarly, the binding energy of the first CO_2 molecule is CO_2*(I) configuration is -189.83 kJ/mol (-1.97 eV) while that of the second molecule is reduced to -66.16 kJ/mol (-0.69 eV). These values suggest that in catalytic reaction condition, the second molecule (H_2 or CO_2) would prefer to desorb from the defect leaving available site for co-adsorption of CO_2 and H_2 paving the way for the hydrogenation process.

In the second co-adsorption configuration (Figure 4.3), CoAds(II), one atomic H bonds to an O atom and the other bonds the to a B atom. This configuration is possible as the O atom that does not bond to any B atom is unsaturated. The co-adsorption energy for this configuration is found to be -141.04 kJ/mol (-1.46 eV). To form the co-adsorption configurations, CO_2 must adsorb first. We found that the barrier for H_2 dissociatively adsorption is 126.17 kJ/mol (1.31 eV), reaction 035 in Table 4.8. Given significantly lower in co-adsorption energy and higher in reaction barrier, CoAds(II) is not energetically and kinetically favorable as compared to CoAds(I).

4.3.4 Hydrogenation Pathway

From the CoAds(I) configuration, the first atomic H react with C to form HCOO*, with a barrier of 17.03 kJ/mol (0.18 eV). It is not favorable for the remaining H atom to react with the resultant HCOO* species. The reaction (HCOO* + H* → HCOOH*) is highly endothermic

(146.96 kJ/mol, 1.52 eV). To complete hydrogenation of the surface HCOO* species, additional gas phase H_2 molecule is needed. Even though the vacancy site is occupied, the dissociation of H_2 can be facilitated by the large negative charge of the outward-pointing O. Figure 4.5 shows the reconfiguration of the defect state during the reaction with gas phase H_2 molecule. At the onset, the charge of the defect state is transferred to HCOO* species, giving the outward O atom a negative charge (-0.325 e). The charge then transfers to H_2 molecule, facilitating the dissociation. One atomic H reacts with HCOO* to form HCOOH* and the other atomic H recombines with the *dh*-BN surface. The barrier for this process is 85.12 kJ/mol (0.88 eV). We found that desorption of the HCOOH* species is not favorable due to its high endothermicity (203.26 kJ/mol, 2.11 eV, reactions 029 and 030 in Table 4.7, and 031 in Table 4.8). We also found that the –OH group in the resultant HCOOH* species rotates by about 114°, with a barrier of 13.10 kJ/mol (0.14 eV), for facilitating the subsequent reactions.

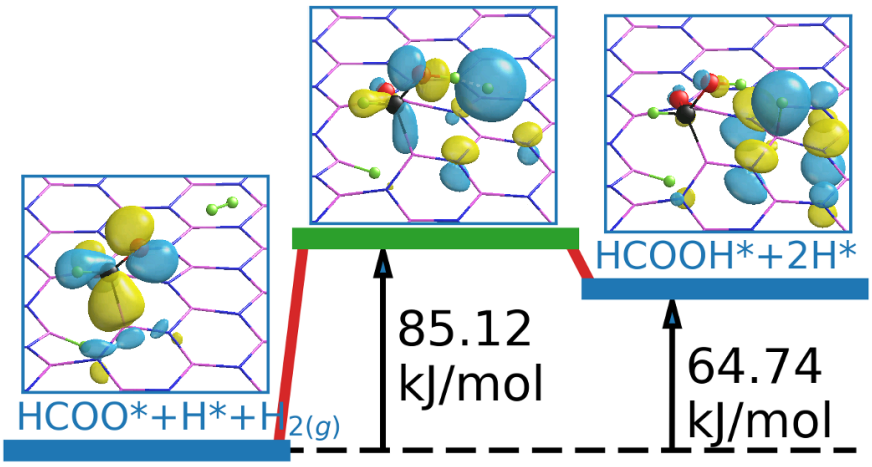

Figure 4.5 Evolution of the defect (frontier) orbitals during the dissociation of an H_2 molecule on *h*-BN with N vacancy that is occupied by HCOO* and H* species. Blue horizontal bars represent the initial and final states and green horizontal bar represent transition state of HCOO* + H* + $H_{2(p)}$ →HCOOH* + 2H* reaction. Blue, pink, black, red, and green balls represent N, B, C, O, and H atoms, respectively.

Figure 4.6 shows the reaction pathway for the formation of HCOOH*. From C2/H7 configuration (Figure 4.4), referred as F5, the H* at B site towards to bottom first jump to the B site with H* towards to the up (F6) (reaction 004 in Table 4.2) with a barrier of 64.01 kJ/mol. The next step is the formation of HCOO* with a barrier of 17.03 kJ/mol (reaction 005 Table 4.2, F6→F7). The reaction pathway is followed by the addition of H_2 as described in the main text (reaction 008 in Table 4.3, F7→F8). The final step of this path is the rotation of -OH group, with a small barrier of 13.10 kJ/mol (reaction 009 in Table 4.3, F8→F9).

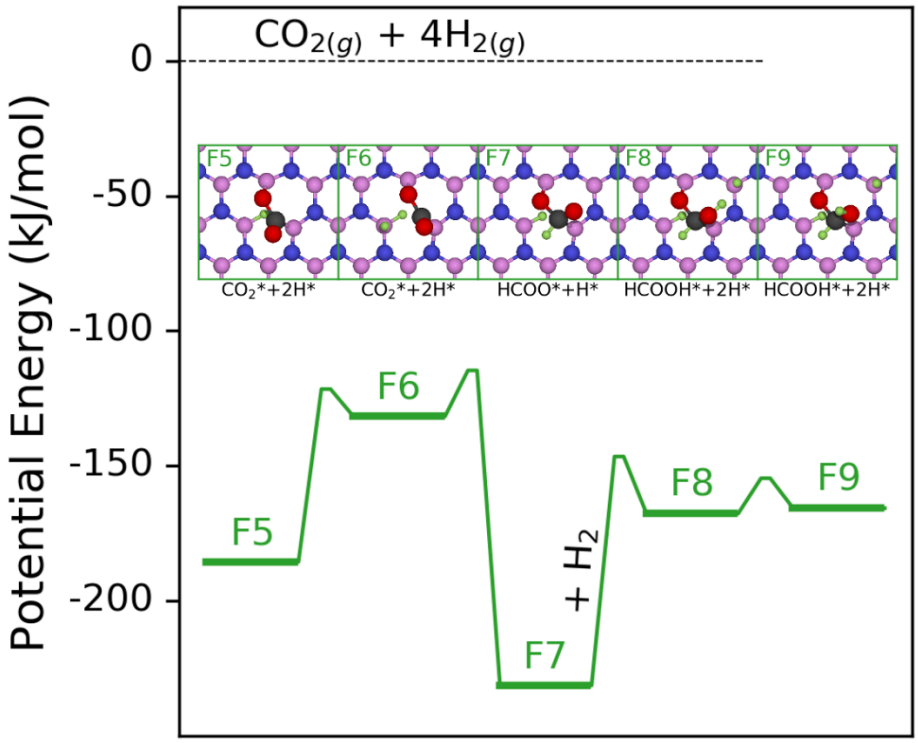

Figure 4.6 Reaction pathways for the formation of HCOOH*. Horizontal bars represent intermediate states of the two pathways. Potential energy of each state is calculated with respect to one CO_2 and 4 H_2 molecules in gas phase. Inserts are atomistic configurations of the states noted in the left panel. Blue, pink, black, red, and green balls represent N, B, C, O, and H atoms, respectively. F5 state is the same as C2/H7 state in Figure 4.4.

4.3.5 Alternative Pathway for HCOO* + H_2

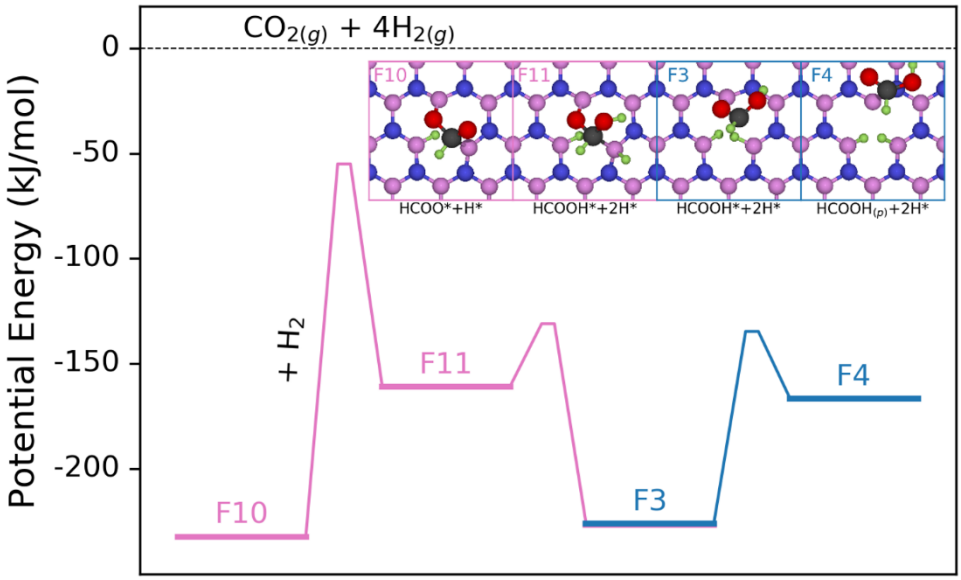

Figure 4.7 Alternative reaction pathways of HCOO* + H_2. Horizontal bars represent intermediate states of the two pathways. Potential energy of each state is calculated with respect to one CO_2 and 4 H_2 molecules in gas phase. Inserts are atomistic configurations of the states noted in the left panel. Blue, pink, black, red, and green balls represent N, B, C, O, and H atoms, respectively.

Figure 4.7 shows an alternative less-favorable pathway for the addition of H_2 to HCOO* + H* state. In this case, H_2 dissociates in a way that one H* is bonded to HCOO* the other is bonded to B atom when HCOO* bonded to (reaction 007 in Table 4.3). This reaction has a barrier of 177.31 kJ/mol, which is higher than that of the competitive process discussed in the last section, suggesting that this alternative pathway is less favorable.

4.3.6 Desorption of Formic Acid

Starting with the HCOOH* + 2H* configuration, we summarize (Figure 4.8) the reaction pathways for the formation of: 1) formic acid (F0→F4, reactions 024→026 and 028, which shown in Table 4.6 and Table 4.7); 2) methanol (M0→M7, reactions 017→023, which shown in

Table 4.5 and Table 4.6. Its alternative path is M'0→M'6→M7, reactions 036→041 and 020→023 in Table 4.5-4.10). To form formic acid, H* on the *dh*-BN surface diffuses to the next N site (state F1) with a barrier of 81.65 kJ/mol (0.85 eV) and then to the B site at the vacancy (F2) with a barrier of 32.86 kJ/mol (0.34 eV), at which point the B-C bond is broken (F3) leaving only one bond between HCOOH* and *h*-BN (B-O bond). This process is exothermic (-61.23 kJ/mol, -0.63 eV) with a barrier of 34.46 kJ/mol (0.36 eV). Finally, the resultant formic acid will desorb with a barrier of 91.54 kJ/mol (0.95 eV) (F4).

4.3.7 Formation of Methanol

Alternatively, the reaction can take a different path from the same starting point (aka state F0/M0). In this path, H* on the *dh*-BN surface combines with –OH group to form H_2O with a barrier of 62.80 kJ/mol (0.65 eV), which is slightly higher than that of H diffusion process, leaving HCO* species at the vacancy. The reaction (M0→M1) is highly exothermic (-152.25 kJ/mol, -1.58 eV). The HCO* will then react with gas phase H_2 to form CH_2O* and 2 absorbed atomic H* (M2). This process happens with a mechanism similar to that for HCOO* + H2 which has been previously discussed (Figure 4.5). The H* is now bound to B at the vacancy and the charge at the C atom facilitates the reaction. This process has a barrier of 91.11 kJ/mol (0.94 eV) and is endothermic (75.71 kJ/mol, 0.78 eV). The resulting moiety CH2O* transforms to a lower potential state M3, in which only O is bonded to the *h*-BN, with a barrier of 46.45 kJ/mol (0.48 eV).

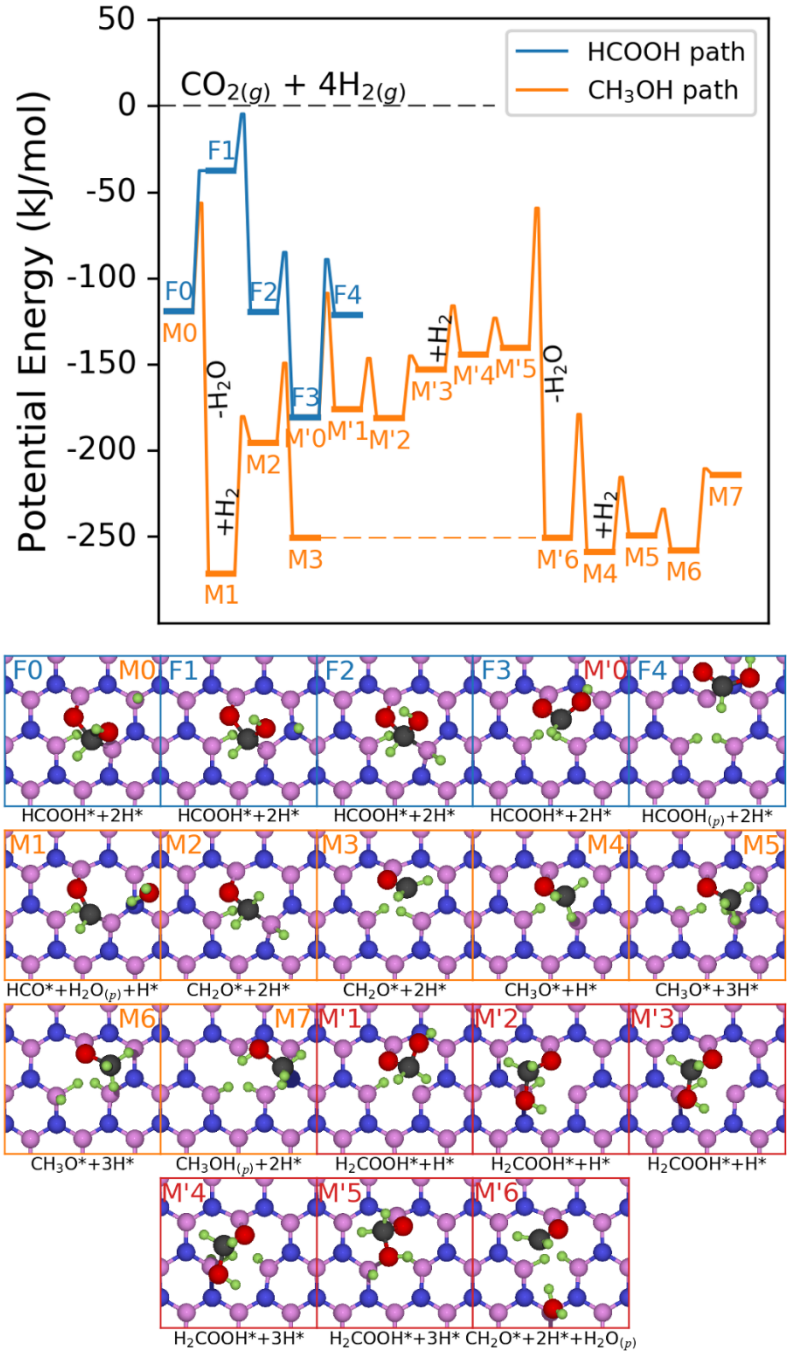

Figure 4.8 (Top) Reaction pathways for formic acid and methanol formation. Horizontal bars represent intermediate states in the two pathways. Potential energy of each state is calculated with respect to one CO_2 and 4 H_2 molecules in gas phase. (Bottom) Atomistic configurations of the states noted in the left panel. Blue, pink, black, red, and green balls represent N, B, C, O, and H atoms, respectively.

The adsorbed CH_2O* then converts to methoxy by reacting with an H* (state M4), with an activation barrier of 71.83 kJ/mol (0.74 eV), leaving one B near the vacancy site that is not occupied by any adsorbate on which H_2 can dissociatively adsorb (to form state M5). This dissociation has a barrier of 44.04 kJ/mol (0.46 eV). Eventually, two -BH_2 groups rearrange, with a barrier of 15.52 kJ/mol (0.16 eV), to a lower energy configuration (M6) from which methanol is formed and desorbed from the defect (M7) with a barrier of 47.35 kJ/mol (0.49 eV), leaving two H* at the defect site. This desorption of methanol is endothermic (43.53 kJ/mol, 0.45 eV). Subsequent CO_2 molecules could adsorb at the vacancy preoccupied by two H* to form CoAds(I) as discussed earlier and the reaction is repeated.

Before desorption of formic acid (F3→F4), the reaction HCOOH* + H*→H_2COOH* (M'0→M'1) could happen with an effective activation barrier of 71.93 kJ/mol (0.75 eV), which is lower than that of the desorption process, following by the low barrier reconfigurations (M'1 →M'2 and M'2→M'3), starting the pathway for the formation of methanol. As a result of this reaction, an empty B site is exposed and is available for the dissociative adsorption of an H_2 molecule (M'3→M'4). This mechanism is similar to the dissociative adsorption that forms CoAds(I), as previously discussed. This dissociative adsorption is slightly endothermic (8.81 kJ/mol, 0.09 eV) with a barrier of 37.00 kJ/mol (0.38 eV). After a small barrier reconfiguration process, M'4→M'5, the ‒OH group of H_2COOH* then combines with H* to form H_2O (M'5→ M'6, H_2COOH* + H* → H_2CO* + $H_2O_{(p)}$) with an activation barrier of 81.00 kJ/mol (0.84 eV). This particular reaction is highly exothermic (-110.54 kJ/mol, -1.15 eV). From M'6, the reactions

continue to form methanol (M3→M7) as described above because the adsorbed species in M'6 and M3 states are identical.

At the end of both formic acid and methanol formation, the defect is occupied by two atomic H*. Subsequent CO_2 molecules could adsorb at the vacancy to from CoAds(I) as discussed earlier and the reaction cycle is repeated.

Even though our calculations indicate few reaction steps with sizable barriers, reactions with activation energies between 95 (0.99) and 134 (1.40) kJ/mol (eV) have been driven mechanochemically [104-108]. Our computed maximum barrier is not outside of this range, suggesting that our proposed mechanism is feasible.

4.3.8 Formic Acid / Methanol selection

We note that along the reaction pathways, it is the F0 and F3 state that determine the selection of formic acid or methanol as the final product. From both states, the paths that lead to the formation of formic acid begin with endothermic processes (F0→F1 and F3→F4) with barriers that are higher than that for the starting processes of methanol formation (F0/M0→M1 and F0/M'0→M'1), which are highly exothermic. Thus, methanol formation is thermodynamically preferable and is the preferred product. However, to further progress to the M7 state, methanol formation requires addition of two H_2 molecule from gas phase, all of which are endothermic processes (M1→M2, M'3→M'4, and M4→M5). Such processes are less likely to happen at high temperature at which desorption of H_2 is facilitated or through the application

of mechanical force. Thus, at high temperatures, the formation and desorption of formic acid (F0 →F4) is favorable.

4.3.9 Total Reaction Pathway

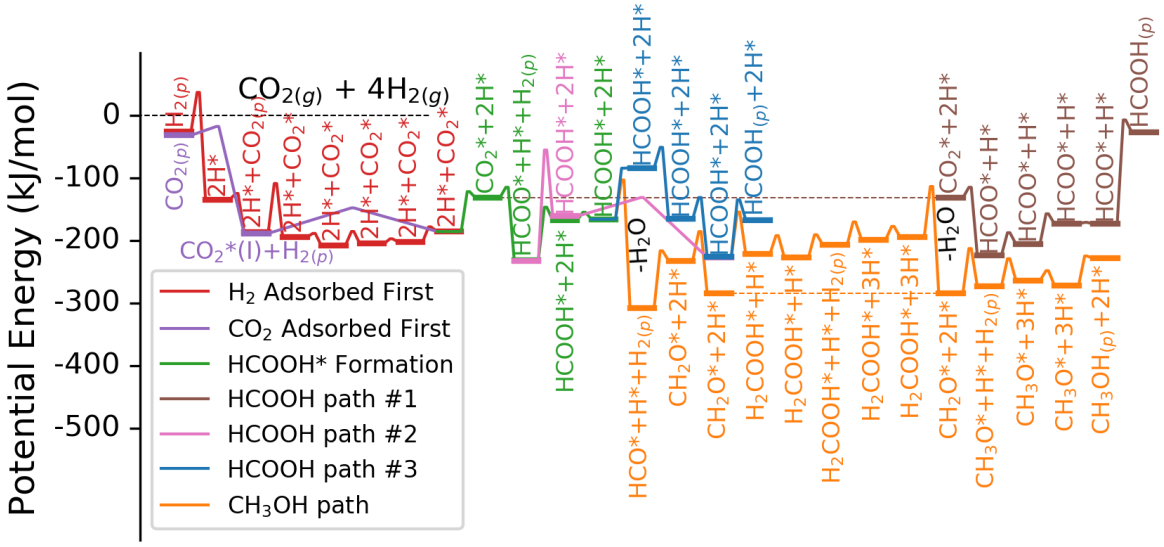

Figure 4.9 Total reaction pathway of the CO_2 reduction on dh-BN with nitrogen vacancy. Potential energy of each state is calculated with respect to one CO_2 and 4 H_2 molecules in gas phase. To calculate potential energy of each state, additional H_2 or CO_2 molecules in gas phase are added to each state if needed.

Figure 4.9 shows the total reaction pathway calculated with DFT. Each section of the pathway is discussed individually in the main text of in this supplementary material.

"H_2 Adsorbed First" pathway is the formation of co-Adsorption CoAds(I) staring with a dissociative adsorption of H_2. This pathway consists of reactions 010, 011, 012, 013, 014, 015, and 016 (Table 4.3-4.5).

"CO_2 Adsorbed First" pathway is the formation of co-Adsorption CoAds(I) starting with the adsorption of CO_2. This pathway consists of two reactions 001 and 003 (Table 4.2).

"HCOOH* Formation" pathway is the formation of HCOOH* species from CoAds(I) configuration. This pathway consists of reactions 004, 005, 008, and 009 (Table 4.2 and 4.3)

"HCOOH path #1" is the formation of formic acid directly from CO_2* and 2 atomic H*. This pathway consists of reactions 005, 032, 033, 034, and 006 (Table 4.2 and 4.8)

"HCOOH path #2" is the formation of formic acid from HCOO* and an additional dissociative H_2 molecules. This pathway consists of reactions 007, 027, 026, and 028 (Table 4.3 and 4.7)

"HCOOH path #3" is the formation of formic acid from HCOOH* species. This pathway consists of reactions 024, 025, 026, and 028 (Table 4.6 and 4.7).

"CH_3OH path" is the formation of methanol from HCOOH* species. This pathway consists of reactions 017, 018, 019, 020, 021, 022, 023, 036, 037, 038, 039, 040, and 041 (Table 4.5, 4.6, 4.9 and 4.10).

"HCOOH path #3" and "CH_3OH path" are plotted in Figure 4.8.

4.4 Conclusion

Engineering catalytic activity into a solid through the introduction of defects is an important step toward realizing rationally designed heterogeneous catalysts. Through exploitation of defects a heterogeneous catalyst for the reduction of CO_2 to methanol was realized. It also provides a general criterion for active sites for CO_2 reduction catalyst: strong co-adsorption of CO_2 and H_2 on the sites that is more favorable than the adsorption of individual species. Defects in *h*-BN are extremely active toward the formation of low volatility compounds.

Increased reaction temperatures or implementation in a plug flow reactor may alleviate this issue. Also, the production of formic acid and methanol are attractive for time shifting electrical energy generation from solar and wind sources. This would be achieved through the conversion of excess electrical energy to chemical energy, during peak production times, and conversion back to electrical energy, during peak demand times. Both are useful, liquid fuels that can be used to power small turbines for energy generation at peak demand and the subsequent CO_2 combustion product can be again captured and reused. With an active site concentration of 1%, 4700 m^3 would be sufficient to capture and utilize the world's yearly production of carbon dioxide. This would translate to a little over 200 catalyst beds less than the size of a small shed. Assuming production from borax, this amount would consume less than 1% of the world's yearly boron production - once [109]. Catalysts such as *dh*-BN can provide a pathway toward reduction of global CO_2 release by commoditizing CO_2 thereby encourage utilization versus disposal.

Table 4.2 List of all reactions used in this work (part 1). Blue, pink, black, red, and green balls represent N, B, C, O, and H atoms, respectively

Reaction ID	Initial state	Final state	Barrier (kJ/mol)	Reaction energy (kJ/mol)
001	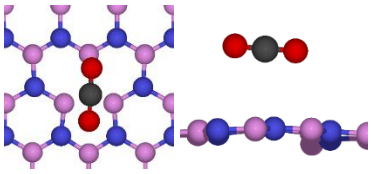 $CO_{2(p)}$	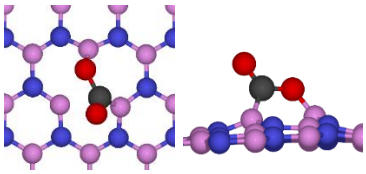 CO_2*(I)	14.12	-150.02
002	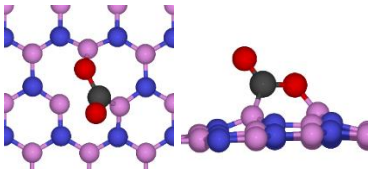 CO_2*(I)	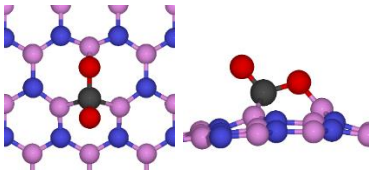 CO_2*(II)	15.27	-8.61
003	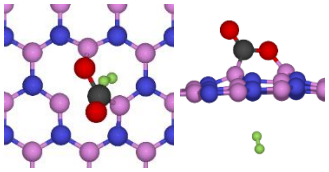 CO_2*(I)+$H_{2(p)}$	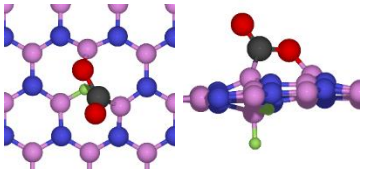 CO_2*+2H*	40.82	3.09
004	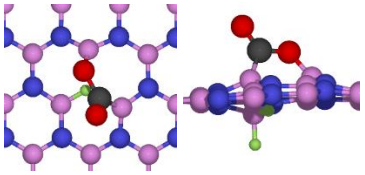 CO_2*+2H*	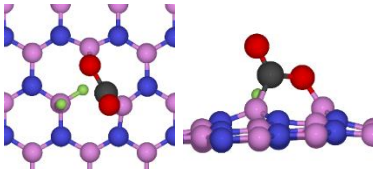 CO_2*+2H*	64.01	53.91
005	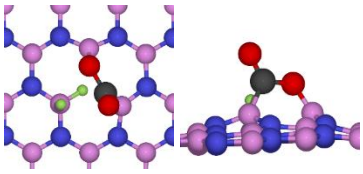 CO_2*+2H*	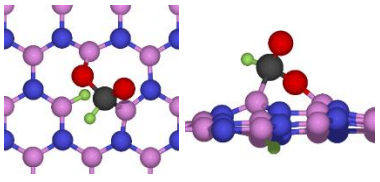 HCOO*+H*	17.03	-91.99

Table 4.3 List of all reactions used in this work (part 2). Blue, pink, black, red, and green balls represent N, B, C, O, and H atoms, respectively

Reaction ID	Initial state	Final state	Barrier (kJ/mol)	Reaction energy (kJ/mol)
006	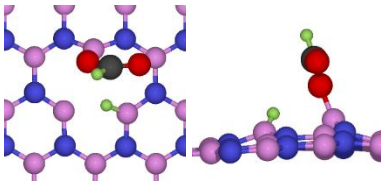 HCOO* + H*	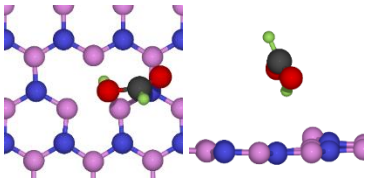 $HCOOH_{(p)}$	166.28	146.96
007	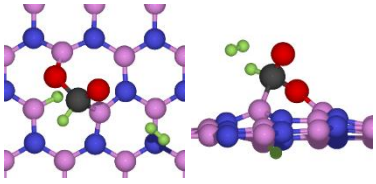 HCOO* +H* +$H_{2(p)}$	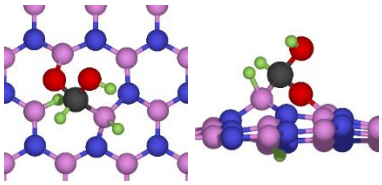 HCOOH*+2H*	177.31	70.61
008	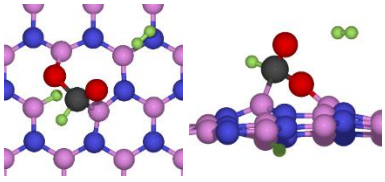 HCOO*+H*+$H_{2(p)}$	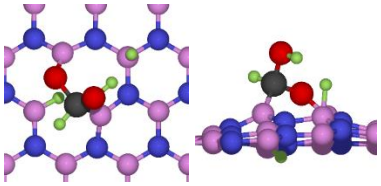 HCOOH*+2H*	85.12	64.74
009	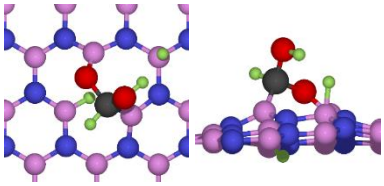 HCOOH*+2H*	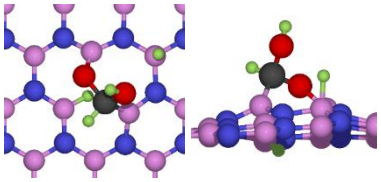 HCOOH*+2H*	13.10	2.01
010	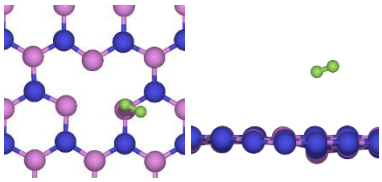 $H_{2(p)}$	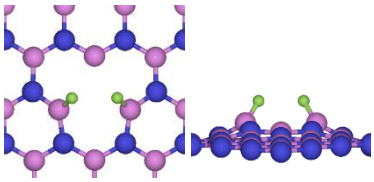 2H*	62.85	-108.63

Table 4.4 List of all reactions used in this work (part 3). Blue, pink, black, red, and green balls represent N, B, C, O, and H atoms, respectively

Reaction ID	Initial state	Final state	Barrier (kJ/mol)	Reaction energy (kJ/mol)
011	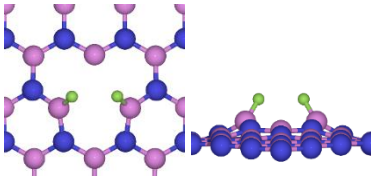 2H*	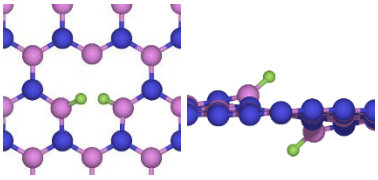 2H*	9.98	-38.13
012	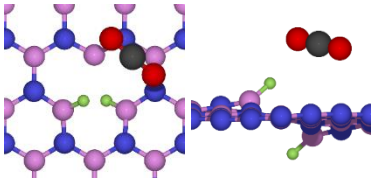 2H* +$CO_{2(p)}$	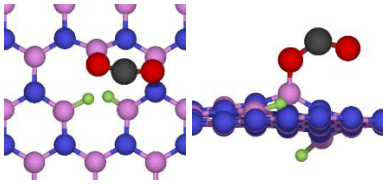 2H*+CO_2*	78.32	-7.55
013	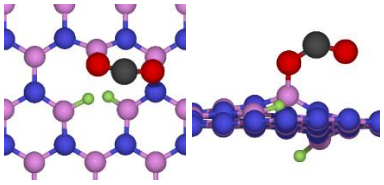 2H*+CO_2*	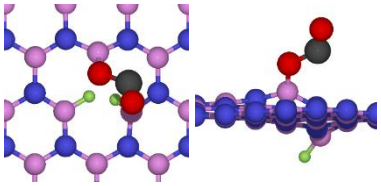 2H*+CO_2*	5.95	-13.39
014	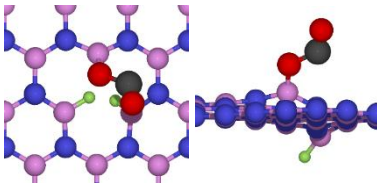 2H*+CO_2*	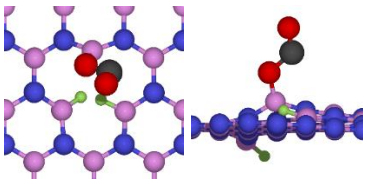 2H*+CO_2*	22.44	2.85
015	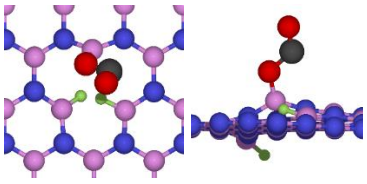 2H*+CO_2*	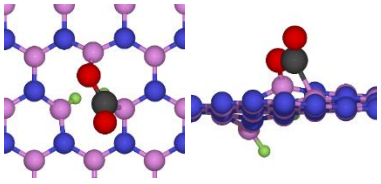 2H*+CO_2*	7.87	3.02

Table 4.5 List of all reactions used in this work (part 4). Blue, pink, black, red, and green balls represent N, B, C, O, and H atoms, respectively

Reaction ID	Initial state	Final state	Barrier (kJ/mol)	Reaction energy (kJ/mol)
016	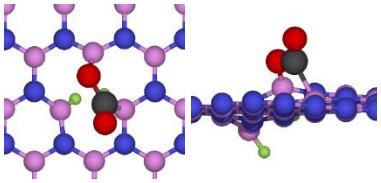 $2H^*+CO_2^*$	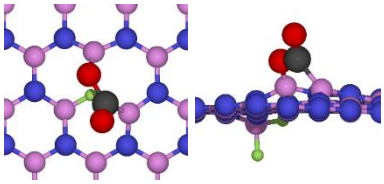 $2H^*+CO_2^*$	24.27	16.61
017	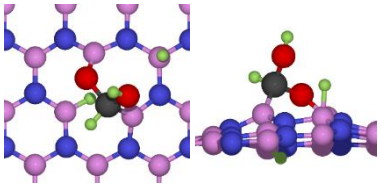 $HCOOH^*+2H^*$	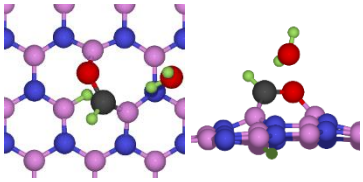 $HCO^*+H_2O_{(p)}+H^*$	62.80	-152.25
018	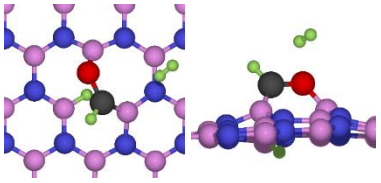 $HCO^*+H^*+H_{2(p)}$	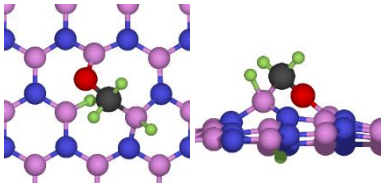 $CH_2O^*+2H^*$	91.41	75.71
019	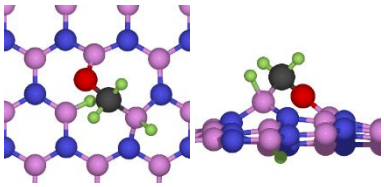 $CH_2O^*+2H^*$	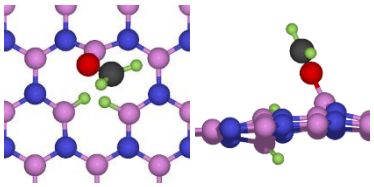 $CH_2O^*+2H^*$	46.45	-52.68
020	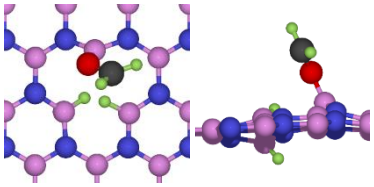 $CH_2O^*+2H^*$	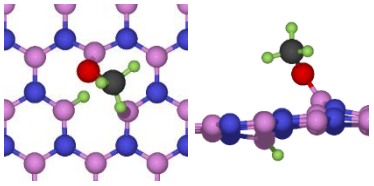 $CH_3O^*+H^*$	71.83	-8.11

Table 4.6 List of all reactions used in this work (part 5). Blue, pink, black, red, and green balls represent N, B, C, O, and H atoms, respectively

Reaction ID	Initial state	Final state	Barrier (kJ/mol)	Reaction energy (kJ/mol)
021	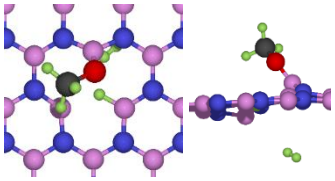 $CH_3O^*+H^*+ H_{2(p)}$	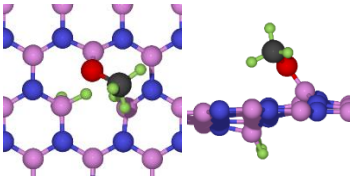 $CH_3O^*+3H^*$	44.04	10.36
022	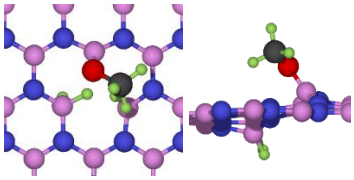 $CH_3O^*+3H^*$	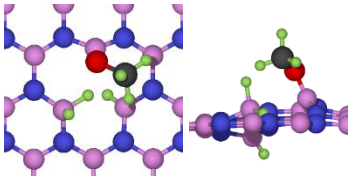 $CH_3O^*+3H^*$	15.52	-8.37
023	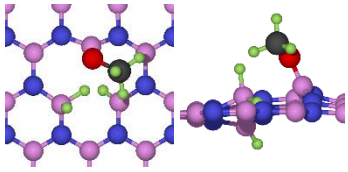 $CH_3O^*+3H^*$	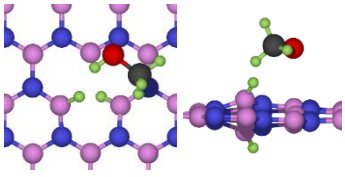 $CH_3OH_{(p)}+2H^*$	47.35	43.53
024	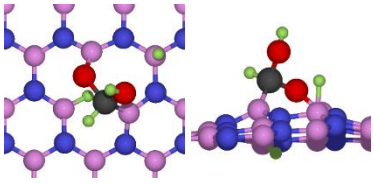 HCOOH*+2H*	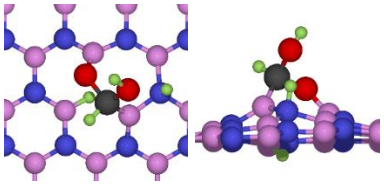 HCOOH*+2H*	81.65	81.65
025	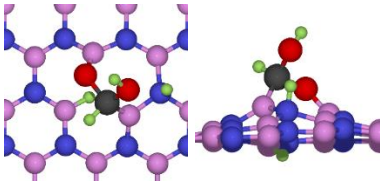 HCOOH*+2H*	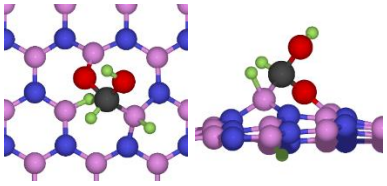 HCOOH*+2H*	32.86	-81.90

Table 4.7 List of all reactions used in this work (part 6). Blue, pink, black, red, and green balls represent N, B, C, O, and H atoms, respectively

Reaction ID	Initial state	Final state	Barrier (kJ/mol)	Reaction energy (kJ/mol)
026	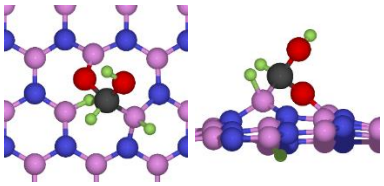 HCOOH*+2H*	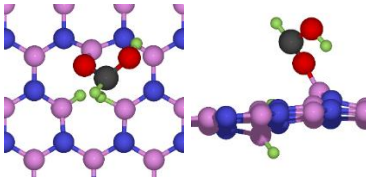 HCOOH*+2H*	34.46	-61.23
027	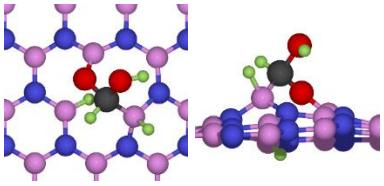 HCOOH*+2H*	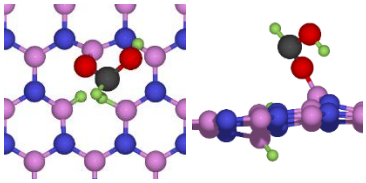 HCOOH*+2H*	30.07	-65.59
028	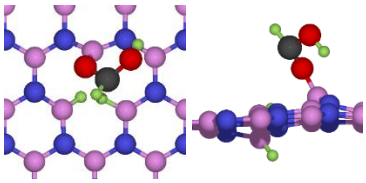 HCOOH*+2H*	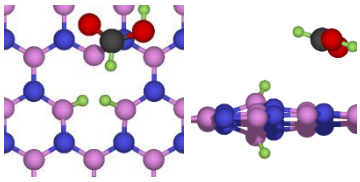 $HCOOH_{(p)}$+2H*	91.54	59.43
029	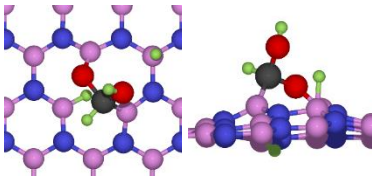 HCOOH*+2H*	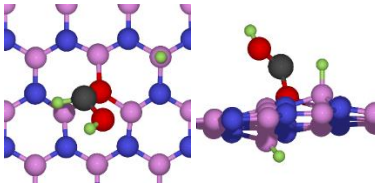 HCOOH*+2H*	78.93	76.42
030	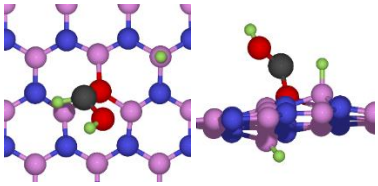 HCOOH*+2H*	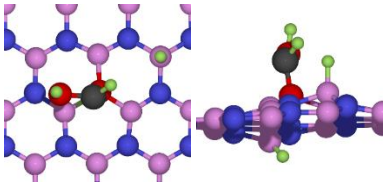 HCOOH*+2H*	1.48	-2.02

Table 4.8 List of all reactions used in this work (part 7). Blue, pink, black, red, and green balls represent N, B, C, O, and H atoms, respectively

Reaction ID	Initial state	Final state	Barrier (kJ/mol)	Reaction energy (kJ/mol)
031	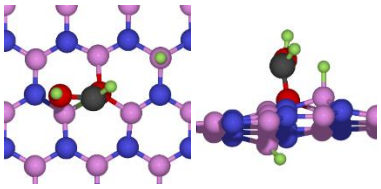 HCOOH*+2H*	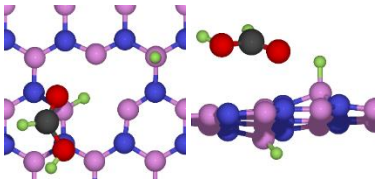 $HCOOH_{(p)}$+2H*	131.25	128.86
032	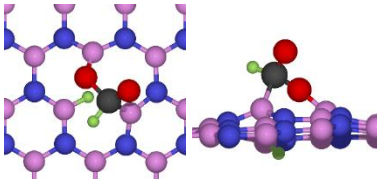 HCOO*+H*	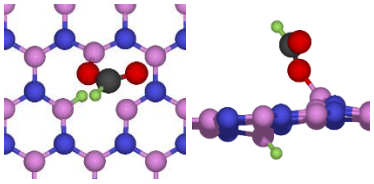 HCOO*+H*	36.36	18.43
033	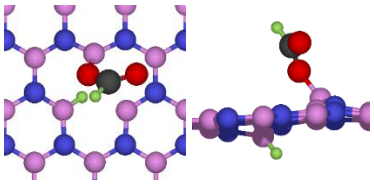 HCOO*+H*	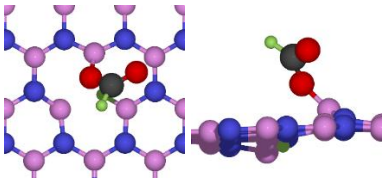 HCOO*+H*	48.15	32.01
034	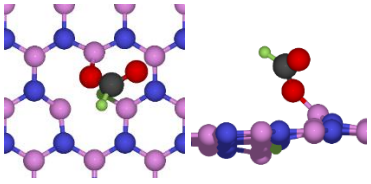 HCOO*+H*	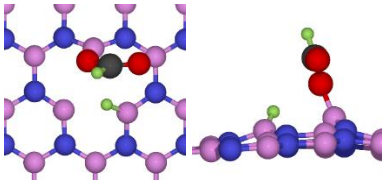 HCOO*+H*	2.43	-0.33
035	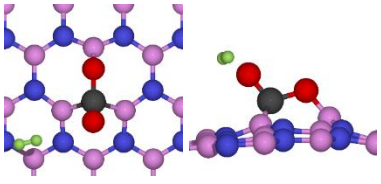 CO_2*(I)+$H_{2(p)}$	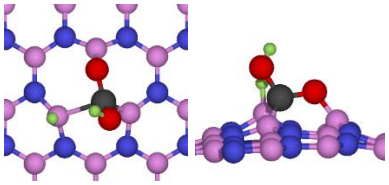 COOH*+H*	126.17	55.33

Table 4.9 List of all reactions used in this work (part 8). Blue, pink, black, red, and green balls represent N, B, C, O, and H atoms, respectively

Reaction ID	Initial state	Final state	Barrier (kJ/mol)	Reaction energy (kJ/mol)
036	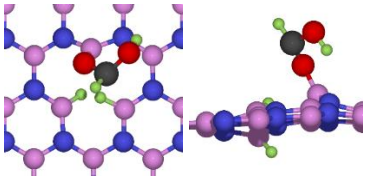 HCOOH*+2H*	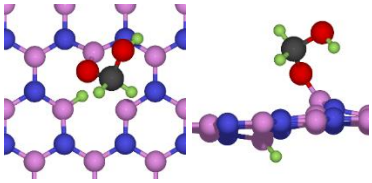 $H_2COOH^*+H^*$	71.93	4.61
037	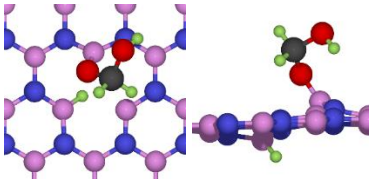 $H_2COOH^*+H^*$	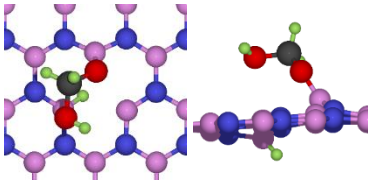 $H_2COOH^*+H^*$	29.51	-5.34
038	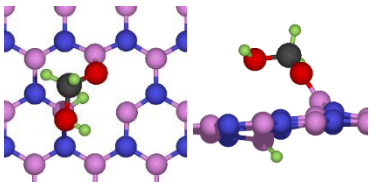 $H_2COOH^*+H^*$	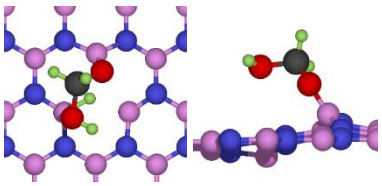 $H_2COOH^*+H^*$	36.31	28.35
039	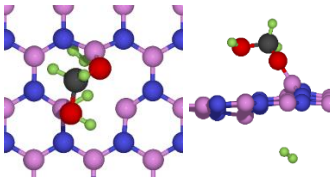 $H_2COOH^*+H^*+H_{2(p)}$	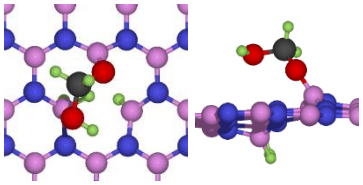 $H_2COOH^*+3H^*$	37.00	8.81
040	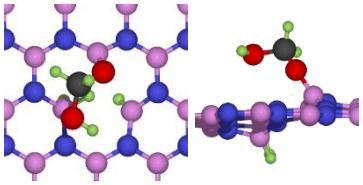 $H_2COOH^*+3H^*$	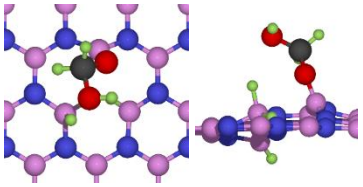 $H_2COOH^*+3H^*$	21.04	3.90

Table 4.10 List of all reactions used in this work (part 9). Blue, pink, black, red, and green balls represent N, B, C, O, and H atoms, respectively

Reaction ID	Initial state	Final state	Barrier (kJ/mol)	Reaction energy (kJ/mol)
041	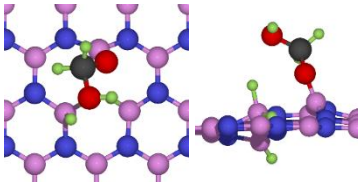 $H_2COOH^*+3H^*$	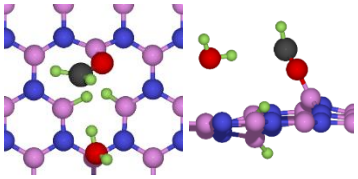 $CH_2O^*+2H^*+ H_2O_{(p)}$	81.00	-110.54

CHAPTER 5: TOWARDS HIGHER ALCOHOL FORMATION USING A SINGLE-LAYER MoS_2 ACTIVATED Au NANOPARTICLE

We demonstrate that the 13-atom gold nanoparticles on single-layer MoS_2 (Au_{13}/MoS_2) is catalytically active for acetaldehyde (CH_3CHO) synthesis, from carbon monoxide (CO) and methanol (CH_3OH) via the density functional theory (DFT) modeling. The reactant CO plays an important role in promoting dissociation of methanol and formation of acetyl (via C-C coupling via between CO and methyl). We find CH_3CO hydrogenation to form CH_3COH is less energetic favorable than to form CH_3CHO. The carbonylation of methanol to a C_2 species represents a crucial step toward the formation of higher alcohols.

5.1 Introduction

The formation of higher alcohols from syngas is an important goal in the quest for economic and sustainable transformation of biomass into transportation fuels [110]. A necessary step for its realization is efficient C-C coupling involving oxygenate small molecules such as carbon monoxide and methanol [111]. The seminal finding by Haruta of CO oxidation by supported nanoscale gold particles [112] showed that gold, despite being arguably the most noble of metals [113], can play an active role in heterogeneous catalysis. In recent work [23, 72, 114], we have shown that single-layer MoS_2 coating can transform an otherwise inert substrate, silica, into a catalytic active surface for e.g. CO oxidation by gold nanoclusters, similar to results obtained for reducible oxides, such as titania and ceria [115-121]. Concomitant computational efforts have predicted a number of feasible, low-barrier reaction [122] on pathways on thus supported gold nanoparticles [27, 72] in contrast to the largely catalytically inactive bulk gold,

Au on pristine silica or on other 2D materials like graphene [123-125]. Here, we address the carbonylation of methanol as the most fundamental C-C coupling step that can lead to higher alcohol formation, from a lower alcohol and a component of syngas, as it may be obtained from biomass gasification.

A wide range of catalytic applications have been proposed for MoS_2, both in the past and more recently. MoS_2 with cobalt and alkali modifiers is the key catalyst material in industrial hydrodesulfurization; notably, the industrial catalyst material resembles a few-layer film [126]. MoS_2 modified by alkali has also been proposed for alcohol formation [127-135]. The mechanistic aspects of these studies by and large focus on the hydrogenation step, in particular the initial CO hydrogenation. In contrast, our study focusses on the extension of the carbon chain toward higher alcohols by means of carbonylation of methanol.

MoS_2 has gained prominence as a catalyst for hydrogen evolution [136, 137]; its activity has been attributed to edge sites based on low-temperature measurements [138], and related materials that feature large number of exposed edge sites have been prepared and validated in some catalytic applications [16, 80, 139-143]. In this work, density functional theory (DFT) modeling sheds light on the crucial carbon-carbon coupling step at the center of this finding.

5.2 Calculation Methods

Plane-wave DFT calculations were carried out using the Vienna Ab initio Simulation Package (VASP) [26]. We described the exchange-correlation interaction of electrons by the generalized gradient approximation (GGA) in the form of Perdew-Burke-Ernzerhoff (PBE) [39] to take into account the electron-electron interaction. For the long-range interactions, we include

DFT-D3 [44] correction. For the treatment of interaction between electrons and nuclei, we use the approach of projector-augmented waves of Bloch [54] in the implementation of Kresse and Joubert [55]. We use cutoff energy of 500 eV for kinetic energy of plane-wave expansion and one k-point in performing integration over the Brillouin zone. We relax all atoms in the systems by using residual forces threshold of 0.01 eV/Å on each atoms and total energy threshold of 10^{-5} eV. For activation barriers (E_b) calculation, we use the climbing-image nudged elastic band (CI-NEB) method [59].

5.3 Results and Discussion

Continuing the success of previous computational work [23, 72, 114], in which the alcohol synthesis from syngas (CO and H_2) was shown to be feasible on Au_{13} nanoparticles stabilized by interactions with a single layer of MoS_2, we use the same supercell setup to study the process of higher alcohol formation. Based on the study of CO hydrogenation on MoS_2-supported Au_{13} [23], we can easily get the energy profile of $CH_3OH_{(g)} \rightarrow CH_3OH^*$ and $CH_3OH^* \rightarrow CH_3O^* + H^*$. With continuous dissociation, one can get product methyl CH_3^*, which is the main reactants for C-C coupling via reacting with CO. Following these initial reactions, we study the important reaction, which are listed them in Table 5.1.

Table 5.1 Considered reaction steps with activation barriers (E_b) and reaction energy (ΔE). The subscript (g) represent a gas specie. The superscript * together with specie represent an adsorbed specie. The isolated symbol * without specie represents a surface site.

No.	Equation	E_b (eV)	ΔE (eV)
R1	$CH_3O^* \rightarrow CH_3^* + O^*$	1.57	0.76
R2	$CH_3OH^* \rightarrow CH_3^* + OH^*$	1.99	0.87
R3	$OH^* \rightarrow O^* + H^*$	2.15	1.84
R4	$O^* + O^* \rightarrow O_2^*$	0.33	-1.16
R5	$O^* + CO^* \rightarrow CO_{2(g)} + *$	0.03	-2.23
R6	$CH_3^* + CO^* \rightarrow CH_3CO^*$	0.69	-0.40
R7	$CH_3^* + CHO^* \rightarrow CH_3CHO^*$	0.27	-0.67
R8	$CH_3CO^* + H^* \rightarrow CH_3CHO^*$	0.47	-0.24
R9	$CH_3CO^* + H^* \rightarrow CH_3COH^*$	0.54	0.10
R10	$CH_3CHO^* \rightarrow CH_3CHO_{(g)} + *$	0.39	0.39
R11	$CH_3CO^* + OH^* \rightarrow CH_3COOH^*$	0.00	-1.12

5.3.1 Dissociation of Methanol

CH_3* and H* can be dissociative from methanol via reactions such as $CH_3OH^* \rightarrow CH_3O^* + H^*$ (O-H bond scission), $CH_3O^* \rightarrow CH_3^* + O^*$, and $CH_3OH^* \rightarrow CH_3^* + OH^*$ (O-C bond scission). Since $CH_3OH^* \rightarrow CH_3O^* + H^*$, is ready shown in Ref [23], we continually calculate dissociation of CH_3O^* as R1: $CH_3O^* \rightarrow CH_3^* + O^*$ and CH_3OH^* (O-C bond scission) as R2: $CH_3OH^* \rightarrow CH_3^* + OH^*$, listed in Table 5.1. For the reactions R1 and R2, we show the reaction details of and are activation barrier (E_b) and reaction energy (ΔE) with geometry views of initial, transition, and final states in Figure 5.1, respectively. In Figure 5.1 (a), it takes 1.57 eV for CH_3O^* dissociated to CH_3^* and O* via C-O breaking, endothermic with reaction energy of 0.76 eV. While in R2, the dissociation of CH_3OH^* into CH_3O^* and H* via O-H bond breaking is an endothermic reaction with a high barrier of 1.99 eV. Because of their high activation barriers, R1 and R2's reaction remains at a low reaction rate. However, consider another reactant CO involving the reactions, the dissociation of methanol would be promoted, which we will discuss in the following section.

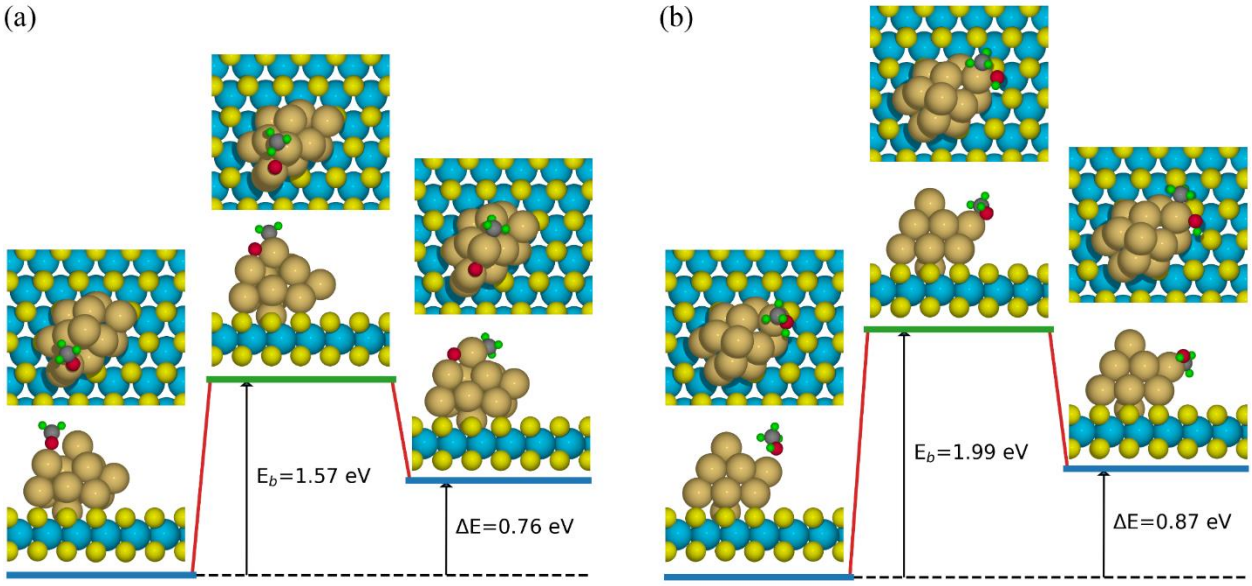

Figure 5.1 Reaction pathways of $CH_3O^* \rightarrow CH_3 + O^*$ (a) $CH_3OH^* \rightarrow CH_3^* + OH^*$ (b). Left, central, and right cartoons show both top and side views of initial, transition, and final states, respectively. Blue, yellow, gold, grey, red, and green balls represent Mo, S, Au, C, O, and H atoms, respectively. E_b and ΔE are activation barrier and reaction energy, respectively.

5.3.2 CO Oxidation and Reactions with Oxygen Participating

Since pecies CH_3^*, O*, H* and OH* are main products from R1 and R2, we look beyond to see how OH* and O* will react with species. We calculated R3: $OH^* \rightarrow H^* + O^*$ shown in Figure 5.2 (a), whose activation barrier being very high as 2.25 eV, indicating bond of O-H hard to break on Au_{13}. The reverse reaction of R3: $OH^* \rightarrow H^* + O^*$ is $H^* + O^* \rightarrow OH^*$, found as an extremely exothermic reaction, showing very energy favorable for O* reacting with H*. So the production of O* will be limited existing since the OH* formation (the reverse reaction of R3).

Figure 5.2 (b) shows the potential energy profile for the formation of O_2^* from O*. Two O* takes activation energy of 0.33 eV via O-O bond formation to become O_2^*, and it is an

exothermic reaction with ΔE= -1.16, showing very energetic favorable and can decrease the likelihood of the existence of O*.

Syngas CO is main reactant and $CO_{(g)} \rightarrow CO^* + *$ is a spontaneous on Au_{13} [23]. By our calculation results, we find adsorbed CO* prefer to react with O* to directly form $CO_{2(g)}$, which is very energetic favorable (also described on Au_{29} supported by MoS_2 [72]). We show the detailed reaction $O^* + CO^* \rightarrow CO_{2(g)} + *$ as R5 in Figure 5.2 (c). Since the reaction of CO oxidation to CO_2 is a huge exothermic reaction with a slight barrier of 0.03 eV, amount of O* would be taken away by CO* via C-O bond formation, also decreasing the probability of the existence of O*.

Looking at $H^* + O^* \rightarrow OH^*$, R4: $O^* + O^* \rightarrow O_2^*$ and R5: $O^* + CO^* \rightarrow CO_{2(g)} + *$, we find O* is hardly existing for a long time, since O* will be easy to reaction with H* (formation of O-H bond), O* itself (oxygen molecule formation), and CO* (form to CO_2 by CO oxidation). There three reactions, especially CO oxidation (since under a CO-rich environment) not only largely decrease amount of O*, but also promote the dissociation of methanol ($CH_3OH^* \rightarrow CH_3O^* + H^*$, R1: $CH_3O^* \rightarrow CH_3^* + O^*$, and R2: $CH_3OH^* \rightarrow CH_3^* + OH^*$). Besides reaction related to CO, OH* could also react with H* to form H_2O on gold [144]. However R5: $O^* + CO^* \rightarrow CO_{2(g)} + *$, play the most important role (since the amount of CO is huge and very low barrier), we can neglect those reactions between OH* and H*.

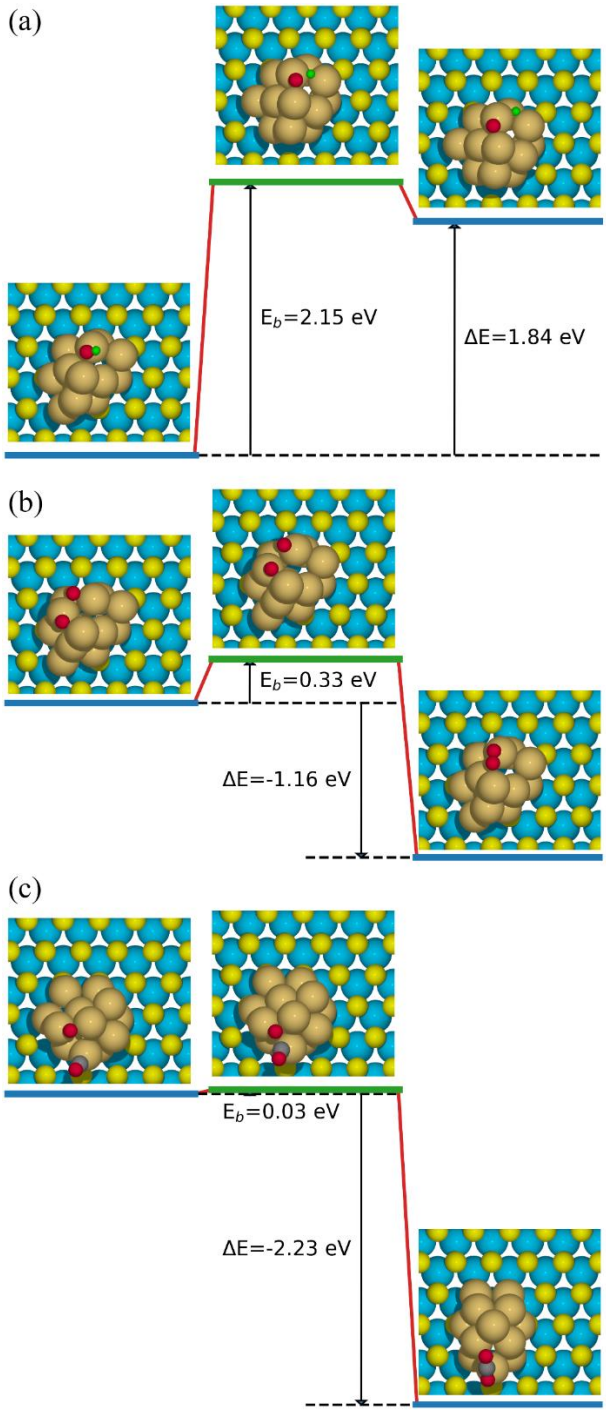

Figure 5.2 Reaction pathways of OH* → H* + O* (a), O* + O* → O_2* (b), and O* + CO* → $CO_{2(g)}$ + * (c). Left, central, and right cartoons show both top views of initial, transition, and final states, respectively. Blue, yellow, gold, grey, red, and green balls represent Mo, S, Au, C, O, and H atoms, respectively. E_b and ΔE are activation barrier and reaction energy, respectively.

5.3.3 C-C Bond Formation

Based on precious section study, if we under the environment surrounded by gas mixture gas of CH_3OH and CO, there will be CO*, CH_3*, H* and less OH*, and very limited O* exiting on MoS_2-supported Au_{13}. As efficient C-C coupling is typically based on the reactant CO* and CH_3* [111], we first examine what kind of co-adsorption of CH_3* and CO* has the lowest total-energy. Then we perform the CI-NEB calculation on the reaction CH_3* + CO* → CH_3CO*, labeled as R6 in Table 5.1. We show geometries and energy profile in Figure 5.3 (a) with the initial state, transition state, and final state, respectively. We could see CH_3* and CO* are firstly adsorbed on two different Au sites in the initial state, then CH_3* moves forwards to CO* on the same Au site accompanied by formation of C-C bond beginning in the transition state, finally the product acetyl (CH_3CO*) made itself to stay in the lowest-total energy condition as the final state. Our calculations indicate that the C-C coupling via CH_3* + CO* → CH_3CO* on Au_{13} is well feasible because it is exothermic and with a low barrier as 0.69 eV.

Besides CH_3* + CO* → CH_3CO*, CHO* (a main immediate species of CO hydrogenation [23]) could also be a reactant with CH_3*. After performing the CI-NEB calculation on CH_3* + CHO* → CH_3CHO*, we got the activation barrier of 0.27 eV and reaction energy of -0.67 eV, an exothermic reaction, labeled as R7 in Table 5.1. With the initial state, transition state, and final state shown in Figure 5.3 (b), we find CHO* preforms similar geometry changing and reaction movement like CO* (in R6) to react with CH_3*. Through the reaction R7: CH_3* + CHO* → CH_3CHO* together with R6, we can find Au_{13} is facile on C-C formation.

Considering the two reactions CH_3* + CO* → CH_3CO* and CH_3* + CHO* → CH_3CHO*, we conclude that the formation of the C-C bond is favorable on Au_{13}. Some CO* may even be hydrogenated to CHO* (CO* + H* → CHO*, with E_b =0.83 eV and ΔE = -0.4 eV in Ref [23]), CHO* will then continually react with CO* to generate CH_3CHO* in the energy favorable way. Our calculations indicate that the formation of a C-C bond via R6 (between the adsorbed CH_3* species and a CO*) and via R7 (between the adsorbed CH_3* species and the adsorbed CHO*) on Au_{13} are both well feasible (the reactions are exothermic and the activation barriers comparatively low as 0.69 eV and 0.27 eV, respectively). What is more is that C-C formation utilizes a lot of CH_3* and promotes dissociation of methanol reaction.

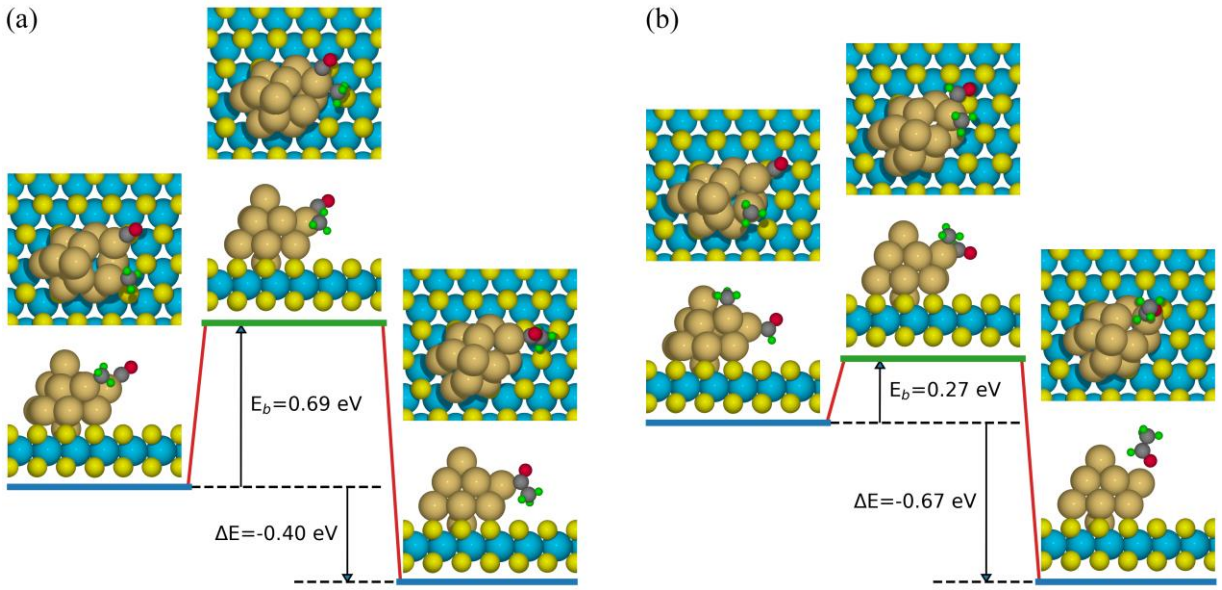

Figure 5.3 Reaction pathways of CH_3* + CO* → CH_3CO* (a) and CH_3* + CHO* → CH_3CHO* (b). Left, central, and right cartoons show both top and side views of initial, transition, and final states, respectively. Cyan, yellow, gold, grey, red, and green balls represent Mo, S, Au, C, O, and H atoms, respectively. E_b and ΔE are activation barrier and reaction energy, respectively.

5.3.4 Hydrogenation of Acetyl

After formation of acetyl (CH_3CO^*), hydrogenation of CH_3CO^* can be active with another available hydrogen (H*). In our calculation results, we find that there are two possible reaction pathways. The first possible reaction pathway is that the H* react with the one of carbon atoms of CH_3CO^*, generating CH_3CHO^* (acetaldehyde), preforming as $CH_3CO^* + H^* \rightarrow CH_3CHO^*$ (labeled as R8 in Table 5.1 and shown in Figure 5.4 (a)). In the initial state, H* and CH_3CO^* are separately absorbed on two different Au sites. Then H* moves forward to CH_3CO^*, being co-adsorbed with CH_3CO^* at the same Au site in the transition state, at the same time H* intends to react with CH_3CO^* via H-C bond formation. Finally, CH_3CHO^* intends to let its oxygen atom bind with the Au site. As depicted in Figure 5.4 (a), the barrier for this reaction is 0.47 eV with an exothermic reaction energy of -0.24 eV, indicating that Au_{13} promoted hydrogenation of acetyl to acetaldehyde. Moreover, acetaldehyde only needs to overcome a barrier of 0.39 eV for desorption (labeled as R10 in Table 5.1 and shown in Figure 5.5 (a)).

The second possible reaction pathway is that H* comes to react with the oxygen atom of CH_3CO^* forming: $CH_3CO^* + H^* \rightarrow CH_3COH^*$, labeled as R9 in Table 5.1 and shown in Figure 5.4 (b). Although the initial state is same as R8's, the pathway is quite different such that CH_3CO^* rotates itself first, letting its oxygen atom get closer to the absorbed H* (H* absorbed on the neighboring Au site). Next H* is going to react with the oxygen atom of CH_3CO^*, as the approached distance between hydrogen and oxygen atom is 1.487 Å, shown in the transition state. Finally, after "pick up" of H* via O-H bond formation, CH_3COH^* rotates itself until reaching a stable geometry. The reaction has the activation barrier of 0.54 eV and being slightly endothermic with the reaction energy of 0.10 eV.

Comparing with the pathway R8: $CH_3CO^* + H^* \rightarrow CH_3CHO^*$ and R9: $CH_3CO^* + H^* \rightarrow CH_3COH^*$ in Figure 5.4, we find the reaction pathway of CH_3CHO^* formation (R8) is more energetically favorable than CH_3COH^* formation (R9). Although R9 is not energetically favorable as R8, R9 with a low activation energy of 0.54 eV will still be a potential competitive reaction to R8. What is more is that the product of R9 is CH_3COH^*, an important immediate species for the formation of ethanol. Continuous hydrogenation of CH_3COH^* to CH_3CHOH^*, and then to $CH_3CH_2OH^*$ can get one of our desired higher alcohol production: ethanol, which intend to pursue in further studies. So, by showing that R8: $CH_3CO^* + H^* \rightarrow CH_3CHO^*$ and R9: $CH_3CO^* + H^* \rightarrow CH_3COH^*$ with low activation barriers as 0.47 eV and 0.54 eV, respectively, we find that Au_{13} is feasible for hydrogenation of acetyl.

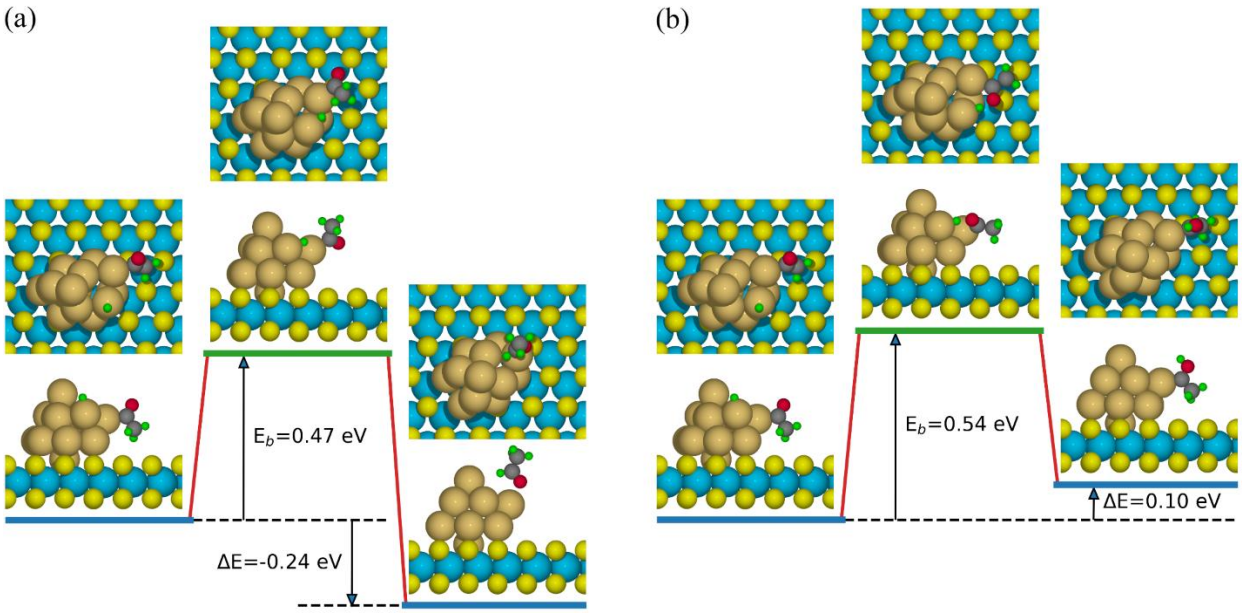

Figure 5.4 Reaction pathways of $CH_3CO^* + H^* \rightarrow CH_3CHO^*$ (a) and $CH_3CO^* + H^* \rightarrow CH_3COH^*$ (b). Left, central, and right cartoons show both top and side views of initial, transition, and final states, respectively. Cyan, yellow, gold, grey, red, and magenta balls represent Mo, S, Au, C, O, and H atoms, respectively. E_b and ΔE are activation barrier and reaction energy, respectively.

Besides hydrogenation of acetyl reaction pathways, Figure 5.5 (b) shows that acetic acid (CH_3COOH^*) can easily be formed from OH* and $CH_3CO,^*$ spontaneously. Since the amount of H* is larger than OH*, this reaction R10: $CH_3CO^* + OH^* \rightarrow CH_3COOH^*$ is only considered as a side reaction.

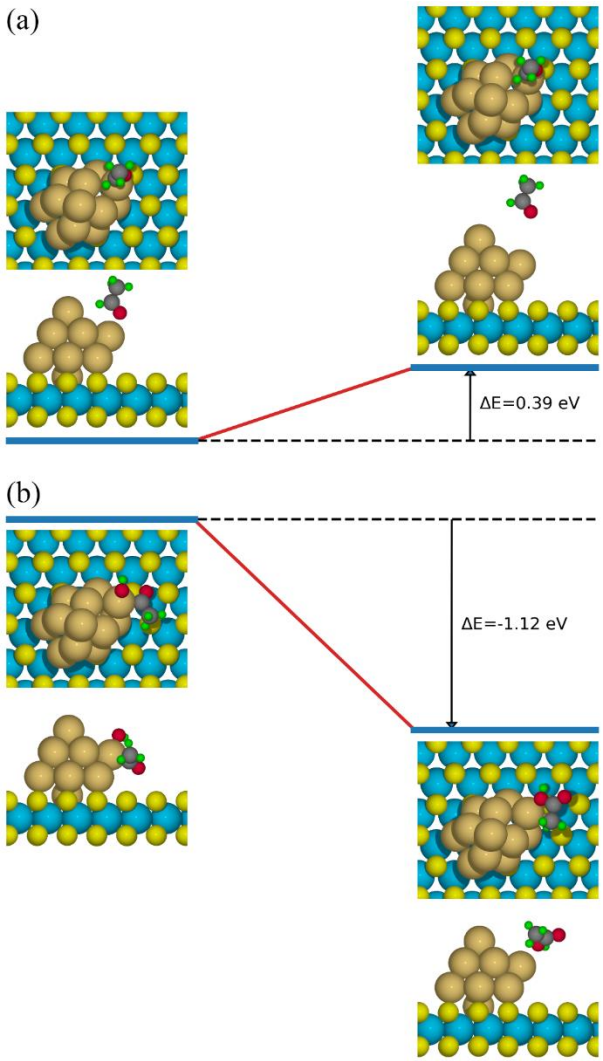

Figure 5.5 Reaction pathways of $CH_3CHO^* \rightarrow CH_3CHO_{(g)} + *$ (a) and $CH_3CO^* + OH^* \rightarrow CH_3COOH^*$ (b). Left, central, and right cartoons show both top and side views of initial, transition, and final states, respectively. Cyan, yellow, gold, grey, red, and magenta balls represent Mo, S, Au, C, O, and H atoms, respectively. E_b and ΔE are activation barrier and reaction energy, respectively.

The adsorption sites and reaction pathways, shown in Figure 5.3 and Figure 5.4, are the result of a wide search for the lowest barrier pathway on these clusters. Close inspection reveals that the site with the lowest barriers corresponds to the least coordinated gold atom on the cluster, where the binding of the reactants is strongest. This finding highlights the importance of small clusters for this reaction to proceed. Such sites are far more common on small gold clusters compared to larger ones. Thus, the ability of even a single-layer of MoS_2 to disperse gold into nanometer-scale clusters [27] is at the root of the availability of this reaction pathway in the system at hand.

5.4 Conclusion

Employing density functional theory (DFT) based calculations, we validate that MoS_2-supported Au_{13} is capable of upconverting methanol to acetaldehyde. This result showcases the promise of gold nanoparticles on a single layer of MoS_2, discussed elsewhere [114] and speaks to the possibility of extending a short alcohol to a precursor of a longer-chain alcohol, with the correct catalyst design, as predicted by previous DFT calculations [23, 72]. Our findings highlight an important first step towards the formation of longer alcohols from methanol or even syngas using inexpensive, non-toxic, earth-abundant MoS_2 and less than a monolayer of gold. This new finding is an exciting milestone for good reasons. The basal plane of MoS_2 is inert, if we put a cluster of 13-atom gold on it; it becomes a good catalyst for C-C coupling. In our detailed computational analyses, we find that although the barrier for dissociation of methanol is high, CO can promote the dissociation of methanol via CO oxidation. We find Au_{13}/MoS_2 is a viable catalyst for the formation of acetyl with a low barrier of 0.69 eV (via the reaction between

methyl and carbon monoxide). Furthermore, we find that there are two competitive reaction pathways of acetyl hydrogenation: 1) $CH_3CO^* + H^* \rightarrow CH_3CHO^*$ and 2) $CH_3CO^* + H^* \rightarrow CH_3COH^*$, where the former one is more energetically favorable since it has a lower barrier of 0.47 eV and being exothermic. In addition, the reaction for acetaldehyde to convert from absorbed to gas phase only takes 0.39 eV. Overall, based on our systematic analyses of reactions, we find Au_{13}/MoS_2 is a good catalyst for converting the mixture gas of carbon monoxide and methanol to acetaldehyde. Our future work will study more steps for higher alcohol synthesis pathways and we will explore experimental evidence for our computational prediction.

CHAPTER 6: MoS_2-SUPPORTED Au_{31} FOR CO HYDROGENATION: A FIRST-PRINCIPLE STUDY

Alcohol synthesis from syngas (CO, H_2) is an important part of an economy based on renewable fuels. Rational designing of efficient catalyst material for such synthesis is in great demand because of the limitation of the current state-of-the-art catalysts. We report our density functional theory based calculations of the hydrogenation of CO on 31-atom, bilayer Au cluster supported on single-layer MoS_2 (Au_{31}/MoS_2). In accordance with previous investigations [27], we found that the gold atoms at the edge were most affected by substrate interaction and had strong affinity for CO. Furthermore, molecular H_2 could only physisorb on Au_{31}/MoS_2 and the activation barrier of H_2 dissociation was 0.63 eV, lower than that on Au_{13} [23]. Interestingly, we found that Au_{31}/MoS_2 offers excellent activity toward methanol synthesis, via two competitive reaction pathways: 1) CHO* → CH_2O* → CH_3O* → CH_3OH*; 2) CHO* → CHOH* → CH_2OH* → CH_3OH*, the former being kinetically more favorable. We compare our findings with that on Au_{13} [23] to elucidate the influence of size and shape of nanoparticles on their catalytic performance.

6.1 Introduction

Supported gold (Au) nanoparticles (NPs) are exhibit a high catalytic activity for important chemical reactions [145], such as CO oxidation [115] and water-gas shift reaction [146]. Majority of the work focus on metal oxide supports such as Al_2O_3 [147, 148] and TiO_2 [149-156], in which the interface between NPs and the supports play an important roles in facilitating reactions. Recently, 2D materials are also utilized for supporting such NPs for

catalytic applications. Among them, Molybdenum Disulfide (MoS_2)-supported Au NPs display unique chemical properties. Since the basal plane of MoS_2 is inert, the NPs-MoS_2 interface is not behave active [23, 72] like transition metal oxide-NP ones, which brings reactions to the low coordinated sites on NPs that are way from the interface. For example, MoS_2-supported Au NP has showed serval reactions such as CO hydrogenation [23], O_2 decomposition [72], and CO oxidation [114] occur at the top of NPs.

Recently a combined experimental-computational investigation found that single-layer MoS_2 islands are capable of interacting sufficiently with gold atoms have affinity for binding CO [27]. The islands are shown to be bilayer thick and the sites at the edges of the islands are shown to be the adsorption sites for CO binding. Since the sites are much closer to MoS_2 basal plane than those active sites in 3D NP shown in prior works [23, 72, 114], it is expected that the reactivity of the Au islands may not be the same as that of 3D Au NPs. It is, thus, necessary to revisit the investigation of the reactivity of MoS_2-supported Au NPs to draw conclusion for realistic MoS_2-supported Au NPs.

In this work, we choose to investigate, on the basic of density functional theory (DFT) calculation, the hydrogenation of CO to methanol because it has been detailed and systematically studied by Rawal *et al* [23] on MoS_2-supported Au_{13} NPs, which will serve as benchmark. Alcohol synthesis from syngas (CO, H_2) is an important part of an economy based on renewable fuels. Rational designing of efficient catalyst material for such synthesis is in great demand because of the limitation of the current state-of-the-art catalysts. We choose MoS_2-supported bilayer Au_{31} NPs as our model catalyst because its size is large enough for reassembling MoS_2-supported bilayer Au islands but is not too large to computationally formidable. We will show

the feasible adsorption of H_2 and CO on the model catalyst, and illustrate two effective reaction pathways from CO to methanol. Our theoretical studies on the bilayer 31-atom cluster of gold supported on MoS_2 help us to better understand the catalytic performance of realistic Au nanoparticles supported by MoS_2.

6.2 Computational Details

Our DFT simulations were carried out using VASP code [26], applying the projector-augmented wave (PAW) [54, 55] and plane wave basis set methods. Perdew−Burke−Ernzerhof functional (PBE) [39] was employed for describing the electronic exchange correlation . We use DFT-D3 [44] correction for accounting the van der Waals interaction. The energy cutoff for plane-wave expansion was set at 500 eV. Our substrate model system constructed from an 8 × 8 single layer MoS_2 (optimized lattice parameter a = 3.16 Å) with setting a vacuum of 15 Å between periodical image along the z-axis. The Au_{31} cluster is chosen to have hexagonal symmetry, similar to the one used in Ref [27]. We sampled the Brillouin Zone with on k-point at the zone center. For structural relaxation, we set the residual force at 0.01 eV/Å. All adsorption energies (E_{abs}) were calculated by: $E_{abs} = E_{(adsorbate/slab)} - (E_{(adsobate)} + E_{(slab)})$, in which $E_{adsorbate/slab}$, $E_{adsorbate}$ and E_{slab} represent the total energies of adsorbates/slab system, adsorbates, and slab (representing Au_{31}/MoS_2 composite system), respectively. We use the implemented Bader's method [157, 158] to estimate the charge transfer and we use the climbing-image nudged elastic band (CI-NEB) method [59] for activation barriers (E_b) calculation.

6.3 Results and Discussion

Figure 6.1 (a) shows the top view of structure of a bilayer 31-atom cluster of gold on MoS_2. Based on the geometry of the bilayer Au_{31} and its symmetry, we find there are six kinds of sites, which labeled as #1, #2 and #3 in the top layer, whereas #4, #5, and #6 in the bottom layer. Figure 6.1 (b) shows atomic charge of each individual Au atom evaluated using Bader Charge method [157, 158]. As expected, the distribution of atomic charges on the Au_{31} cluster reflects the cluster's 3-fold symmetry, although some minor irregularities are seen that could be due to numerical errors. More importantly, except for 3 Au atoms with label #6, the outermost Au atoms are negatively charged. The analysis also shows that the 7 inner Au atoms in the bottom layer, which are not visible in Figure 6.1 (a and b), are positively charged with a total charge of +0.42 |e|. Similar to the case of Au_{13} [23], we found that the net charge of the bilayer 31-atom Au cluster is +0.13 |e|.

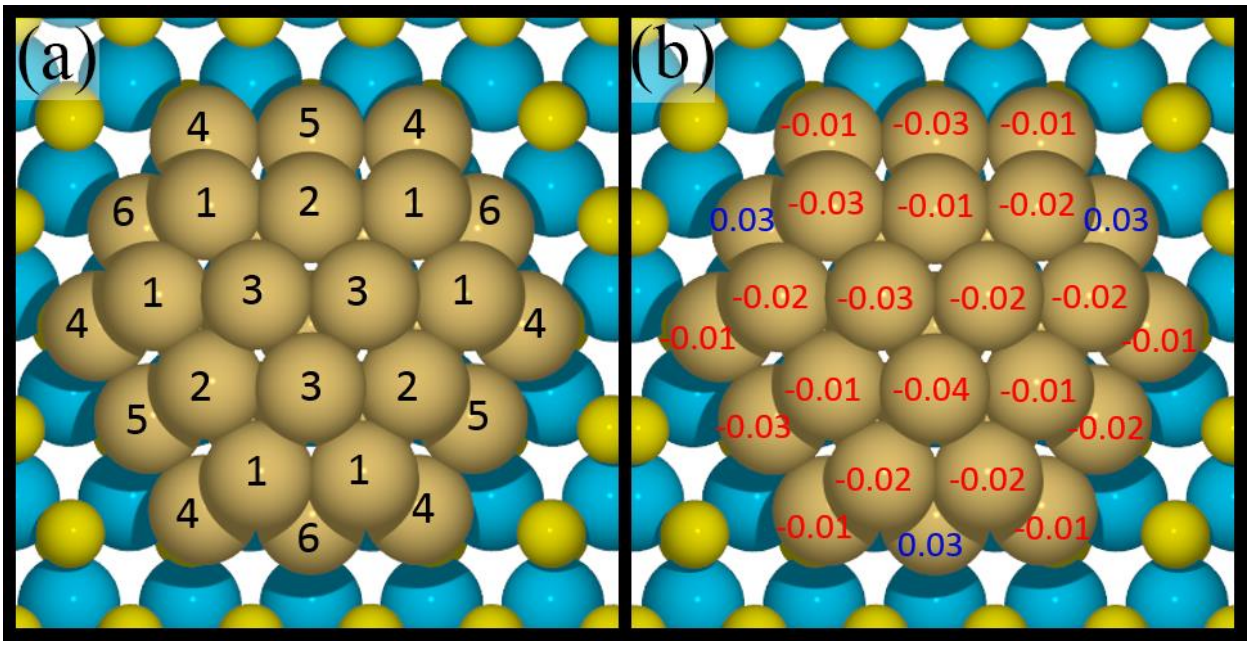

Figure 6.1 (a)Top view of bilayer Au31 supported by MoS2 together with labels for each Au atom. (b) Atomic charge of Au atoms based on Bader charge analysis. Positive and negative numbers indicate positively (donate electron) and negatively (accept electron), respectively, charged Au atom (unit is |e|).

6.3.1 Adsorption of CO

Adsorption of CO is a key step in methanol synthesis through the CO hydrogenation route. It is therefore important to identify the atomic site for CO activation and to determine how strongly CO binds on Au_{31}/MoS_2. The optimized geometries of CO on Au_{31} supported on defect-laden MoS_2 on different Au sites are shown in Figure 6.2. The adsorption energy and geometrical parameters for all configurations are summarized in Table 6.1. In our calculation results, CO prefers to adsorb adsorbs at #1 Au site in Figure 6.2 (a) with an adsorption energy of −0.97 eV, with the O-C distance of 1.152 Å and C-Au distance of 1.948 Å. The common feature in the six configurations is that CO adsorbs at Au atom via Au–C bonding.

Table 6.1 Adsorption energy and geometrical parameters of CO adsorbed at different Au sites of MoS_2-supported Au_{31}

Configurations	Site	E_{ads} (eV)	$d_{(O-C)}$ (Å)	$d_{(C-Au)}$ (Å)	$\theta_{(O-C-Au)}$ (°)
a	#1	-0.97	1.152	1.948	179.3
b	#2	-0.58	1.151	1.948	177.5
c	#4	-0.56	1.156	2.157	133.8
d	#4	-0.79	1.153	1.980	163.8
e	#5	-0.70	1.153	2.002	127.4
f	#6	-0.24	1.155	1.960	157.8

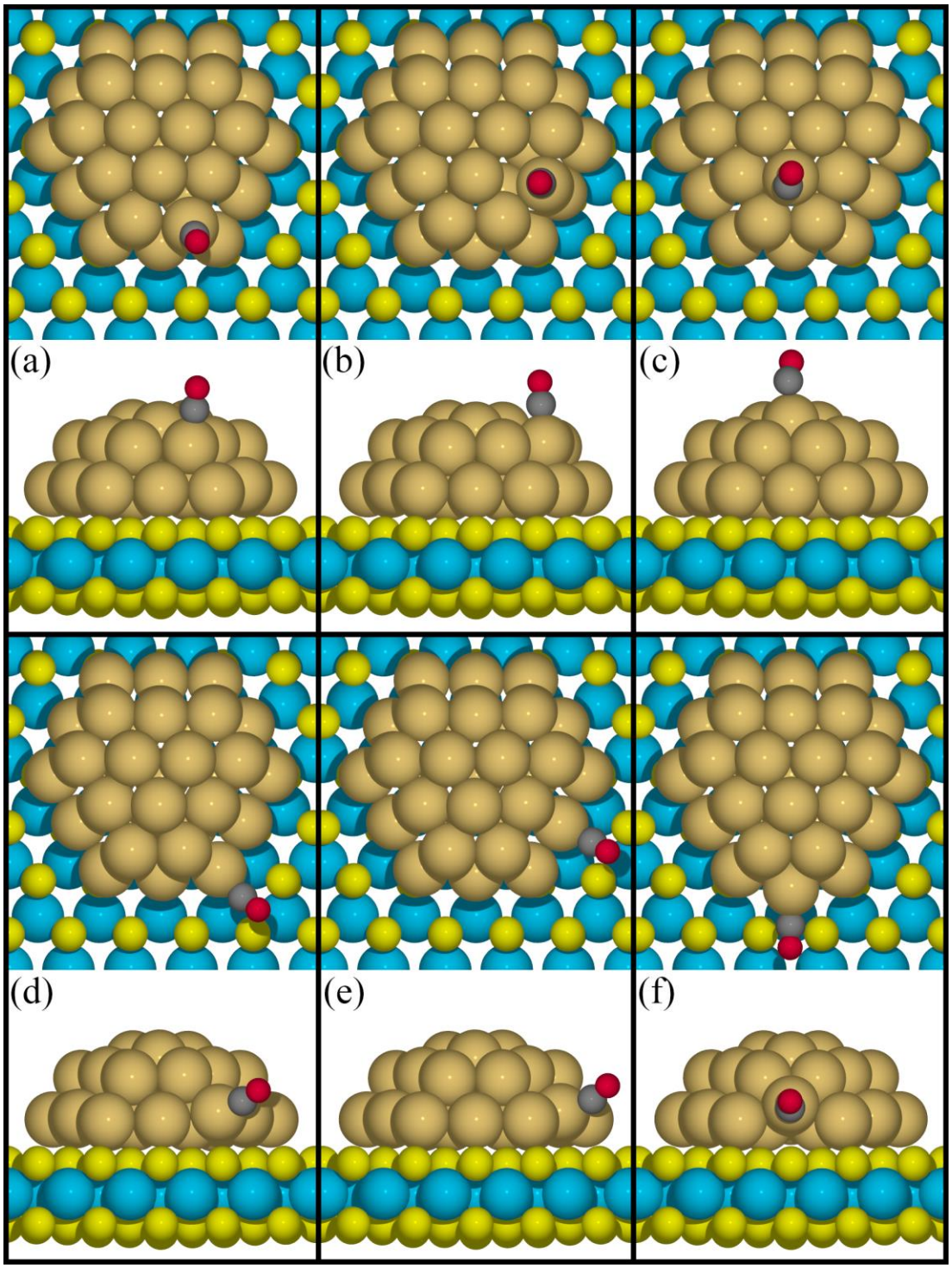

Figure 6.2 Optimized geometries of CO adsorbed on Au_{31} supported on MoS_2 at different sites. The black and red balls represent the C and O atoms, respectively. The top and bottom panels show the top and side views, respectively.

6.3.2 Adsorption of H_2

Adsorption and dissociation of H_2 is another key step in methanol synthesis from syngas (H_2 and CO). Here, we first identify possible sites for H_2 activation. Our DFT-optimized geometries of various configurations of H_2 on Au_{31}/MoS_2 are shown in Figure 6.3 (a-f). The adsorption energy and geometrical parameters of all considered configurations are summarized in Table 6.2. From our calculations, we find that H_2 could only physisorb on six Au sites with similar adsorption energy from -0.06 eV to -0.10 eV and with a distance of more than 2.35 Å away from the nearest Au atom. Even though there is no chemisorption, H–H bond length is found to be slightly extended to 0.755 - 0.762 Å as compared to a value of 0.750 Å in H_2 gas phase.

Table 6.2 Adsorption energy and geometrical parameters of H_2 adsorbed at different Au sites of MoS_2-supported Au_{31}

Configurations	E_{ads} (eV)	$d_{(H-H)}$ (Å)	$d_{(H-Au)}$ (Å)	$\theta_{(H-H-Au)}$ (°)
a	-0.08	0.762	2.351	175.1
b	-0.07	0.754	2.887	169.3
c	-0.06	0.753	2.940	167.9
d	-0.08	0.756	2.723	150.8
e	-0.10	0.755	2.858	169.7
f	-0.10	0.755	2.782	162.5

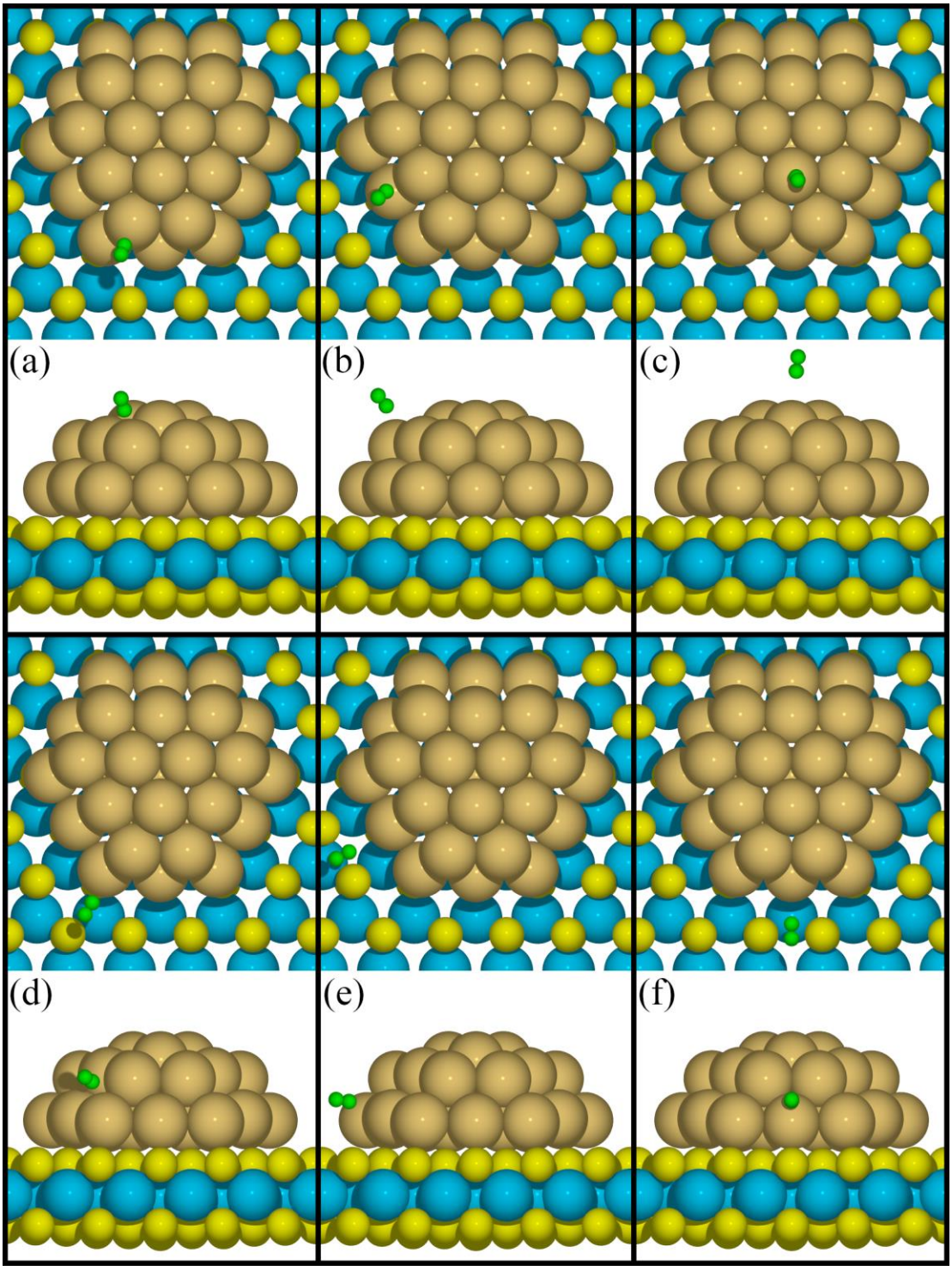

Figure 6.3 Optimized geometries of H_2 adsorbed on a bilayer 31-atom cluster of gold on MoS_2. The green balls represent the H atoms, respectively. The top and bottom panels show the top and side views, respectively.

6.3.3 Dissociation of H_2

Even though H_2 is found to be physisorbed at various places on the Au_{31} cluster, we choose configuration shown in Figure 6.4 (a) and (b) as initial states (IS) #1 and #2 for study the of H_2 dissociation. It is because these are the locations where CO binds the strongest, thus co-adsorption of CO and atomic H is preferred to form. We found that the dissociations of H_2 starting from IS#1 is slightly endothermic of 0.02 eV and with a barrier of 0.43 eV while the reaction starting with IS#2 is exothermic of -0.28 eV with the barrier of 0.63 eV. The found activation energies are both lower than 0.83 eV of H_2 dissociation on MoS_2-supported Au_{13} [23]. Moreover, comparing some barrier of reactions in CO hydrogenation route (as we shall see), the barrier of H_2 dissociation is relatively smaller.

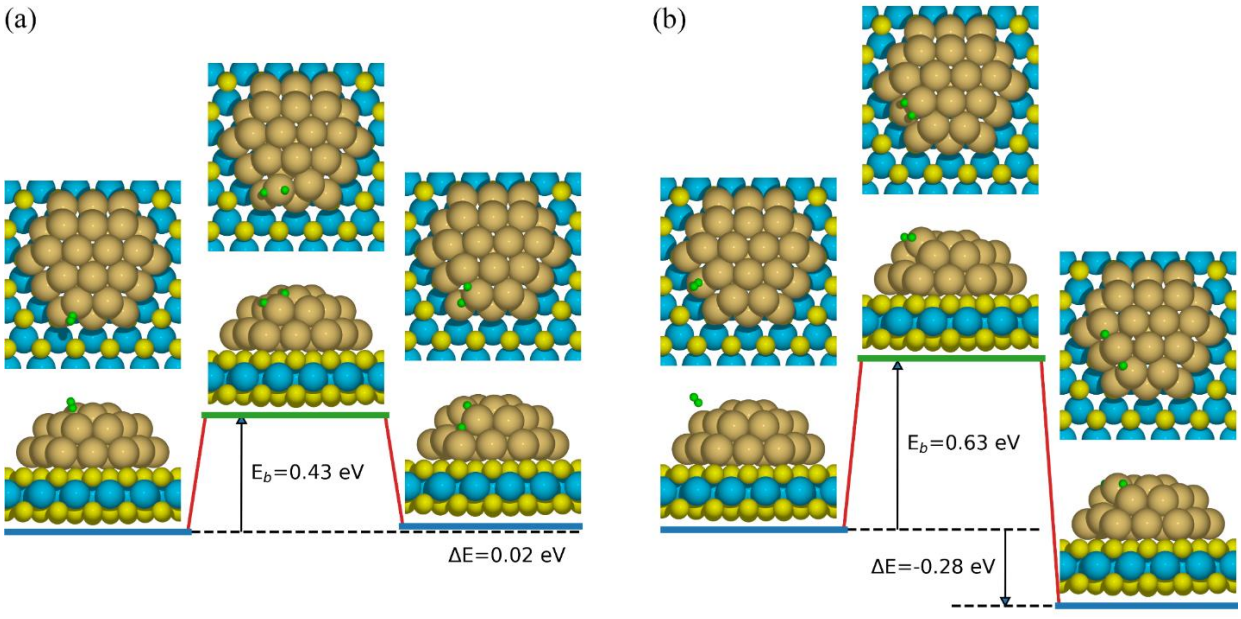

Figure 6.4 Two possible reaction pathways of dissociation of H_2 from #1 physical-adsorption sites and #2 physical-adsorption (b). Left, central, and right cartoons show both top and side views of initial, transition, and final states, respectively. Cyan, yellow, gold, grey, red, and green balls represent Mo, S, Au, C, O, and H atoms, respectively. E_b and ΔE are activation barrier and reaction energy, respectively.

6.3.4 Reactions for Methanol Synthesis

To study the reaction mechanism for methanol synthesis through CO hydrogenation on Au_{31}/MoS_2, we calculated the activation energy barriers and reaction energy for all elementary steps and listed them in Table 6.3. For the configurations of initial state, transition state, and final state of each elementary step, we displayed them in Figures 6.5-6.10.

R1. $CO_{(p)} + * \rightarrow CO*$. This reaction of CO from physisorb to chemisorb has no barrier and has a reaction energy of -0.95 eV. The CO* is adsorbed at site #1.

R2. $H_{2(p)} + * \rightarrow 2H*$. Among the two H_2 dissociative adsorptions considered above, we choose the one stared with IS#2. It is because the sites for the two atomic H* adsorption is different from but near by the favorite adsorption site for CO* (Site #1), which is needed for co-adsorption of CO and H* for advancing further CO hydrogenation pathway. This reaction is an exothermic reaction of -0.28 eV with an activation barrier of 0.63 eV.

Table 6.3 Considered reaction steps with activation barriers (E_b) and reaction energy (ΔE), for CO hydrogenation where the subscript (p), superscript *, and isolated symbol * represent physisorb, an adsorbed specie, and a surface site, respectively.

No.	Equation	E_b (eV)	ΔE (eV)
R1	$CO_{(p)} + * \rightarrow CO*$	0.00	-0.95
R2	$H_{2(p)} + * \rightarrow 2H*$	0.63	-0.28
R3	$CO* + H* \rightarrow CHO* + *$	1.25	0.46
R4	$CO* + H* \rightarrow COH* + *$	2.44	1.21
R5	$CHO* + H* \rightarrow CH_2O* + *$	0.53	-0.07
R6	$CHO* + H* \rightarrow HCOH* + *$	0.35	-0.08
R7	$CH_2O* + H* \rightarrow CH_3O* + *$	0.11	-0.25
R8	$CH_2O* + H* \rightarrow CH_2OH* + *$	0.37	-0.77
R9	$CH_3O* + H* \rightarrow CH_3OH* + *$	0.12	-1.03
R10	$CH_3OH* \rightarrow * + CH_3OH_{(p)} + *$	0.45	0.45
R11	$HCOH* + H* \rightarrow CH_2OH* + *$	0.21	-0.67
R12	$CH_2OH* + H* \rightarrow CH_3OH* + *$	0.62	-0.74
R13	$CH_3OH* \rightarrow * + CH_3OH_{(p)} + *$	0.45	0.45
R14	$CH_2O* \rightarrow CH_2O_{(p)} + *$	0.29	0.29

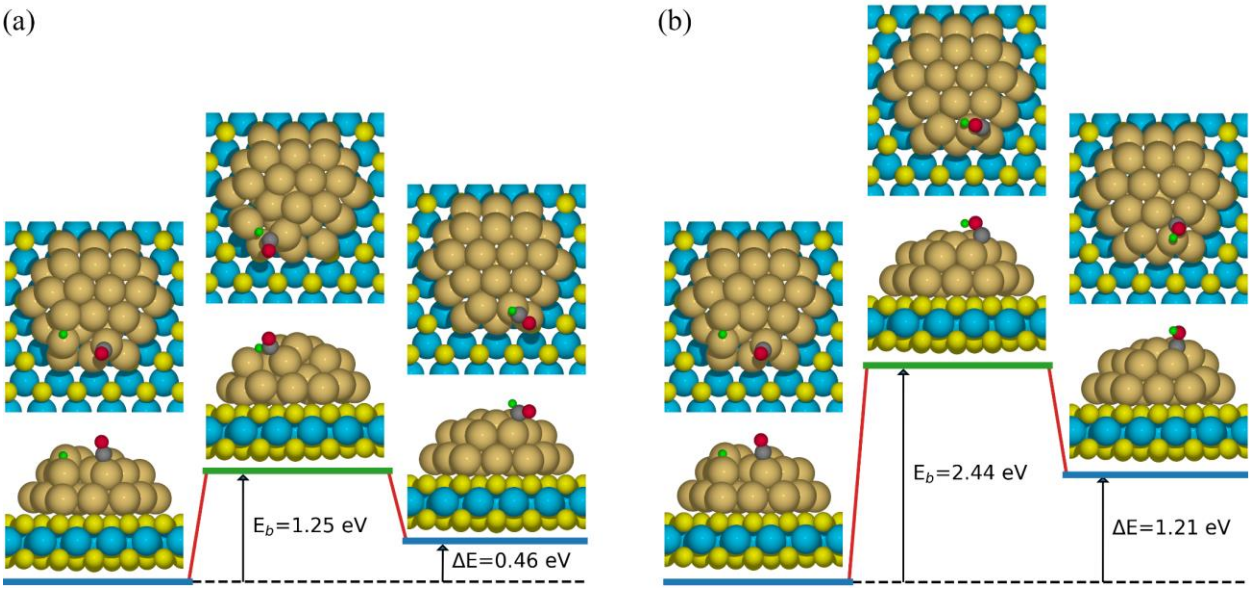

Figure 6.5 Reaction pathways of CO* + H* → CHO* + * (a) and CO* + H* → COH* + * (b). Left, central, and right cartoons show both top and side views of initial, transition, and final states, respectively. Cyan, yellow, gold, grey, red, and green balls represent Mo, S, Au, C, O, and H atoms, respectively. E_b and ΔE are activation barrier and reaction energy, respectively.

R3. CO* + H* → CHO* + *. Formyl (CHO*) is formed by CO* reacting with H*. As presented in Figure 6.5 (a), this step is endothermic of 0.46 eV and has an activation barrier of 1.25 eV. In the initial state, CO* and H* are separately adsorbing onto two Au sites. NEB calculated reaction pathway indicates that CO* diffuses towards H*, making carbon atom get closer to H* to form CHO* species. In the transition state, the geometry resembles a quadrilateral species locating at the bridge site with C−H of 1.267 Å and H-Au of 1.876 Å, respectively. Finally after attaching H*, new formed CHO* stay at a stable geometry with C−H of 1.114 Å, C-Au of 2.055 Å and $\theta_{(H\text{-}C\text{-}O)}$ of 121.7°.

R4. CO* + H* → COH* + *. The formation of Hydroxymethylidyne (COH*) is another possible reaction pathway of CO* initial hydrogenation. This step must overcome an activation barrier as high as 2.44 eV, and it is highly endothermic (1.21 eV). In the initial state of Figure 6.5

(b), the geometry of reactants CO* and H* is same as R4. Then CO* rotate itself around the carbon atom to pick up H* via O-H bond formation. Finally, COH* stayed at the bridge side among three Au atoms. Compared with the R3, CO* + H* → CHO* + *, this reaction is not energetically nor kinetically favorable due to its high barrier and endothermicity. For this reason, this reaction is not further considered in reaction pathways to methanol.

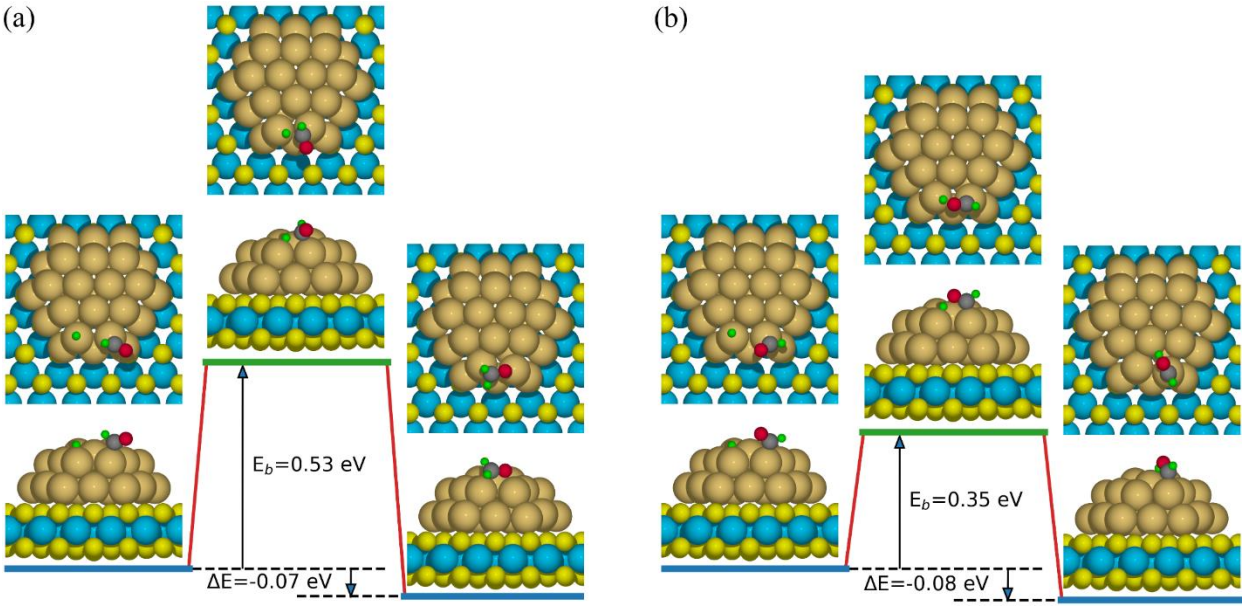

Figure 6.6 Reaction pathways of CHO* + H* → CH_2O* + * (a) and CHO* + H* → HCOH* + * (b). Left, central, and right cartoons show both top and side views of initial, transition, and final states, respectively. Cyan, yellow, gold, grey, red, and green balls represent Mo, S, Au, C, O, and H atoms, respectively. E_b and ΔE are activation barrier and reaction energy, respectively.

R5. CHO* + H* → CH_2O* + *. Formaldehyde (CH_2O*) comes from the reaction between available H* and CHO* (CHO* is the product of R3) via H-C bond formation. This reaction's activation energy barrier is 0.53 eV with a small exothermic reaction energy of -0.07 eV, shown in Figure 6.6 (b). The product CH_2O* is found adsorbed at two type #1 Au sites with C-Au of 2.274 Å and O-Au of 2.165 Å.

R6. CHO* + H* → HCOH* + *. Hydroxymethylene (HCOH*) is another possible production from the hydrogenation of CHO*, shown in Figure 6.6 (b). In the initial state, CHO* and H* separately adsorbed on two Au sites, where the oxygen atom of CHO* is tilting towards to H*. This co-adsorption geometry is different to R5's, in which carbon atom of CHO* is diffusing towards to H*. It takes an activation barrier of 0.35 eV for CHO* rotating itself ready for -OH formation, at transition state, where the distance of O-H is 1.472 Å and the distance of Au-H is 1.692 Å. The reaction is slightly exothermic with a reaction energy of -0.08 eV. While both R5 and R6 have similar reaction energy, R6 has a significantly lower reaction barrier, indicating that the formation of hydroxymethylene is kinetically more favorable than that of formaldehyde.

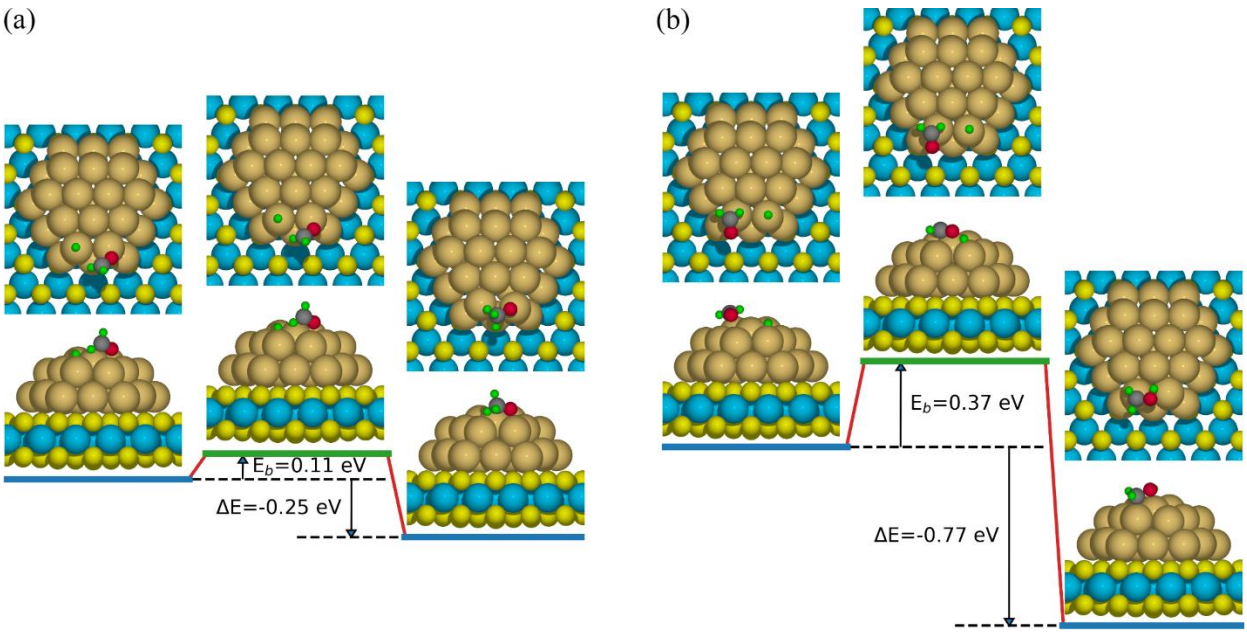

Figure 6.7 Reaction pathways of CH_2O^* + H* → CH_3O^* + * (a) and CH_2O^* + H* → CH_2OH^* + * (b). Left, central, and right cartoons show both top and side views of initial, transition, and final states, respectively. Cyan, yellow, gold, grey, red, and green balls represent Mo, S, Au, C, O, and H atoms, respectively. E_b and ΔE are activation barrier and reaction energy, respectively.

R7. $CH_2O^* + H^* \rightarrow CH_3O^* + *$. We focus possible reactions after R5 first, which is the reaction showing addition of H could react with adsorbed CH_2O^* shown in Figure 6.7 (a). We can find that there are also two possible reaction pathway for CH_2O^* hydrogenation. One is that H* react with the carbon atom of CH_2O^*, which leads to the formation of methoxyl, mark as R7, shown in Figure 6.7 (a). This step has a quite low activation barrier of 0.11 eV and reaction energy of -0.25 eV. In the final state in Figure 6.7 (a), CH_3O^* species binds like a bridge between two Au sites, where O-Au being 2.064 Å and H-Au being 2.023 Å. Another one is that H* react with the oxygen atom of CH_2O^*, which marked as R8 as following.

R8. $CH_2O^* + H^* \rightarrow CH_2OH^* + *$. The hydrogenation of formaldehyde (CH_2O^*) via O-H bond formation, resulting in CH_2OH^* with an activation energy barrier of 0.67 eV, much higher than that of CH_3O^* formation in R7 (Figure 6.7 (b)). Comparing with the total energy of R7 and R8's initial states, co-adsorption of H* and CH_2O^* in R7 is 0.14 eV lower than that in R8. Because of these two factors, we can find the reaction pathway to form CH_3O^* (via R7 in Figure 6.7 (a)) is more energetic favorable than to form CH_2OH^* (via R8 in Figure 6.7 (b)).

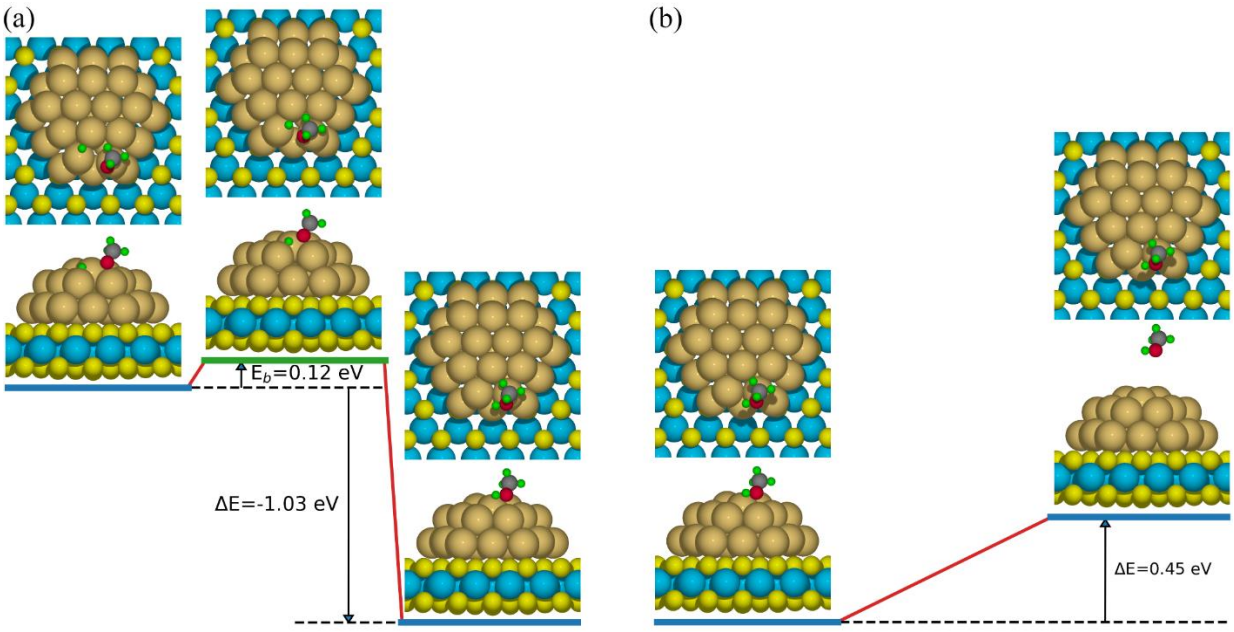

Figure 6.8 Reaction pathways of $CH_3O^* + H^* \rightarrow CH_3OH^* + *$ (a) and $CH_3OH^* \rightarrow CH_3OH_{(p)} + *$ (b). Left, central, and right cartoons show both top and side views of initial, transition, and final states, respectively. Cyan, yellow, gold, grey, red, and green balls represent Mo, S, Au, C, O, and H atoms, respectively. E_b and ΔE are activation barrier and reaction energy, respectively.

R9. $CH_2OH^* + H^* \rightarrow CH_3OH^* + *$. After the formation of CH_3O^*, adding another available H* will lead to the formation of CH_3OH^*. We label this reaction as R9 and show the detail geometries evolving in Figure 6.8 (a). While this reaction's activation barrier is as low as 0.12 eV; its reaction energy is -1.03 eV, very exothermic.

R10. $CH_3OH^* \rightarrow CH_3OH_{(p)} + *$. We got methanol absorbed on Au_{31} from R9, then we find it takes 0.45 eV to desorp to physisorb methanol shown in Figure 6.8 (b). Then from the physisorb to gas phase, it only takes 0.027 eV, and we will get our desirable product methanol (gas phase).

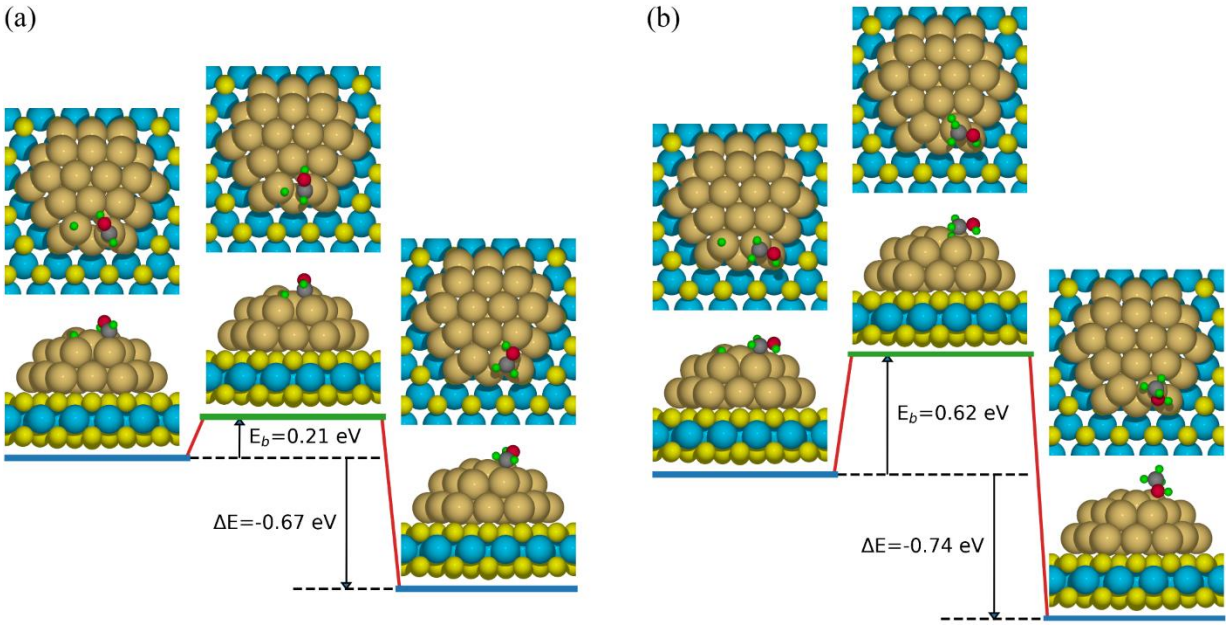

Figure 6.9 Reaction pathways of HCOH* + H* → CH_2OH* + * (a) and CH_2OH* + H* → CH_3OH* + * (b). Left, central, and right cartoons show both top and side views of initial, transition, and final states, respectively. Cyan, yellow, gold, grey, red, and green balls represent

R11. HCOH* + H* → CH_2OH* + *. We look back on the reaction R6: CHO* + H*→ HCOH* + *, whose product is Hydroxymethylene (HCOH*). If HCOH* continues to react with an available H*, we will get CH_2OH*, which reaction we labeled as R11, shown in Figure 6.9 (a). This step has the activation barrier of 0.96 eV and the reaction energy of 0.42 eV.

R12. CH_2OH* + H* → CH_3OH* + *. Following R11 reaction, another available H* could also leads the reactant CH_2OH* to the desirable product methanol, which labeled as R12 in Table 6.3, shown in Figure 6.9 (b). This step is an exothermic reaction with E_b =0.62 eV and ΔE = -0.74 eV.

With R11 and R12, we get absorb methanol, whose geometry is a little different with R9's product CH_3OH*, where the direction of hydrogen atom (from O-H bond) is opposite. For R9's CH_3OH*, the desorption process to physisorb will take 0.43 eV (we label this reaction as

R13, shown in Figure 6.10 (a)), and then it only takes 0.021 eV to gas phase, which is similar to R10's. What's more, there are also some side reactions happening simultaneously, for example, CH_2O^* desorption to physisorb $CH_2O_{(p)}$. The step's activation barrier is 0.29 eV, which we labeled as R14 and showed in Figure 6.10 (b).

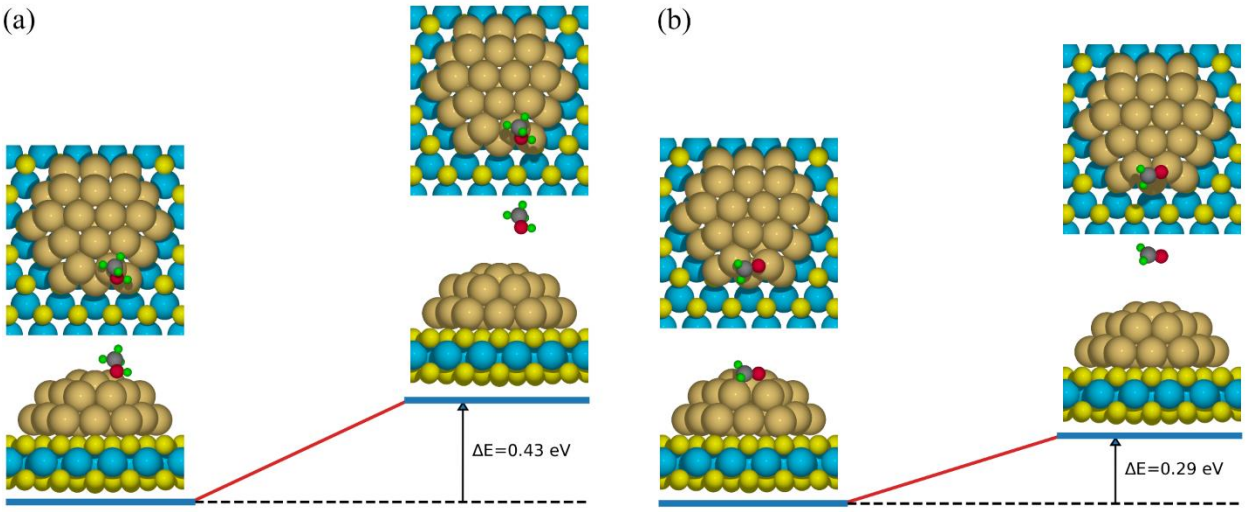

Figure 6.10 Reaction pathways of $CH_3OH^* \rightarrow CH_3OH_{(p)} + *$ (a) $CH_2O^* \rightarrow CH_2O_{(p)} + *$ (b). Left, central, and right cartoons show both top and side views of initial, transition, and final states, respectively. Cyan, yellow, gold, grey, red, and green balls represent Mo, S, Au, C, O, and H atoms, respectively. E_b and ΔE are activation barrier and reaction energy, respectively.

6.3.5 CO Hydrogenation Pathways

We set the total energy of $CO_{(g)}$ and $2H_{2(g)}$ as zero, and connected the effective reactions we discussed together, to plot the complete reaction pathway in Figure 6.11. We can find there are mainly two rotates via the following sequences: $CO^* \rightarrow CHO^* \rightarrow CH_2O^* \rightarrow CH_3O^* \rightarrow CH_3OH^*$ and $CO^* \rightarrow CHO^* \rightarrow HCOH^* \rightarrow CH_2OH^* \rightarrow CH_3OH^*$, which labeled as blue and red routes, respectively. We can find most of them are overlap showing similar catalytic properties, except for $CH_3O^* + H^* \rightarrow CH_3OH^* + *$ and $CH_2OH^* + H^* \rightarrow CH_3OH^* + *$. The

activation barrier of the former reaction is 0.12 eV, much lower than that of the latter one. It shows that the blue route would not block between CH_3O^* and CH_3OH^* in comparison with the red route between CH_2OH^* and CH_3OH^*. Based on our analysis, the synthesis of methanol on the bilayer 31-atom cluster of gold on MoS_2 prefers the pathway: $CO^* \rightarrow CHO^* \rightarrow CH_2O^* \rightarrow CH_3O^* \rightarrow CH_3OH^*$ (blue route in Figure 6.11).

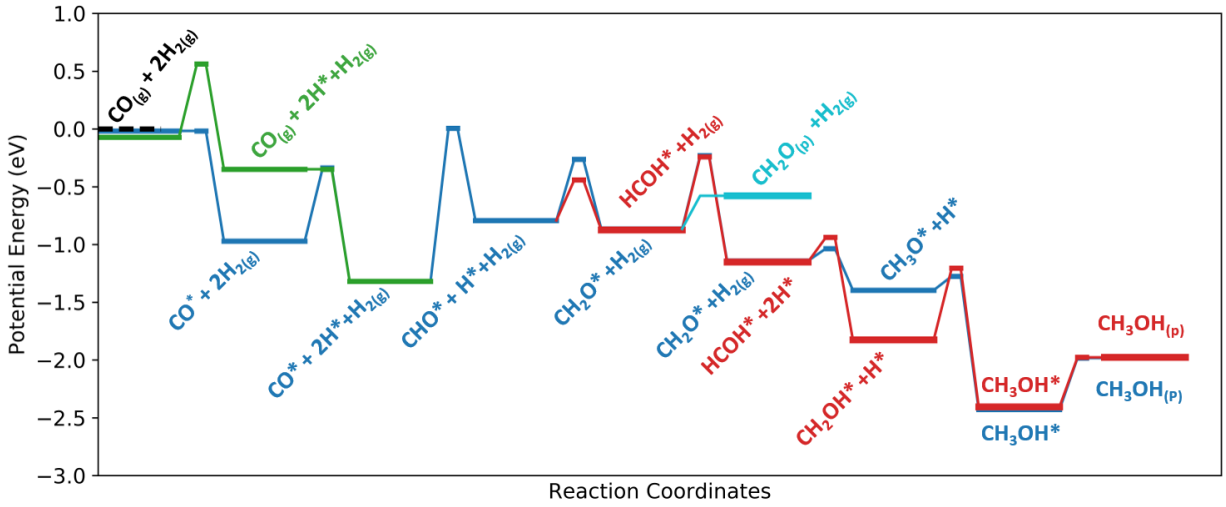

Figure 6.11 Total reaction pathways of CO hydrogenation on a bilayer 31-atom cluster of gold on MoS_2.

In the comparison with CO hydrogenation on Au_{13} [23], the barriers for the reaction $CO^* + H^* \rightarrow CHO^* + *$ (1.25 eV) and the reaction $CHO^* + H^* \rightarrow CH_2O^* + *$ (0.53 eV) are higher (1.14 eV and 0.23 eV on Au_{13} ,respectively). However for H_2 dissociation, the reaction on Au_{31}/MoS_2 (E_b= 0.63 eV) shows more energy favorable than that on Au_{13}/Mos_2 (E_b= 0.83 eV). Also H_2 dissociation on Au_{31}/MoS_2 is a one-step dissociation reaction ($H_{2(p)} \rightarrow 2H^*$), whereas a two-step reaction ($H_{2(p)} \rightarrow H_2^* \rightarrow 2H^*$) on Au_{13}/MoS_2. What's more, Au_{31}/MoS_2 has much lower barrier (0.12 eV) than Au_{13}/MoS_2 (1.22 eV) on the reaction $CH_3O^* + H^* \rightarrow CH_3OH^* + *$.

So far, we have find Au_{31}/MoS_2 show advantages on some reaction than Au_{13}/MoS_2, more important, showing two effective rotates to methanol synthesis.

6.4 Conclusion

Employing density functional theory, we have examined the competitive paths for methanol synthesis from CO hydrogenation on the bilayer 31-atom cluster of gold on MoS_2. Based on the calculated potential energy profile for elementary reactions, we find there are two effective pathways: (1) CO* → CHO* → CH_2O* → CH_3O* → CH_3OH* and (2) CO* → CHO* → HCOH* → CH_2OH* → CH_3OH*, where the former pathway showing relatively more energetic favorable. Comparing with Au_{13} [23], the bilayer 31-atom gold has the more stable structure and behave more energetic favorable on some reactions. Our future work will explore turnover frequencies of these considered reactions via Kinetic Monte Carlo Simulations in order to lead to an experimental verification.

CHAPTER 7: CONCLUSION

In this dissertation, I have explored the structural, catalytic properties of defect-laden 2D materials using a modern-quantum-mechanical approach, based on density functional theory (DFT). The results presented here not only provide fundamental understanding of those properties of defect-laden 2D material at the nanoscale but also provide guidelines to design novel functional materials for catalytic applications. Below is a chapter-wise summary of specific conclusions.

In chapter 3, I provide fundamental insights into the interaction of syngas molecules (H_2, CO, CO_2) on defect-laden hexagonal boron nitride based on first-principles DFT study. We exploring electronic structure of *dh*-BN to prescreen their active sites and adsorption mechanism. We find *dh*-BN (V_N) is the potential catalyst for CO and CO_2 hydrogenation.

In chapter 4, I provide results reaction pathways and activation energy barriers via density functional theory (DFT), I found that back-donation to the π^* orbitals of CO_2 from frontier orbitals (defect state) of the *dh*-BN (V_N) can effectively activate the CO_2 molecule for hydrogenation. Moreover, my work indicates that *dh*-BN (V_N) is an excellent metal-free catalyst for CO_2 hydrogenated to formic acid (HCOOH) and methanol (CH_3OH).

In chapter 5, I presented the results of DFT-D3 calculations of C-C bonding on 13-atom Au nanoparticle on single-layer MoS_2 with single S vacancy. We showed that Au_{13}/MoS_2 is feasible for formation of C_2 bond (acetyl) between adsorbed methyl and carbon monoxide. Moreover, hydrogenation of acetyl is also feasible on Au_{13}/MoS_2 via two reaction pathways, which to form acetaldehyde showing more energetic favorable.

In chapter 6, by studying interaction between syngas (CO and H_2) between Au_{31}/MoS_2, I found that the gold atoms at the edge sustain the substrate interaction and have strong affinity for CO in accordance with previous investigation [23]. I also found that molecular H_2 could only adsorb physically on Au_{31}/MoS_2 and the activation barrier of H_2 dissociation to 2H* is 0.63 eV, lower than that on Au_{13} [27]. Interestingly, we found that Au_{31}/MoS_2 offers excellent activity toward methanol synthesis via two competitive reaction pathways that one way is CHO* → CH_2O* → CH_3O* → CH_3OH* and another way is CHO* → CHOH* → CH_2OH* → CH_3OH*, where the former pathway showing relatively energetic favorable.

In order to design and discovery for 2D defect-laden catalyst for energy needs, my results provide fundamental insights into the interaction of syngas molecules on defect-laden hexagonal boron nitride, which help to prescreen the *dh*-BN (V_N) catalytically active for CO_2 hydrogenation reactions. Second, I showed reactions pathways on CO_2 hydrogenation to formic acid and methanol on *dh*-BN (V_N), indicating *dh*-BN an excellent metal-free hydrogenation catalyst. Third part of work, I focus on key reactions of higher alcohol synthesis from CO and methanol on MoS_2 functionalized with small 13-atom Au nanoparticle. At the fourth part, I present CO hydrogenation on small 31-atom Au bilayer on MoS_2 nanoparticle, which serve as a more effective catalyst than Au_{13}/MoS_2.

I employed modern quantum mechanical methods and powerful computational techniques to illustrate a mechanism that how these 2D-material-based catalysts have significant catalytic activity for energy needs, which could guide experimental discoveries and industrial applications.

APPENDIX A: LIST OF PUBLICATIONS

Under Review

K. Chagoya, **T. Jiang**, D.J. Nash, D. Le, T.S. Rahman and R.G. Blair, *Selectable Catalytic Reduction of Carbon Dioxide to Formic Acid or Methanol over Defect Hexagonal Boron Nitride*

K. Almeida, K. Chagoya, A. Felix, **T. Jiang**, D. Le, T.B. Rawal, P.E. Evans, M. Wurch, K. Yamaguchi,1 P.A. Dowben,L. Bartels, T.S. Rahman, R.G. Blair, *Towards Higher Alcohol Formation using a single-layer MoS_2 activated Au on Silica: Methanol Carbonylation to Acetaldehyde*

In Preparation

T. Jiang, T.B. Rawal, D. Le, T.S. Rahman, *Adsorption of Syngas Molecules on Defect-Laden Single-Layer Hexagonal Boron Nitride*

T. Jiang, D. Le, T.S. Rahman, *MoS_2-supported Au_{31} for CO hydrogenation*

LIST OF REFERENCES

[1] K. S. Novoselov, A. K. Geim, S. V. Morozov, D. Jiang, Y. Zhang, S. V. Dubonos, I. V. Grigorieva, and A. A. Firsov, Science **306**, 666 (2004).

[2] K. S. Novoselov, D. Jiang, F. Schedin, T. J. Booth, V. V. Khotkevich, S. V. Morozov, and A. K. Geim, P Natl Acad Sci USA **102**, 10451 (2005).

[3] A. K. Geim and K. S. Novoselov, Nat Mater **6**, 183 (2007).

[4] Y. Chen, Z. Fan, Z. Zhang, W. Niu, C. Li, N. Yang, B. Chen, and H. Zhang, Chemical reviews **118**, 6409 (2018).

[5] C. Tan *et al.*, Chemical reviews **117**, 6225 (2017).

[6] T. F. Jaramillo, K. P. Jørgensen, J. Bonde, J. H. Nielsen, S. Horch, and I. Chorkendorff, Science **317**, 100 (2007).

[7] H. T. Wang *et al.*, Proc. Nat. Acad. Sci. USA **110**, 19701 (2013).

[8] D. Voiry *et al.*, Nat. Mater. **12**, 850 (2013).

[9] B. Radisavljevic, M. B. Whitwick, and A. Kis, Acs Nano **5**, 9934 (2011).

[10] H. Fang, S. Chuang, T. C. Chang, K. Takei, T. Takahashi, and A. Javey, Nano Lett **12**, 3788 (2012).

[11] L. Britnell *et al.*, Science **340**, 1311 (2013).

[12] Y. Li, Y. Rao, K. F. Mak, Y. You, S. Wang, C. R. Dean, and T. F. Heinz, Nano Lett **13**, 3329 (2013).

[13] X. P. Hong *et al.*, Nat. Nanotechnol. **9**, 682 (2014).

[14] D. J. Nash *et al.*, ACS Omega **1**, 1343 (2016).

[15] J. T. Grant *et al.*, Science **354**, 1570 (2016).

[16] D. Le, T. B. Rawal, and T. S. Rahman, J. Phys. Chem. C **118**, 5346 (2014).

[17] D. Deng, K. S. Novoselov, Q. Fu, N. Zheng, Z. Tian, and X. Bao, Nat Nanotechnol **11**, 218 (2016).

[18] D. Pacile, J. Meyer, Ç. Girit, and A. Zettl, Appl Phys Lett **92**, 133107 (2008).

[19] G. Cassabois, P. Valvin, and B. Gil, Nature Photonics **10**, 262 (2016).

[20] K. Watanabe, T. Taniguchi, and H. Kanda, Nat Mater **3**, 404 (2004).

[21] A. Splendiani, L. Sun, Y. Zhang, T. Li, J. Kim, C.-Y. Chim, G. Galli, and F. Wang, Nano letters **10**, 1271 (2010).

[22] A. Ciesielski and P. Samor, Adv Mater **28**, 6030 (2016).

[23] T. B. Rawal, D. Le, and T. S. Rahman, J. Phys.: Condens. Matter **29**, 415201 (2017).

[24] W. Kohn and L. Sham, Phys. Rev. **140**, A1133 (1965).

[25] P. Giannozzi *et al.*, Journal of physics. Condensed matter : an Institute of Physics journal **21**, 395502 (2009).

[26] G. Kresse and J. Furthmüller, Computational materials science **6**, 15 (1996).

[27] C. S. Merida *et al.*, J. Phys. Chem. C **122**, 267 (2018).

[28] R. O. Jones, Rev Mod Phys **87**, 897 (2015).

[29] M. Born and R. Oppenheimer, Annalen der physik **389**, 457 (1927).

[30] L. H. Thomas, in *Mathematical Proceedings of the Cambridge Philosophical Society* (Cambridge University Press, 1927), pp. 542.

[31] E. Fermi, Zeitschrift für Physik **48**, 73 (1928).

[32] P. Hohenberg and W. Kohn, Physical review **136**, B864 (1964).

[33] P. A. Dirac, in *Mathematical Proceedings of the Cambridge Philosophical Society* (Cambridge University Press, 1930), pp. 376.

[34] R. G. Parr, in *Horizons of Quantum Chemistry* (Springer, 1980), pp. 5.

[35] S. H. Vosko, L. Wilk, and M. Nusair, Canadian Journal of physics **58**, 1200 (1980).

[36] J. P. Perdew and A. Zunger, Physical Review B **23**, 5048 (1981).

[37] L. A. Cole and J. Perdew, Physical Review A **25**, 1265 (1982).

[38] J. P. Perdew and Y. Wang, Physical Review B **45**, 13244 (1992).

[39] J. P. Perdew, K. Burke, and M. Ernzerhof, Phys. Rev. Lett. **77**, 3865 (1996).

[40] C. Lee, W. Yang, and R. G. Parr, Physical review B **37**, 785 (1988).

[41] J. P. Perdew, J. A. Chevary, S. H. Vosko, K. A. Jackson, M. R. Pederson, D. J. Singh, and C. Fiolhais, Physical Review B **46**, 6671 (1992).

[42] S. Grimme, Journal of computational chemistry **25**, 1463 (2004).

[43] S. Grimme, Journal of computational chemistry **27**, 1787 (2006).

[44] S. Grimme, J. Antony, S. Ehrlich, and H. Krieg, The Journal of chemical physics **132**, 154104 (2010).

[45] M. Dion, H. Rydberg, E. Schroder, D. C. Langreth, and B. I. Lundqvist, Phys Rev Lett **92**, 246401 (2004).

[46] K. Lee, É. D. Murray, L. Kong, B. I. Lundqvist, and D. C. Langreth, Physical Review B **82** (2010).

[47] F. Bloch, Zeitschrift für physik **52**, 555 (1929).

[48] M. C. Payne, M. P. Teter, D. C. Allan, T. Arias, and a. J. Joannopoulos, Rev Mod Phys **64**, 1045 (1992).

[49] A. Baldereschi, Physical Review B **7**, 5212 (1973).

[50] D. Chadi and M. L. Cohen, Physical Review B **8**, 5747 (1973).

[51] J. C. Phillips, Physical Review **112**, 685 (1958).

[52] D. Hamann, M. Schlüter, and C. Chiang, Phys. Rev. Lett. **43**, 1494 (1979).

[53] D. Vanderbilt, Physical review B **41**, 7892 (1990).

[54] P. E. Blöchl, Physical Review B **50**, 17953 (1994).

[55] G. Kresse and D. Joubert, Phys. Rev. B **59**, 1758 (1999).

[56] H. Eyring, The Journal of Chemical Physics **3**, 107 (1935).

[57] M. G. Evans and M. Polanyi, Transactions of the Faraday Society **31**, 875 (1935).

[58] G. J. G. Henkelman, and H. Jónsson, J. Chem. Phys. **113** (2000).

[59] G. Henkelman and H. Jonsson, J Chem Phys **113**, 9978 (2000).

[60] I. N. Remediakis, F. Abild-Pedersen, and J. K. Norskov, J Phys Chem B **108**, 14535 (2004).

[61] Y. Choi and P. Liu, Journal of the American Chemical Society **131**, 13054 (2009).

[62] Y. Yang, J. Evans, J. A. Rodriguez, M. G. White, and P. Liu, Physical chemistry chemical physics : PCCP **12**, 9909 (2010).

[63] H. Wu, X. Fan, and J.-L. Kuo, International Journal of Hydrogen Energy **37**, 14336 (2012).

[64] W. Wang, S. Wang, X. Ma, and J. Gong, Chem Soc Rev **40**, 3703 (2011).

[65] Y. Lin and J. W. Connell, Nanoscale **4**, 6908 (2012).

[66] R. Decker, Y. Wang, V. W. Brar, W. Regan, H. Z. Tsai, Q. Wu, W. Gannett, A. Zettl, and M. F. Crommie, Nano Lett **11**, 2291 (2011).

[67] J. Di, J. Xia, M. Ji, B. Wang, S. Yin, Q. Zhang, Z. Chen, and H. Li, Applied Catalysis B: Environmental **183**, 254 (2016).

[68] M. Topsakal, E. Aktürk, and S. Ciraci, Physical Review B **79** (2009).

[69] A. K. Geim, Science **324**, 1530 (2009).

[70] D. Kong, H. Wang, J. J. Cha, M. Pasta, K. J. Koski, J. Yao, and Y. Cui, Nano Lett **13**, 1341 (2013).

[71] L. Rapoport, Y. Bilik, Y. Feldman, M. Homyonfer, S. R. Cohen, and R. Tenne, Nature **387**, 791 (1997).

[72] T. B. Rawal, D. Le, and T. S. Rahman, J. Phys. Chem. C **121**, 7282 (2017).

[73] P. E. Evans, H. K. Jeong, Z. Hooshmand, D. Le, T. B. Rawal, S. N. Alvillar, L. Bartels, T. S. Rahman, and D. P. A., J. Phys. Chem C **122** 10042 (2018).

[74] H. Li *et al.*, Nat Mater **15**, 48 (2016).

[75] B. Huang and H. Lee, Physical Review B **86** (2012).

[76] C. Jin, F. Lin, K. Suenaga, and S. Iijima, Phys Rev Lett **102**, 195505 (2009).

[77] R. Schimmenti, R. Cortese, D. Duca, and M. Mavrikakis, ChemCatChem **9**, 1610 (2017).

[78] S. Lin, X. Ye, R. S. Johnson, and H. Guo, The Journal of Physical Chemistry C **117**, 17319 (2013).

[79] X. Liu, T. Duan, C. Meng, and Y. Han, RSC Adv. **5**, 10452 (2015).

[80] Q. Sun, Z. Li, D. J. Searles, Y. Chen, G. M. Lu, and A. Du, J Am Chem Soc **135**, 8246 (2013).

[81] A. L. Gibb, N. Alem, J. H. Chen, K. J. Erickson, J. Ciston, A. Gautam, M. Linck, and A. Zettl, Journal of the American Chemical Society **135**, 6758 (2013).

[82] C. K. Oliveira *et al.*, Nano Res **8**, 1680 (2015).

[83] P.-O. Löwdin, in *Advances in quantum chemistry* (Elsevier, 1970), pp. 185.

[84] R. Wang, J. Yang, X. Wu, and S. Wang, Nanoscale **8**, 8210 (2016).

[85] H. Choi, Y. C. Park, Y. H. Kim, and Y. S. Lee, J Am Chem Soc **133**, 2084 (2011).

[86] Z. L. Liu, Q. Z. Xue, T. Zhang, Y. H. Tao, C. C. Ling, and M. X. Shan, J Phys Chem C **117**, 9332 (2013).

[87] K. Mao, L. Li, W. Zhang, Y. Pei, X. C. Zeng, X. Wu, and J. Yang, Sci Rep **4**, 5441 (2014).

[88] Y.-H. Zhang, K.-G. Zhou, X.-C. Gou, K.-F. Xie, H.-L. Zhang, and Y. Peng, Chemical Physics Letters **484**, 266 (2010).

[89] Y. Jiao, A. Du, Z. Zhu, V. Rudolph, G. Q. Lu, and S. C. Smith, Catalysis Today **175**, 271 (2011).

[90] C. Le Quere *et al.*, Earth Syst Sci Data **10**, 2141 (2018).

[91] S. Bachu and J. Adams, Energy Conversion and management **44**, 3151 (2003).

[92] M. Jacoby, Chemical and Engineering News **91**, 21 (2013).

[93] G. Ménard and D. W. Stephan, Angewandte Chemie **123**, 8546 (2011).

[94] W. Li, H. Wang, X. Jiang, J. Zhu, Z. Liu, X. Guo, and C. Song, RSC Advances **8**, 7651 (2018).

[95] K. W. Ting, T. Toyao, S. M. A. H. Siddiki, and K.-i. Shimizu, ACS Catalysis **9**, 3685 (2019).

[96] J. T. Grant, W. P. McDermott, J. M. Venegas, S. P. Burt, J. Micka, S. P. Phivilay, C. A. Carrero, and I. Hermans, ChemCatChem **9**, 3623 (2017).

[97] D. J. Nash, K. L. Chagoya, A. Felix, F. E. Torres-Davila, T. Jiang, D. Le, L. Tetard, T. S. Rahman, and R. G. Blair, Advances in Applied Ceramics **118**, 153 (2019).

[98] M. Behrens *et al.*, Science **336**, 893 (2012).

[99] S. Polarz, J. Strunk, V. Ischenko, M. W. E. van den Berg, O. Hinrichsen, M. Muhler, and M. Driess, Angewandte Chemie International Edition **45**, 2965 (2006).

[100] R. J. H. Voorhoeve, J. P. Remeika, and L. E. Trimble, Annals of the New York Academy of Sciences **272**, 3 (1976).

[101] K. Ralphs, C. Hardacre, and S. L. James, Chemical Society reviews **42**, 7701 (2013).

[102] S. Immohr, M. Felderhoff, C. Weidenthaler, and F. Schüth, Angewandte Chemie International Edition **52**, 12688 (2013).

[103] I. Roger, M. A. Shipman, and M. D. Symes, Nature Reviews Chemistry **1**, 0003 (2017).

[104] K. S. McKissic, J. T. Caruso, R. G. Blair, and J. Mack, Green Chemistry **16**, 1628 (2014).

[105] S. M. Hick, C. Griebel, D. T. Restrepo, J. H. Truitt, E. J. Buker, C. Bylda, and R. G. Blair, Green Chemistry **12**, 468 (2010).

[106] B. Rodriguez, A. Bruckmann, T. Rantanen, and C. Bolm, Advanced Synthesis & Catalysis **349**, 2213 (2007).

[107] I. Milosavljevic and E. M. Suuberg, Industrial & Engineering Chemistry Research **34**, 1081 (1995).

[108] V. A. Davydov, L. S. Kashevarova, A. V. Rakhmanina, V. M. Senyavin, N. N. Oleœnikov, and V. N. Agafonov, Phys Solid State+ **44**, 557 (2002).

[109] J. Robert D. Crangle, edited by U.S. Geological Survey (U.S. Department of the Interior, Washinton, D.C., 2016), p. 7.

[110] J. C. Serrano-Ruiz and J. A. Dumesic, Energy & Environmental Science **4**, 83 (2011).

[111] D. Mei *et al.*, Journal of Catalysis **271**, 325 (2010).

[112] M. Haruta, T. Kobayashi, H. Sano, and N. Yamada, Chemistry Letters, 405 (1987).

[113] B. Hammer and J. K. Norskov, Nature **376**, 238 (1995).

[114] K. Almeida *et al.*, The Journal of Physical Chemistry C **123**, 6592 (2019).

[115] M. Haruta, S. Tsubota, T. Kobayashi, H. Kageyama, M. J. Genet, and B. Delmon, Journal of Catalysis **144**, 175 (1993).

[116] M. M. Schubert, V. Plzak, J. Garche, and R. J. Behm, Catalysis Letters **76**, 143 (2001).

[117] W. L. Deng, J. De Jesus, H. Saltsburg, and M. Flytzani-Stephanopoulos, Applied Catalysis **A291**, 126 (2005).

[118] S. D. Gardner, G. B. Hoflund, D. R. Schryer, J. Schryer, B. T. Upchurch, and E. J. Kielin, Langmuir **7**, 2135 (1991).

[119] M. S. Chen and D. W. Goodman, Science **306**, 252 (2004).

[120] Y. Y. Zhou *et al.*, Angewandte Chemie-International Edition **52**, 6936 (2013).

[121] F. Yang, J. Graciani, J. Evans, P. Liu, J. Hrbek, J. F. Sanz, and J. A. Rodriguez, J Am Chem Soc **133**, 3444 (2011).

[122] G. Kresse and D. Joubert, Physical Review B **59**, 1758 (1999).

[123] B. Wang and M. L. Bocquet, Journal of Physical Chemistry Letters **2**, 2341 (2011).

[124] K. Katsiev *et al.*, Applied Surface Science **304**, 35 (2014).

[125] J. X. Zheng, L. Wang, K. Katsiev, Y. Losovyj, E. Vescovo, D. W. Goodman, P. A. Dowben, J. Lu, and W. N. Mei, European Physical Journal B **86** (2013).

[126] L. P. Hansen, Q. M. Ramasse, C. Kisielowski, M. Brorson, E. Johnson, H. Topsoe, and S. Helveg, Angewandte Chemie-International Edition **50**, 10153 (2011).

[127] V. R. Surisetty, A. K. Dalai, and J. Kozinski, Appl Catal a-Gen **404**, 1 (2011).

[128] M. R. Morrill, N. T. Thao, H. Shou, R. J. Davis, D. G. Barton, D. Ferrari, P. K. Agrawal, and C. W. Jones, Acs Catalysis **3**, 1665 (2013).

[129] M. T. Claure, S. H. Chai, S. Dai, K. A. Unocic, F. M. Alamgir, P. K. Agrawal, and C. W. Jones, Journal of Catalysis **324**, 88 (2015).

[130] V. R. Surisetty, A. K. Dalai, and J. Kozinski, Applied Catalysis a-General **385**, 153 (2010).

[131] M. M. Lv, W. Xie, S. Sun, G. M. Wu, L. R. Zheng, S. Q. Chu, C. Gao, and J. Bao, Catalysis Science & Technology **5**, 2925 (2015).

[132] W. Xie, J. L. Zhou, L. L. Ji, S. Sun, H. B. Pan, J. F. Zhu, C. Gao, and J. Bao, Rsc Advances **6**, 38741 (2016).

[133] H. T. Luk, C. Mondelli, D. C. Ferre, J. A. Stewart, and J. Perez-Ramirez, Chemical Society reviews **46**, 1358 (2017).

[134] H. T. Luk, T. Forster, C. Mondelli, S. Siol, D. Curulla-Ferre, J. A. Stewart, and J. Perez-Ramirez, Catalysis Science & Technology **8**, 187 (2018).

[135] M. Ao, G. H. Pham, J. Sunarso, M. O. Tade, and S. M. Liu, Acs Catalysis **8**, 7025 (2018).

[136] J. Kim, S. Byun, A. J. Smith, J. Yu, and J. X. Huang, Journal of Physical Chemistry Letters **4**, 1227 (2013).

[137] T. Osaki, N. Narita, T. Horiuchi, T. Sugiyama, H. Masuda, and K. Suzuki, Journal of Molecular Catalysis A: Chemical **125**, 63 (1997).

[138] F. Besenbacher *et al.*, Catalysis Today **130**, 86 (2008).

[139] D. Sun *et al.*, Angewandte Chemie **124**, 10430 (2012).

[140] J. Kibsgaard, Z. B. Chen, B. N. Reinecke, and T. F. Jaramillo, Nature Materials **11**, 963 (2012).

[141] T. A. Ho, C. Bae, S. Lee, M. Kim, J. M. Montero-Moreno, J. H. Park, and H. Shin, Chemistry of Materials **29**, 7604 (2017).

[142] Q. Ma *et al.*, Journal of Physics-Condensed Matter **25**, 252201 (2013).

[143] Q. Ma *et al.*, Acs Nano **8**, 4672 (2014).

[144] S. Singh, S. Li, R. Carrasquillo‐Flores, A. C. Alba‐Rubio, J. A. Dumesic, and M. Mavrikakis, AIChE Journal **60**, 1303 (2014).

[145] M. Haruta, The chemical record **3**, 75 (2003).

[146] D. Andreeva, V. Idakiev, T. Tabakova, A. Andreev, and R. Giovanoli, Applied Catalysis A: General **134**, 275 (1996).

[147] J. Jia, K. Haraki, J. N. Kondo, K. Domen, and K. Tamaru, J. Phys. Chem. B **104**, 11153 (2000).

[148] J. Saavedra, T. Whittaker, Z. Chen, C. J. Pursell, R. M. Rioux, and B. D. Chandler, Nat Chem **8**, 584 (2016).

[149] S. Hong and T. S. Rahman, J. Am. Chem. Soc. **135**, 7629 (2013).

[150] A. Gazsi, T. Bánsági, and F. Solymosi, Catal. Lett. **131**, 33 (2009).

[151] Z.-P. Liu, X.-Q. Gong, J. Kohanoff, C. Sanchez, and P. Hu, Phys. Rev. Lett. **91**, 266102 (2003).

[152] I. N. Remediakis, N. Lopez, and J. K. Norskov, Angew. Chem. Int. Ed. **44**, 1824 (2005).

[153] L. B. Vilhelmsen and B. Hammer, ACS Catalysis **4**, 1626 (2014).

[154] Z. Duan and G. Henkelman, ACS Catal. **5**, 1589 (2015).

[155] I. X. Green, W. Tang, M. Neurock, and J. T. Yates, Science **333**, 736 (2011).

[156] T. Whittaker, K. B. S. Kumar, C. Peterson, M. N. Pollock, L. C. Grabow, and B. D. Chandler, J Am Chem Soc (2018).

[157] R. F. Bader, Accounts of chemical research **18**, 9 (1985).

[158] G. Henkelman, A. Arnaldsson, and H. Jónsson, Computational Materials Science **36**, 354 (2006).